JUSTUS-LIEBIG-
UNIVERSITÄT
GIESSEN

On Vietoris-Rips Complexes of the 2-Sphere

Dissertation

Zur Erlangung des akademischen Grades
Dr. rerum naturalium (Dr. rer. nat.)

dem Fachbereich 07 der
Justus-Liebig-Universität
Gießen vorgelegt von

Nada Saleh

Betreuer: Prof. Dr. Ralf Köhl
Co-Betreuer: Prof. Dr. Stefan Witzel

September, 2023

This thesis is printed and published with the support of the German academic exchange services DAAD.

ACKNOWLEDGMENTS

First and foremost I would like to acknowledge my supervisors: Prof. Ralf Köhl and Prof. Stefan Witzel for their invaluable advice, continuous support, and patience during my PhD study. Their immense knowledge and plentiful experience have encouraged me in all the time of my academic research and daily life. Besides my supervisors, I would like to thank the committee members: Prof. Matthias Meiners, Prof. Klaus Metsch and Prof. Mohameden Ahmedou for their insightful comments. I am sincerely grateful to Dr. Gerrit Eichner for his guidance on applying statistical tools using R, and to Dr. Marcel Giar for his technical support on running HPC computations. My deepest gratitude goes to Prof. Henry Adams for his guidance and valuable suggestions on this project. I would also like to thank my colleague Thomas Titz-Mite for his support in the 'gap' code. My appreciation goes out to DAAD for funding this research under the 'PhD and Research Grants' program. Finally, my thanks goes out to my child, Amr, for being a great motivation for establishing our life in Germany and to my father, for being my dearest friend.

Deutsche Zusammenfassung

Eine der praktischen Methoden, um die Form der Daten zu untersuchen, ist die Anwendung der topologischen Datenanalyse (TDA). Dieses aufstrebende Gebiet befasst sich mit der Berechnung topologischer Invarianten und der Untersuchung ihrer Stabilität unter kleinen Störungen. TDA liegt auf dem Gebiet der Datenanalyse, algebraischen Topologie, Computergeometrie, Informatik und Statistik. Ein leistungsfähiges Werkzeug der TDA ist die persistente Homologie (PH), die auf algebraischer Topologie basiert und es uns ermöglicht, qualitative Merkmale von Daten anhand komplexer Strukturen zu interpretieren.

Das Ziel dieser Arbeit ist es, die Homotopietypen von Vietoris-Rips-Komplexen des Kreises statistisch zu belegen und die Homotopietypen von Vietoris-Rips-Komplexen von platonischen Körpern, den fünf regulären Objekten, die die 2-Sphäre repräsentieren, zu untersuchen.

Contents

Introduction

In recent years, the vast amount of data we are drawn in necessitates the development of new efficient data-processing tools. One of the practical methods to explore the shape of data is applying topological data analysis (TDA). This emerging field is concerned with computing topological invariants and studying their stability under small perturbations. TDA lies in the fields of data analysis, algebraic topology, computational geometry, computer science, and statistics. A powerful tool of TDA is persistent homology (PH), which is based on algebraic topology, that enables us to interpret qualitative features of data by complex structure. Persistent homology has various applications on proteins [KNBNH16], nuclear collisions [HDP22], robotics [VAB13], cancer [CMC$^+$16], and many more. PH provides insight into data sets representing finite metric spaces (point clouds), digital images with their cubical structures (pixels), level sets of real-valued functions, and networks. When studying point clouds, a thickening of it at different time scales is applied and the role of PH is to analyze the evolution of the resulting topological features, namely the number of connected components, holes, and voids.

We restrict our work to point clouds sampled from a metric space. When building the simplicial complex on a point cloud, we expect that the computed homology of the simplicial complex approximates the homology of the space. This condition is guaranteed when dealing with Čech complexes due to the Nerve Theorem [DW22, Chapter 2.2]. However, since we must check for higher order intersections of the balls in Čech complexes, homology computations turn out to be more expensive than the ones of the Vietoris–Rips complexes, where the former is a subcomplex of the latter, and with the Vietoris-Rips such a guarantee does not always exist. However, Hausmann [H$^+$95] and Latschev [Lat01] have proved that for a small-scale parameter, Vietoris-Rips complexes recover the topology of the original space.

The homotopy types of Vietoris–Rips complexes are fully known for very few shapes like the circle [AA17], regular polygons on n-sides where n is an odd double factorial, [ACJS18] and ellipses [AAR19]. One of the open problems is characterizing the homotopy types of Vietoris-Rips complexes of higher dimensional spheres and tori [GFW17].

The aim of this thesis is to provide statistical evidence of the homotopy types of Vietoris-Rips complexes of the circle and investigate the homotopy types of Vietoris-Rips complexes of Platonic solids, the five regular objects representing the 2-sphere.
In Chapter 1, we present topological preliminaries and related theory. In Chapter 2, we apply statistical tools to approximate the first three homotopy types of $\mathrm{VR}_r(S^1)$, where $r = \frac{1}{3}, \frac{2}{5}$, and $\frac{3}{7}$. We provide three ways for generating point clouds on the $2-$sphere and present computational outcomes. In Chapter 3, we study the homotopy types of Vietoris-Rips complexes of Platonic solids, with a focus on the dodecahedron case. Finally, in Chapter 4, we provide some observations on the homology of some higher-dimensional polytopes: the hypercubes and the 4-dimensional polytopes.

Chapter 1

Topological Prerequisites

We start the exposition by providing an overview of the topological concepts we use in this thesis. For further detailed explanations, we direct the reader to the books [Zom09], [DW22], [Hat02], [EH22], and [KMM04].

Topological spaces that are equivalent to each other are called homeomorphic. However, it is not easy in general to show that two topological spaces are homeomorphic. Therefore, a weaker notion that interprets the similarity between topological spaces is known to be homotopy.

1.1 Homotopy

Definition 1.1.1. Let $f_1, f_2 : X \to Y$ be two continuous maps between the topological spaces X, Y. A continuous function $F : X \times [0,1] \to Y$ is a homotopy between f_1 and f_2 if $F(x,0) = f_1(x)$ and $F(x,1) = f_2(x)$. Then f_1 and f_2 are homotopic to each other and we write $f_1 \simeq f_2$.

The second parameter of F is usually interpreted by time. Hence, F describes a continuous deformation from f_1 into f_2 as time varies from 0 to 1.

Definition 1.1.2. Two topological spaces X and Y are homotopy equivalent if there exist maps $f : X \to Y$ and $g : Y \to X$ such that $f \circ g \simeq id_Y$ and $g \circ f \simeq id_X$.

To state that two topological spaces are homeomorphic, f and g should be inverses of each other. This condition is relaxed in the homotopy equivalence since we require here that the composition of the two functions is homotopic to the identity maps. Two homeomorphic spaces are necessarily homotopy equivalent, but the converse is not true.

A topological space is said to be contractible if it is homotopy equivalent to a point.

Definition 1.1.3. Let X be a topological space, and $U \subseteq X$ a subspace. Let $\iota : U \hookrightarrow X$ be the inclusion map. A continuous map $f : X \to U$ is named

- a retraction if $f\,|_U = id_U$;
- a deformation retraction if $\iota \circ f : X \to X$ is homotopic to the identity map id_X,
- a strong deformation retraction if there exists a homotopy $F : X \times [0,1] \to X$ between $\iota \circ f$ and id_X that is constant on U, i.e., $F(u,t) = u$, for all $t \in [0,1]$ and $u \in U$.

If U is a deformation retract of X, then X and U are homotopy equivalent.

1.2 Simplicial Complexes

Since in this thesis, we are dealing with topological spaces that can be represented discretely, it is convenient to present the building blocks of these spaces.

Definition 1.2.1. A k-simplex σ is the convex hull of $(k+1)$-affinely independent points $S = \{v_0, v_1, \ldots, v_k\}$, where the points of S are the vertices of the simplex and k is its dimension.
For $0 \leqslant k' \leqslant k$, a k'-face τ of σ is a k'-simplex that is the convex hull of a non-empty subset of S, where σ is a coface, and we write $\tau < \sigma$.
When $\dim \tau = \dim(\sigma) - 1$, we call τ a facet and σ a cofacet, and we write $\tau \prec \sigma$.

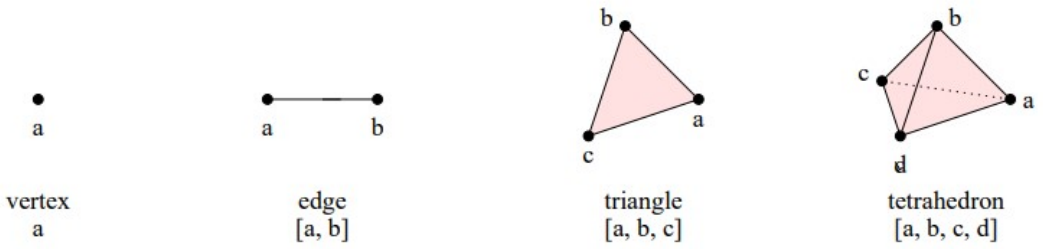

Figure 1.1: k-simplices, for $0 \leqslant k \leqslant 4$.

Definition 1.2.2. A collection K of non-empty subsets of a given set S is an abstract simplicial complex if every element $\sigma \in K$ has all of its non-empty subsets $\sigma' \subseteq \sigma$ also in K.

Definition 1.2.3. A geometric simplicial complex K is a finite set of simplices such that

- K contains every face of each simplex in K.
- For any two simplices $\sigma, \tau \in K$, their intersection $\sigma \cap \tau$ is either the empty set or a face of both σ and τ.

A geometric simplicial complex K in $\mathbb{R}^m$ is called a geometric realization of an abstract simplicial complex K' if and only if there is an embedding $e : V(K') \to \mathbb{R}^m$ that takes every k-simplex $\{v_0, v_1, \ldots, v_k\}$ in K' to a k-simplex in K that is the convex hull of $e(v_0), e(v_1), \ldots, e(v_k)$.

Definition 1.2.4. For any $k \geqslant 0$, the k-skeleton of a simplicial complex K, denoted by $K^{(k)}$, is the maximal subcomplex formed by all simplices of dimension at most k.

Definition 1.2.5. A simplicial complex K is a flag complex, if for each subset of vertices $S = \{v_0, ..., v_k\} \subseteq K^{(0)}$, if every pair of vertices in S is in the complex, then S itself is in the complex too. Equivalently, the flag complex is the clique complex of its graph.

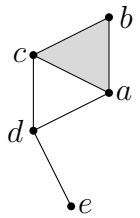

Figure 1.2: A simplicial complex K with five vertices.

For example, the complex drawn in Figure 1.2 is a geometric realization of the abstract complex with five vertices a, b, c, d, e, six 1-simplices $\{a, b\}, \{a, c\}, \{a, d\}, \{b, c\}, \{c, d\}, \{d, e\}$ and one 2-simplex $\{a, b, c\}$. Its 1-skeleton consists of the five vertices a, b, c, d, e and the six edges adjoining them.

Definition 1.2.6. Let (X, d) be a finite metric space. Given a real $r > 0$, the Vietoris-Rips complex $VR_r(X)$ is the abstract simplicial complex with the vertex set X, where a finite subset $F \subseteq X$ is the vertex set of a simplex σ if and only if $d(p, q) \leqslant 2r$ for every pair of vertices in F.

What makes the Vietoris-Rips complex interesting to study is its interleaving relation to the Čech complex, see for example [DW22, Proposition 2.2], and what makes it easier to study is that $VR_r(X)$ is the clique complex of its 1-skeleton, i.e. it is a flag complex.

1.3 Homology of simplicial complexes

Definition 1.3.1. Given an abelian group M and a commutative ring R with multiplicative identity 1, an R-Module M is an abelian group with an operation $R \times M \to M$ which satisfies the following properties for all $r, r' \in R$ and $x, y \in M$:

- $r.(x + y) = r.x + r.y$;
- $(r + r')x = r.x + r'.x$;
- $1.x = x$;
- $(r.r').x = r.(r'.x)$.

Elements in an R-Module are added and multiplied with coefficients in R. If R is replaced with a field F, M becomes a vector space.

In algebraic topology, the integral domain $\mathbb{Z}$ is considered in general for coefficients, whereas the field $\mathbb{Z}_2$ is usually considered for homology computations. The latter, where $a = -a, \forall a \in \mathbb{Z}_2$, imposes that the notion of the orientation of simplicial complexes becomes irrelevant.

Definition 1.3.2. A k-chain c in a simplicial complex K is a formal sum of k-simplices weighted with some coefficients, namely, $c = \Sigma_q a_q \sigma_q$, where $\sigma_q \in K, a_q \in \mathbb{Z}, \forall q$.

The set of k-chains of K along with the addition operator form an abelian group $(C_k(K), +)$, called the k-th chain group of K. Consequently, we obtain the module $C_k(K)$.

Chain groups at different dimensions are related by a boundary homomorphism.

Definition 1.3.3. The boundary map $\partial_k : C_k(K) \to C_{k-1}(K)$ is a map from the group of k-chains to the group of $(k-1)$-chains. For a k-simplex $\sigma = (v_0, ..., v_k)$, the boundary is a $(k-1)$-chain, defined by:

$$\partial_k(\sigma) = \sum_{i=0}^{k} (-1)^i (v_0, \ldots, \widehat{v_i}, \ldots, v_k),$$

where $\widehat{v_i}$ indicates that the vertex v_i is omitted.

For a k-chain $c = \Sigma_q a_q \sigma_q$, the boundary is a $(k-1)$-chain, which is defined by:

$$\partial_k(c) = \partial_k \sum_q a_q \sigma_q = \sum_q a_q \partial_k \sigma_q,$$

Since the boundary of a vertex is 0 and ∂_k commutes with addition, the boundary map is indeed a homomorphism. The boundary homomorphisms of K induce the sequence:

$$... \xrightarrow{\partial_{k+1}} C_k(K) \xrightarrow{\partial_k} C_{k-1}(K) \xrightarrow{\partial_{k-1}} C_{k-2}(K) \xrightarrow{\partial_{k-2}} ...$$

which is called the chain complex of K, and denoted by $C_*(K)$. For a shorter notation, and when K is clear from the context, we can write C_*.

Lemma 1.3.1. *[Zom05, Theorem 4.3]*
For $k > 0$ and any k-chain c, $\partial_{k-1} \circ \partial_k(c) = 0$.

Proof. We know,

$$\partial_k[v_0, v_1, ..., v_k] = \Sigma_i(-1)^i[v_0, ..., \widehat{v}_i, ..., v_k].$$

We have to compute, $\partial_{k-1} \circ \partial_k[v_0, v_1, ..., v_k]$, which equals

$$\Sigma_i(-1)^i\left(\Sigma_{0\leqslant j<i}(-1)^j[v_0, ..., \widehat{v}_j, ..., \widehat{v}_i, ..., v_k]+\Sigma_{i\leqslant j\leqslant(k-1)}(-1)^j[v_0, ..., \widehat{v}_i, ..., \widehat{v_{j+1}}, ..., v_k]\right)$$

replacing each $j+1$ with n in the second term, we get,

$$\Sigma_i(-1)^i\left(\Sigma_{0\leqslant j<i}(-1)^j[v_0, ..., \widehat{v}_j, ..., \widehat{v}_i, ..., v_k]+\Sigma_{i<n\leqslant k}(-1)^{n-1}[v_0, ..., \widehat{v}_i, ..., \widehat{v}_n, ..., v_k]\right),$$

by summing,

$$\Sigma_i(-1)^i\left(\Sigma_{0\leqslant j<i}(-1)^j[v_0, ..., \widehat{v}_j, ..., \widehat{v}_i, ..., v_k] - \Sigma_{i<n\leqslant k}(-1)^n[v_0, ..., \widehat{v}_i, ..., \widehat{v}_n, ..., v_k]\right)$$

these two summands have opposite signs, so they cancel each other. □

Definition 1.3.4. A k-chain c is a k-cycle if $\partial_k c = 0$. The collection of cycles forms the k-th cycle group, defined by, $Z_k = \ker \partial_k$. Consequently, $Z_k(K)$ is also a module.

The set of k-chains, that can be obtained by applying the boundary operator ∂_k on k-chains, forms the k-th boundary group, and is defined by, $B_k = \operatorname{im} \partial_{k+1}(C_k)$. Similarly, we obtain the module $B_k(K)$.

Z_k and B_k are subgroups of C_k. By Lemma 1.3.1, it follows that B_k is a subgroup of Z_k.

Definition 1.3.5. For $k \geqslant 0$, the k-th homology group of K is the quotient group H_k, where,

$$H_k = Z_k/B_k = \ker \partial_k / \operatorname{im} \partial_{k+1}.$$

In Figure 1.2, considering the 1-cycles of K:

$$\begin{aligned} x &= \{a,c\} + \{c,d\} + \{d,a\} \\ y &= \{a,b\} + \{b,c\} + \{c,d\} + \{d,a\} \\ y - x &= \{a,b\} + \{b,c\} + \{c,a\} \end{aligned}$$

is a 1-boundary. Since x and y differ by one boundary, they are homologous cycles, which are obviously homotopic. Note that each element of H_k consists of homologous cycles.

When $\mathbb{Z}_2$ is the considered field for coefficients, H_k is a vector space and its dimension is known to be the k-th Betti number, denoted by β_k, where,

$$\beta_k := dim(H_k) = dim(Z_k) - dim(B_k)$$

Informally, β_k refers to the number of k-dimensional holes of K, where

- β_0 is the number of connected components,
- β_1 is the number of one-dimensional holes, "circular", and
- β_2 is the number of one-dimensional voids, "cavities".

For instance, the Torus has $\beta_0 = 1$, $\beta_1 = 2$, and $\beta_2 = 1$, and the Sphere S^2 has $\beta_0 = 1$, $\beta_1 = 0$, and $\beta_2 = 1$.

In general, homology groups are more computable than homotopy groups, and Hurewicz's theorem provides a relationship between the two:

Theorem 1.3.2. *[Hat02, Theorem 4.32] If a space X is $(n-1)$-connected, $n \geqslant 2$, then $\tilde{H}_i(X) = 0$ for $i < n$ and $\pi_n(X) \approx H_n(X)$. If a pair (X, A) is $(n-1)$-connected, $n \geqslant 2$, with A simply connected and nonempty, then $H_i(X, A) = 0$ for $i < n$ and $\pi_n(X, A) \approx H_n(X, A)$.*

1.4 Persistent homology

In this section, we introduce maps between simplicial complexes and their induced maps on homology groups. The main reference for this subsection is [DW22, Chapter 3] and [Cho17, Chapter 2].

Definition 1.4.1. Let K_1 and K_2 be two simplicial complexes and $\hat{f} : K_1^{(0)} \to K_2^{(0)}$. If for each $v \in K$, there exists some vertex $\hat{f}(v) \in K_2$, then $\hat{f}$ is called a vertex map.
If for each simplex $\sigma = (v_0, ..., v_k) \in K_1$, the set $\{\hat{f}(v_0), ..., \hat{f}(v_k)\}$ spans a simplex in K_2, then the linear extension of the vertex map to simplices of K_1, $f : K_1 \to K_2$, is called the simplicial map.

Simplicial maps are continuous, and they induce chain maps.

Definition 1.4.2. Let K_1 and K_2 be two simplicial complexes. A chain map is a family of homomorphisms $f_\# : C_k(K_1) \to C_k(K_2)$ between chain complexes of K_1 and K_2, which satisfy $f_\# \circ \partial_{k,K_1} = \partial_{k,K_2} \circ f_\#$, for each k. For each simplex $\sigma \in K_1$,

$$f_\#(\sigma) \simeq \begin{cases} f(\sigma) & dim(f(\sigma)) = k \\ 0 & otherwise \end{cases}$$

Chain maps satisfy the two properties of functorality:

- The identity simplicial map on K induces the identity chain map on $C_k(K)$.
- If $f_1 : K_1 \to K_2, f_2 : K_2 \to K_3$ are simplicial maps between the simplicial complexes K_1, K_2, and K_3, then $(f_2 \circ f_1)_\# = (f_2)_\# \circ (f_1)_\#$.

Hence, $(C_k, \#)$ is a functor from the category of simplicial complexes and simplicial maps to the category of chain complexes and chain maps.

In a similar fashion, we see that chain maps induce homomorphisms between the respective homology groups, namely, $f_* : H_k(K_1) \to H_k(K_2)$.

Analogously, $(H_k, *)$ is a homology functor from the category of simplicial complexes and simplicial maps to the category of abelian groups and homomorphisms.

Definition 1.4.3. A filtration $\mathcal{F} = \mathcal{F}(K)$ over a simplicial complex K is a nested sequence of its subcomplexes

$$\mathcal{F} : \varnothing = K_0 \hookrightarrow K_1 \hookrightarrow ... \hookrightarrow K_n = K$$

$\mathcal{F}$ is called simplex-wise if either $K_i \backslash K_{i-1}$ is empty or a single simplex for every $i \in [1, n]$.

An example of a simplicial filtration is the Vietoris-Rips complexes. For any two scales $0 \leqslant a_i \leqslant a_j$, we have $\mathrm{VR}_{a_i}(X) \subseteq \mathrm{VR}_{a_j}(X)$, which gives a filtration $(\mathrm{VR}_a(X))_{a \geqslant 0}$ over the range of scales $[0, \infty)$.

The inclusions in a simplicial filtration are the simplicial maps, and as we mentioned earlier, since the simplicial complexes $(K_a)_{a \in I}$, where $I \subseteq \mathbb{R}$ is an index set,

together with the composition of simplicial maps $\{f_{a_i,a_j}\}_{a_i \leqslant a_j \in I}$ form a category. Hence, applying the homology functor induces vector spaces $(H_k(K_a))_{a\in I}$ connected with linear maps $f_*^{i,j} : H_k(K_{a_i}) \to H_k(K_{a_j})$. Hence, we obtain a sequence of persistent modules.

Definition 1.4.4. Let $\mathcal{F}$ be a filtration, the k-th persistent homology groups are the images of the homomorphisms: $H_k^{i,j} = H_k^{a_i,a_j} = \text{im } f_k^{i,j}$, for $0 \leqslant a_i \leqslant a_j \leqslant n$. The k-th persistent Betti numbers are the dimensions of the vector spaces $H_k^{i,j}$, $\beta_k^{i,j} = \beta_k^{a_i,a_j} = \dim(H_k^{i,j})$.

Definition 1.4.5. A non-trivial k-th homology class $z \in H_k(K_a)$ is born at $K_i, i \leqslant a$ if $z \in H_k^{i,a}$, but $z \notin H_k^{i-1,a}$.
A non-trivial k-th homology class $z \in H_k(K_a)$ dies entering $K_j, a < j$, if $h_k^{a,j-1}(z) \neq 0$, (non-trivial) but $h_k^{a,j}(z) = 0$. We say that z persists for the range of scale $[i, j]$, i is the birth value of z and j is its death value.

The lifetime intervals are called barcodes. They summarize the topological persistence of a filtration. Another visualization tool for the lifetime of a class is the persistence diagrams. However, in this thesis, we restrict ourselves to using barcodes as a representation tool.

Example 1.4.1. In this example, we build a hexagon, where at a filtration value 0, the 0-simplices [a], [b], [c], [d], [e], and [f] appear. At value 1, the 1-simplices [a,b], [c,d], [d,e], [e,f], and [f,a] appear. At value 2, [b,c] appears. At value 3, [a,c] appears; finally, at value 4, the 2-simplex [a,b,c] appears. We compute its homology using JavaPlex package [ATVJ14] and we get the following barcodes and their representative cycles:

Dimension: 0
$[0, 1)$: [b] - [a]
$[0, 1)$: [d] - [c]
$[0, 1)$: [e] - [d]
$[0, 1)$: [f] - [e]
$[0, 1)$: [c] - [a]
$[0, \infty)$: [a]

Dimension: 1
$[3, 4)$: [b,c] + [a,b] - [a,c]
$[2, \infty)$: [d,e] + [b,c] + [a,f] + [e,f] + [a,b] + [c,d]

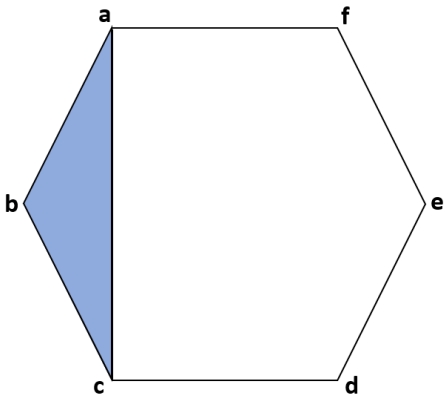

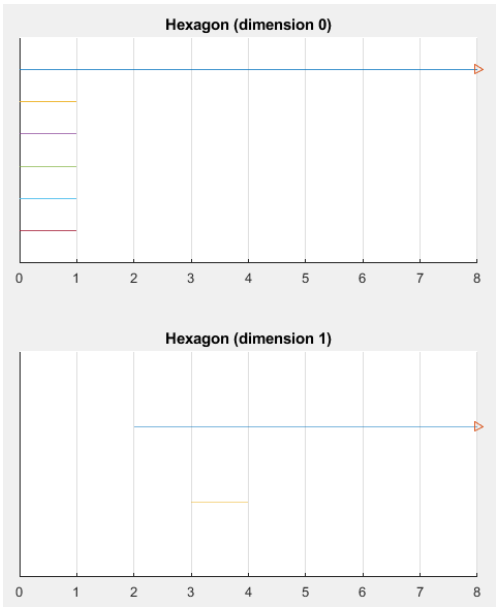

The birth of six barcodes in dimension 0 states that we have six 0-simplices, the long barcode represents that we have one connected component. In dimension 1, we have a hole that is created at value 3 and destroyed at value 4, whereas the second hole is created at value 2 and lasts to infinity.

Example 1.4.2. In this example, we build the Vietoris-Rips complex on the vertices of a hexagon and compute its homology up to dimension 2. We get the following barcodes:

Dimension: 0
$[0, \infty)$
$[0, 1)$
$[0, 1)$
$[0, 1)$
$[0, 1)$
$[0, 1)$

Dimension: 1
$[1, 1.732)$

Dimension: 2
$[1.732, 2)$

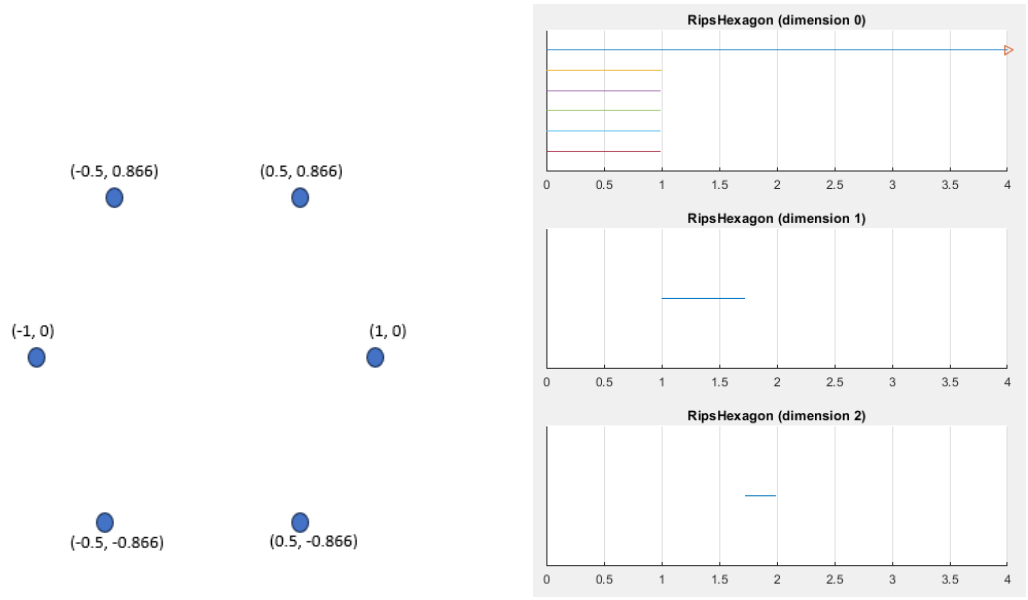

Analogously, the birth of six barcodes in dimension 0 states that we have six 0-simplices, where the long barcode means that we have one connected component. The other five barcodes die by the birth of the shortest 1-simplices, which creates the first-dimensional hole that lasts until the birth of the 1-simplices connecting two non-adjacent vertices, which in turn creates a second-dimensional hole lasting until the birth of the longest 1-simplices. We reach the closing radius where the whole simplicial complex becomes filled and contracts to a point.

For another example on JavaPlex, see [AT+11].

1.5 Acyclic matching

Discrete Morse Theory has been developed by Robin Forman as a tool to investigate the homotopy types of simplicial complexes [For02]. The theory aims to pair faces in a simplicial complex to give rise to a sequence of collapses that yields a homotopy equivalent complex.

Definition 1.5.1. Following [Koz08, Chapter 6], If K is a simplicial complex, and $\sigma, \tau \in K$ where

- τ is a face of σ, and
- σ is a maximal simplex such that no other maximal simplex contains τ,

then a simplicial collapse of K is the removal of all simplices γ such that $\tau \subseteq \gamma \subseteq \sigma$. When τ is a facet of σ, it is called an elementary collapse.

Proposition 1.5.1. *[Koz08, Proposition 6.14] A sequence of collapses yields a strong deformation retraction, in particular, a homotopy equivalence.*

We introduce some combinatorial concepts that encode the simplicial structure which helps in following the collapsing sequences.

Definition 1.5.2. Let K be an arbitrary abstract simplicial complex. The face poset of K is a partially ordered set, denoted by $F(K)$, and defined such that:

- the elements of $F(K)$ are all the simplices of K, including the empty one,
- the partial order is given by the inclusion relation on the simplices, i.e., we write $\tau \leqslant \sigma$ as components of $F(K)$ if and only if $\tau \subseteq \sigma$ as simplices.

Matching is the combinatorial notion for the face posets corresponding to elementary simplicial collapses.

When considering the set of vertices of a partially ordered set P as the set of vertices of that graph, and connecting two elements by an edge if and only if one of these elements is a facet of the other, one obtains a graph known to be the underlying graph of the Hasse diagram of P.

Definition 1.5.3. A partial matching in a poset P is a partial matching in the underlying graph of the Hasse diagram of P. Formally, it is a subset $M \subseteq P \times P$ such that

- if $(a, b) \in M$ implies $a \prec b$,
- each $a \in P$ belongs to at most one element in M.

A partial matching on P is called acyclic if there does not exist a cycle

$$a_1 \succ b_1 \prec a_2 \succ b_2 \prec ... \prec a_n \succ b_n \prec a_1$$

with $n \leqslant 2$, and all $a_i, b_i \in P$ being distinct.

From this definition, and particularly when $P = F(K)$, we can see that the matched simplices are the facets or the cofacets, and the unmatched simplices are the critical ones. We impose the notion of orientation on the edges of the Hasse diagram such that the edges of the matched simplices are directed upwards, and a non-matching edge is directed downwards. A vertex without a matching edge is critical. Furthermore, the matching is acyclic if the diagram has no directed cycles. The proof of acyclicity of the graph can be restricted to adjacent dimensions due to the second condition of Definition 1.5.3.

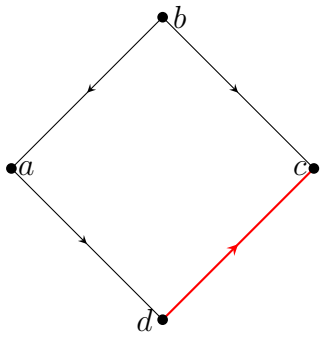

Figure 1.3: The vertex a is critical, whereas (d,c) is a matched pair.

Proposition 1.5.2. *[Koz21, Theorem 10.9] Assume K is an abstract simplicial complex, and assume K' is a simplicial subcomplex of K, such that $K \backslash K'$ is finite. The following statements are equivalent:*

1. *there exists a sequence of elementary collapses leading from K to K';*
2. *there exists a complete acyclic matching on the set of all simplices of K which are not contained in K'.*

In this chapter, we provided the basic topological concepts used in this thesis. We defined the notion of homotopy between topological spaces. We presented the fundamental concept of simplicial complexes and the homology carried by such structures and pointed Hurewicz's theorem that relates homotopy to homology. Later in section 1.4, we defined the concept of persistent homology which represents the topological information carried by special collections of simplicial complexes. We defined a filtration and provided the Vietoris-Rips complex as an important example of it. In section 1.5, we explained the concept of acyclic matching and expressed an equivalence relation between the existence of an acyclic matching and the existence of a sequence of simplicial collapses.

Chapter 2

Homology computations of Vietoris-Rips complexes

The aim of this thesis was to characterize the homotopy types that Vietoris-Rips complex $\mathrm{VR}_r(S^2)$ of the 2-Sphere can obtain when the radius r ranges over $[0, \infty)$. Our methodology was mainly experimental; knowing that the homotopy types of the Vietoris-Rips complex of the circle are fully classified [AA17], we started computing the homology of finite point-clouds representing the circle and comparing the computational outcome with theory to acquire evidence of how good the approximations are. On the circle, we have an accordance described by very good approximations. The next step was investigating the behavior of the Vietoris-Rips complex of the 2-Sphere and deducing theoretical statements from experimental observations. However, due to the exponential growth of the sizes of the simplices, PCs or even High-Performance Clusters (HPC) were unable to handle such computations. Even for a small to medium-sized point cloud on the 2-Sphere, we could not compute all the homology types of its Vietoris-Rips complex due to the extensive memory consumption. In the coming two sections, we present the experimental approach, first on the circle and later on the 2-sphere.

2.1 Vietoris-Rips of the 1-Sphere

In this section, we first explain the routine of producing point clouds representing the circle, and later, we try to approximate the first three obtainable death values of $\mathrm{VR}_r(S^1)$ depending on two approaches: Monte-Carlo simulations leading to estimating confidence intervals and fitting regression models.

2.1.1 Point-clouds approximating the 1-Sphere

The generating mechanism for finite point clouds representing the circle depends on polar parameters. Let n be the size of the point cloud, the angle $\theta_1, \theta_2, ..., \theta_n \in [0, 2\pi]$ can be a random sample coming from distributions like uniform, normal, or wrapped normal, etc. The second parameter is the radius of the circle $r'_1, r'_2, ..., r'_n$, which whenever it is fixed, the point cloud lies exactly on the circumference of the circle $S^1_{r'}$. Obviously, r' itself can also be a random variable coming from a distribution of positive support, like the log-normal, and the exponential distribution. In the case where r' is a random variable, the generated point-cloud is *"jittered"* around the circumference, approximating the shape of a circle. This results in clustering, where one might identify the radius of clusters and compare the homology of an original point cloud with its cluster-free version. For such a comparison, one might apply the greedy permutation technique, see for instance [CJS15] and [TSBO18].

The following examples are of point clouds approximating S^1 with their zeroth and first-dimensional barcodes.

Example 2.1.1. A point-cloud of size 300 where $\theta_1, \theta_2, ..., \theta_n \sim U(0, 2\pi)$ and $r'_1, r'_2, ..., r'_n \sim Lognormal(\log(\frac{1}{2\pi}), 0.1)$ with its corresponding zero and one dimensional barcodes.

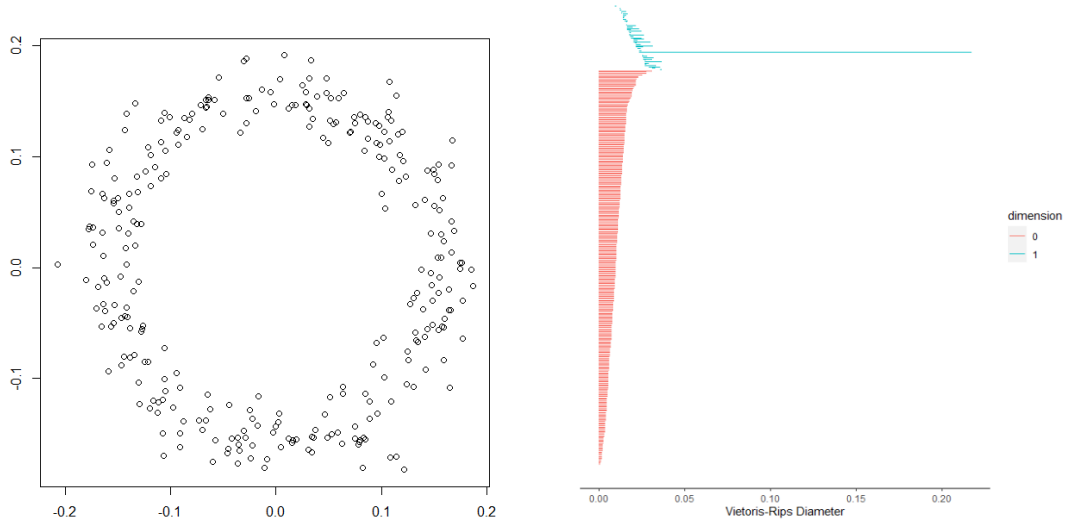

Figure 2.1: Lognormal distribution of the radius parameter r'.

Example 2.1.2. A point-cloud of size 300 where $\theta_1, \theta_2, ..., \theta_n \sim U(0, 2\pi)$ and $r'_1, r'_2, ..., r'_n \sim \text{Exp}(\lambda = 10)$ and its corresponding zero and one dimensional barcodes.

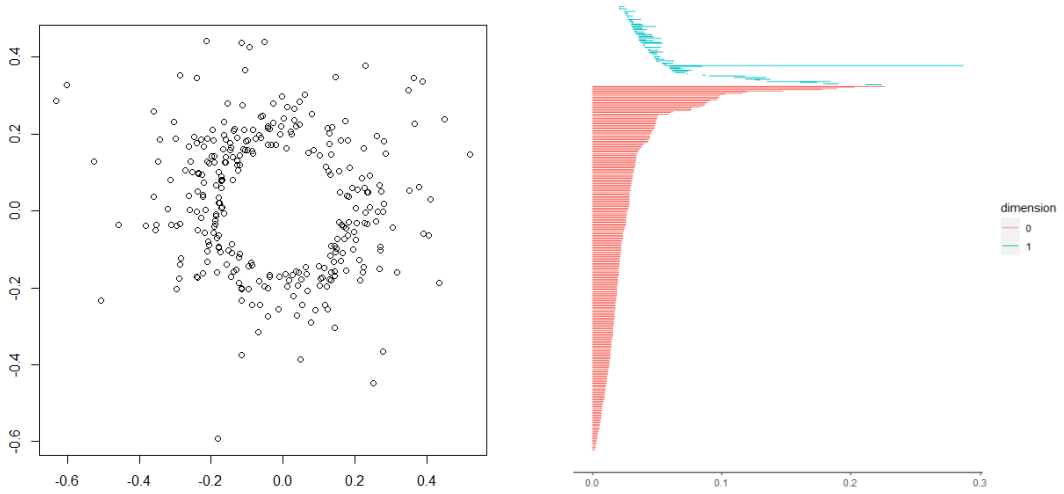

Figure 2.2: Exponential distribution of the radius parameter r'.

Example 2.1.3. A point-cloud of size 300 consisting of two arcs where $\theta_1, \theta_2, ..., \theta_n \sim U(0, 2\pi)$, and $r'_1, r'_2, ..., r'_n \sim Lognormal(\log(\frac{1}{2\pi}), 0.1)$. The arc of the smaller circle is of 225 points of radii $r'_{76}, r'_{77}, ..., r'_{300}$ and the arc of the larger circle is of 75 points with radius $r'_i = r'_1 + 0.2$, where $i \in \{1, 2, ..., 75\}$. The two long bars in dim 1 indicate the shape of two 1-spheres.

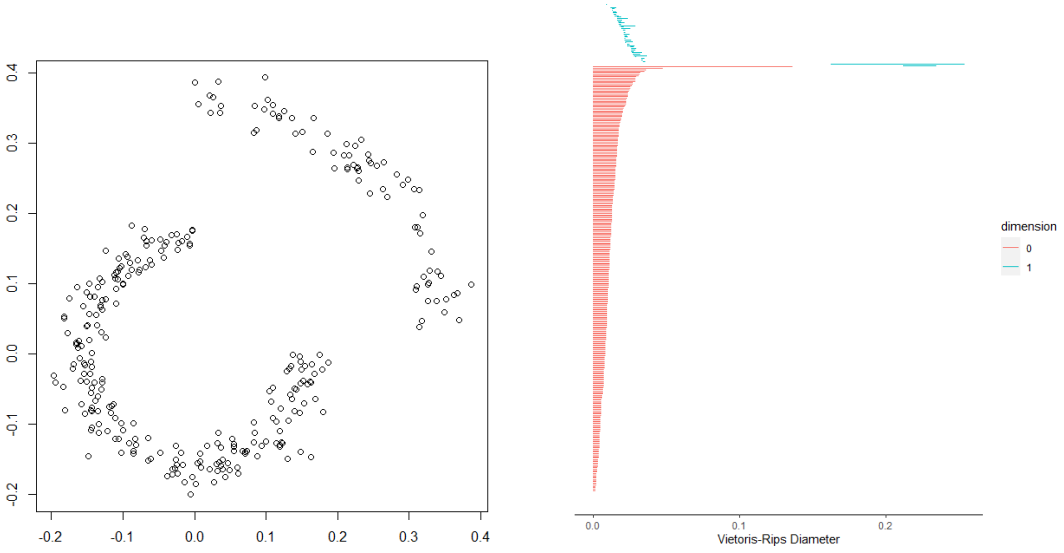

Figure 2.3

2.1.2 Approximating the death values of Vietoris-Rips complexes on the circle

It is proved that the Vietoris–Rips complex of the circle $\mathrm{VR}_r(S^1)$ obtains the homotopy types of the circle, the 3-sphere, the 5-sphere, the 7-sphere, etc., until finally it is contractible [AA17]. The death values, with respect to the geodesic metric given a circle of a unit circumference, are identified to be $\frac{1}{3}$, $\frac{2}{5}$, $\frac{3}{7}$, etc. Since the 'Ripser' code computes the homology using the Euclidean metric [Bau21], we need to interpret these distances with respect to the Euclidean metric.
To obtain the Euclidean distance between two points on an arc, suppose

$$x_1 = (r\cos(\theta_1), r\sin(\theta_1))$$
$$x_2 = (r\cos(\theta_2), r\sin(\theta_2))$$

then,

$$d = r\sqrt{(\cos(\theta_1) - \cos(\theta_2))^2 + (\sin(\theta_1) - \sin(\theta_2))^2}$$

can be simplified to

$$d = 2r\sin(\frac{\theta_1 - \theta_2}{2})$$

using the fact that

$$\cos(2x) = 1 - 2\sin^2(x)$$

2.1.2.1 Monte-Carlo simulations

Identifying the homotopy types of Vietoris-Rips complexes of the 2-Sphere is not easy. That is why one can start by trying to compute the homology first, which can be done by applying an experimental approach. To do so, we first start with the Vietoris-Rips complexes of the circle, whose homotopy types are all known. We do homology computations to investigate how the experimental outcomes approximate the true known theoretical death values. We later apply computations to predict the homology of Vietoris-Rips of the 2-Sphere. To experiment on the circle, we do Monte-Carlo simulations and apply inferential statistics to get approximations of the first three death values of Vietoris-Rips complexes of the circle of a unit circumference, i.e. the radius $r' = \frac{1}{2\pi}$ in a Euclidean metric. The finite point clouds were generated in two ways:

- Equidistantly distributed point-clouds, where the n-angles are equally dividing the interval $[0, 2\pi]$, and the corresponding Cartesian coordinates on a circle were computed, which results in a regular n-gon. The death values of homology classes of such point clouds are the blue dots in the coming simulation figures. See Figure 2.5, 2.6, and 2.7.

- Randomly, identically and independently distributed, point-clouds generated by taking a sample $\alpha_1, \ldots, \alpha_n$ i.i.d. $\sim U(0, 2\pi)$ and obtaining the Cartesian coordinates. The death values of the homology of such point clouds are the grey squares in the coming simulation figures. See Figure 2.5, 2.6, and 2.7.

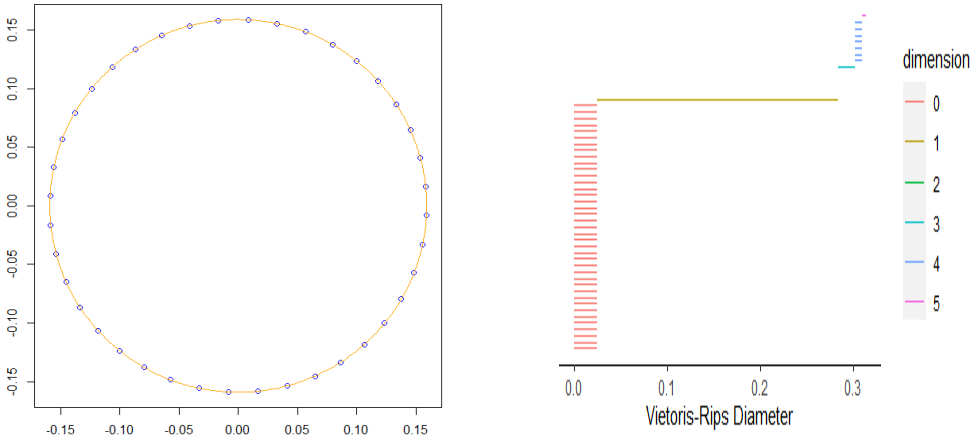

Figure 2.4: A 40-gon and its corresponding homology up to dim 6

Figure 2.4 is an example of a point cloud of 40 vertices equidistantly distributed around the circle of a unit circumference (right), and its corresponding barcodes computed up to dim 5 (left). Each odd dimension has one barcode, and the 7 bars we notice at dimension 4 will disappear once the size of the point cloud is increased.

First dimensional death value

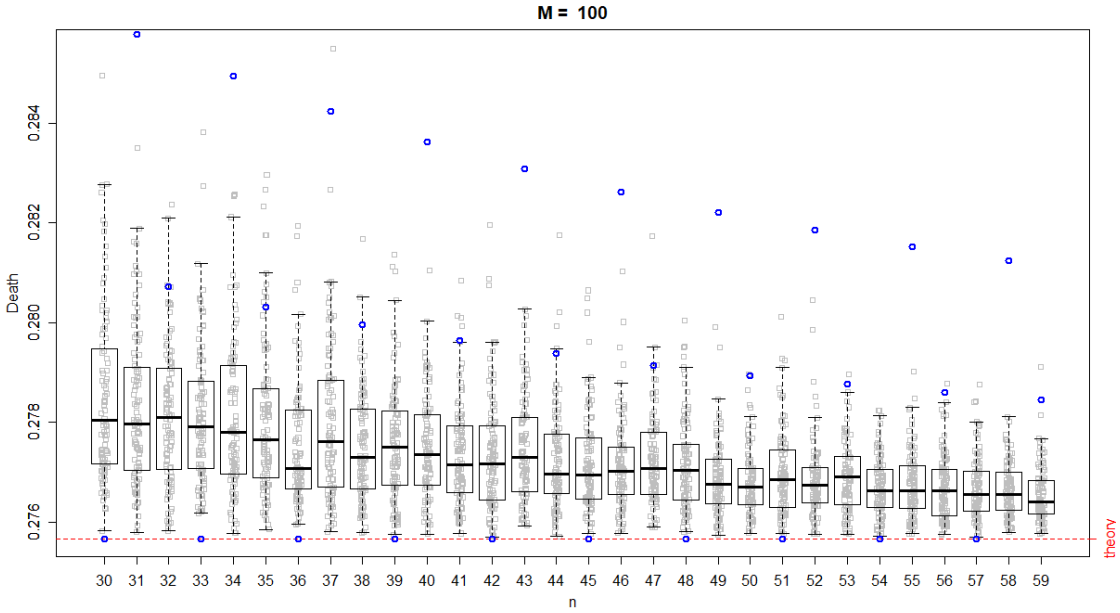

Figure 2.5: Monte-Carlo simulation of the first-dimensional death value.

Figure 2.5 illustrates the first death value of point clouds of sizes ranging from 30 to 59, with a Monte-Carlo simulation of size $M = 100$. i.e., for each n, we generated 100 point clouds that are randomly uniformly distributed on the circle of a unit circumference, and we represent its first-dimensional value with a grey square. Secondly, and for each n, we generate an equidistantly distributed point cloud and represent its first-dimensional value with a blue point.

We know from theory that the first-dimensional death value for a circle of a unit circumference equipped with a geodesic metric is $\frac{1}{3}$, which corresponds to

$$2r\sin(\frac{\pi}{3}) = 0.27566444771$$

in a Euclidean metric.

The first-dimensional death value is proven to be the edge length of an equilateral triangle inscribed in a circle, see [AA17]. In other words, having three equidistant points on the circle guarantees that we reach the minimum value that kills the first homology. Figure 2.5 clearly states that whenever the size of the equidistantly distributed point cloud is divisible by 3, the first death value hits the known theoretical value. Knowing that the smallest size of a point cloud that produces a first-dimensional homology barcode is 4, one obtains the exact death value

by fixing three equidistant points on the circle, and the fourth point can be randomly chosen. In conclusion, we do not need to have an equidistantly distributed point cloud of size divisible by 3, it is enough to have 3 equidistant points in any point cloud on the circle to capture the exact death value of the first dimension. It can also be seen that the simulation results for the 1-sphere allow in principle to estimate the upper bound for the theoretical death values.

Third dimensional death value

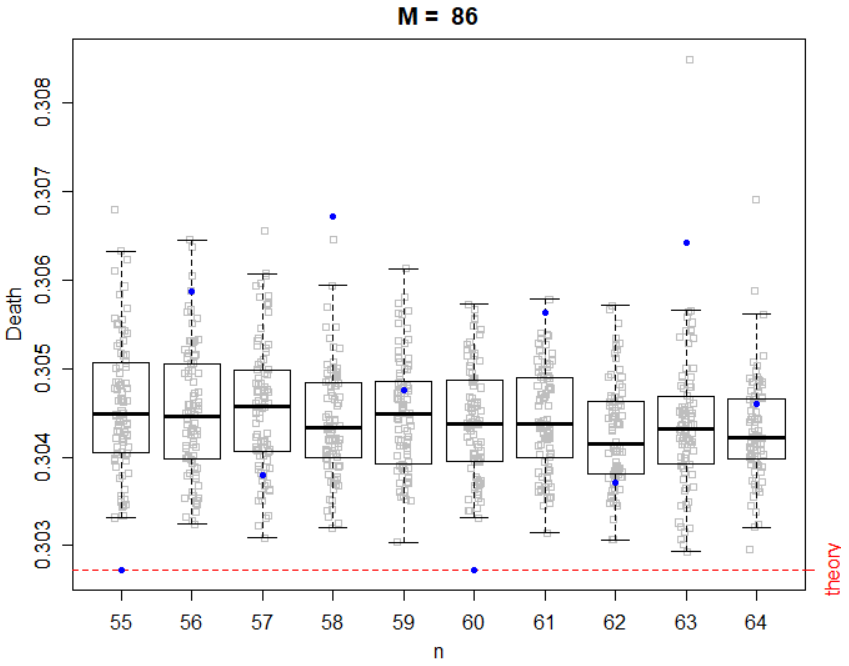

Figure 2.6: Monte-Carlo simulation of the third-dimensional death value.

Figure 2.6 illustrates the third-dimensional death value of point-clouds of size ranging from 55 to 64, with a Monte-Carlo simulation of size $M = 86$.

A similar approach has been conducted for the third-dimensional death value, $\frac{2}{5}$ on a geodesic metric, which is equivalent to

$$2r\sin(\frac{2\pi}{5}) = 0.30273069145$$

in a Euclidean metric.

The third-dimensional death value is the diagonal length of a pentagon inscribed in a circle, see [AA17]. The same observation is valid here as well; we need

five equidistant points to reach the minimum value that is able to kill the third homology. Hence, the outcome reveals that whenever the size of the equidistantly distributed point cloud is divisible by 5, the third death hits the known theoretical value. In other words, whenever our point cloud contains a pentagon, we get the exact third-dimensional death value.

Fifth dimensional death value

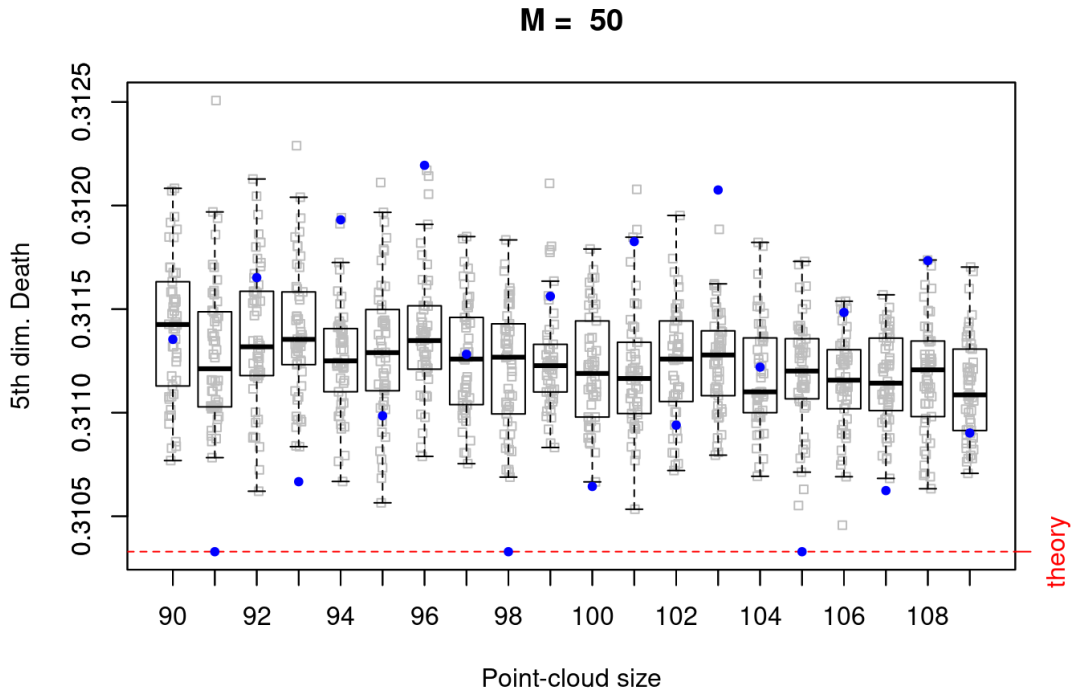

Figure 2.7: Monte-Carlo simulation of the fifth-dimensional death value.

Figure 2.7 illustrates the fifth death value of point clouds of size ranging from 90 to 109, with a Monte-Carlo simulation of size $M = 50$.

Similarly, the fifth dimensional death value, $\frac{3}{7}$ on a geodesic metric is equivalent to

$$2r \sin(\frac{3\pi}{7}) = 0.3103292$$

in a Euclidean metric.

The fifth-dimensional death value is the diagonal length of the longer diagonal of a heptagon inscribed in a circle, see [AA17]. The same observation is valid

here as well; we need seven equidistant points to reach the minimum value that is able to kill the fifth homology. Hence, the outcome reveals that whenever the size of the equidistantly distributed point cloud is divisible by 7, the fifth death hits the known theoretical value. In other words, whenever a point cloud obtains a heptagon, the exact fifth-dimensional death value is capturable.

Remark. Previous boxplots in Figure 2.5 reveal an asymmetric distribution that is skewed to the right.

As a next step, one can try to fit a distribution for each sample of a fixed size of a point cloud. The most suitable candidate of a predefined set of distributions was always suggested to be a beta distribution of different shape parameters α and β. But these two parameters were not both of large values to allow of a convergence of a beta distribution to a normal one. One can see this in the following case.

For instance, consider generating 100 point clouds each of size 60 representing S^1, and computing the third-dimensional homology of $\mathrm{VR}_r(S^1)$, then considering the collected death values as a sample. For fitting a distribution to this obtained data set, we observe its empirical distribution, which is a useful tool in guessing the best distribution candidate in the case of the absence of knowledge of the underlying stochastic process that governs this data set.

Plotting its empirical density and cumulative distribution we get:

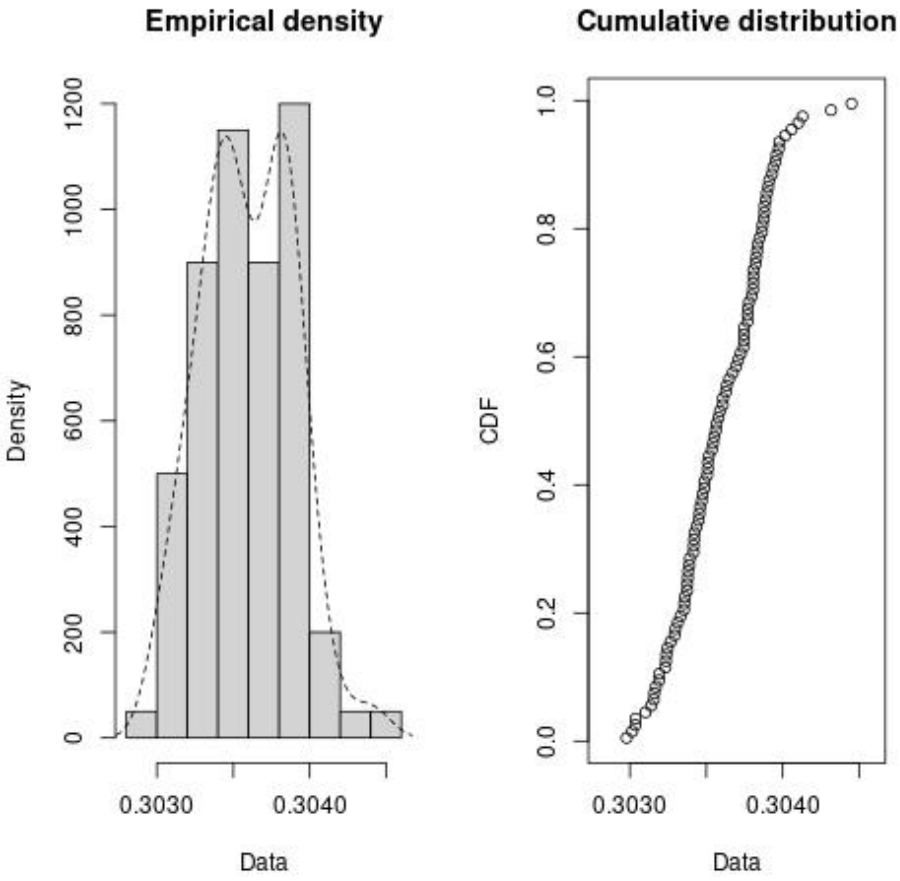

Figure 2.8: Histogram and CDF plots of an empirical distribution for the random sample of 100 third-dimensional death values.

In addition to empirical plots, descriptive statistics may help to choose candidates to describe a distribution among a set of parametric distributions. Useful tools for this purpose are the skewness and kurtosis notions, where the former is a measure of symmetry or asymmetry of data distribution, and the latter measures whether data is heavy-tailed or light-tailed relative to a normal distribution. Therefore, for fitting a distribution for our sample, it is efficient to consider the Cullen and Frey graph. On this graph, values for common distributions are displayed to help us choose a distribution to fi

t to our data. For distributions like normal, uniform, logistic, or exponential, there is only one possible value for the skewness and the kurtosis and these are represented by points on the graph. For other distributions, areas of possible values are represented by either lines as for gamma and lognormal distributions, or by larger areas like the beta distribution. Skewness and kurtosis are known

to be sensitive to outliers and to take into consideration the uncertainty of the estimated values of kurtosis and skewness from data, we perform a nonparametric bootstrap procedure, i.e., by random sampling with replacement from the original data, which is represented in the graph as the yellow area. For further insight, we direct the reader to [DMD15] and [DMDP$^+$15].

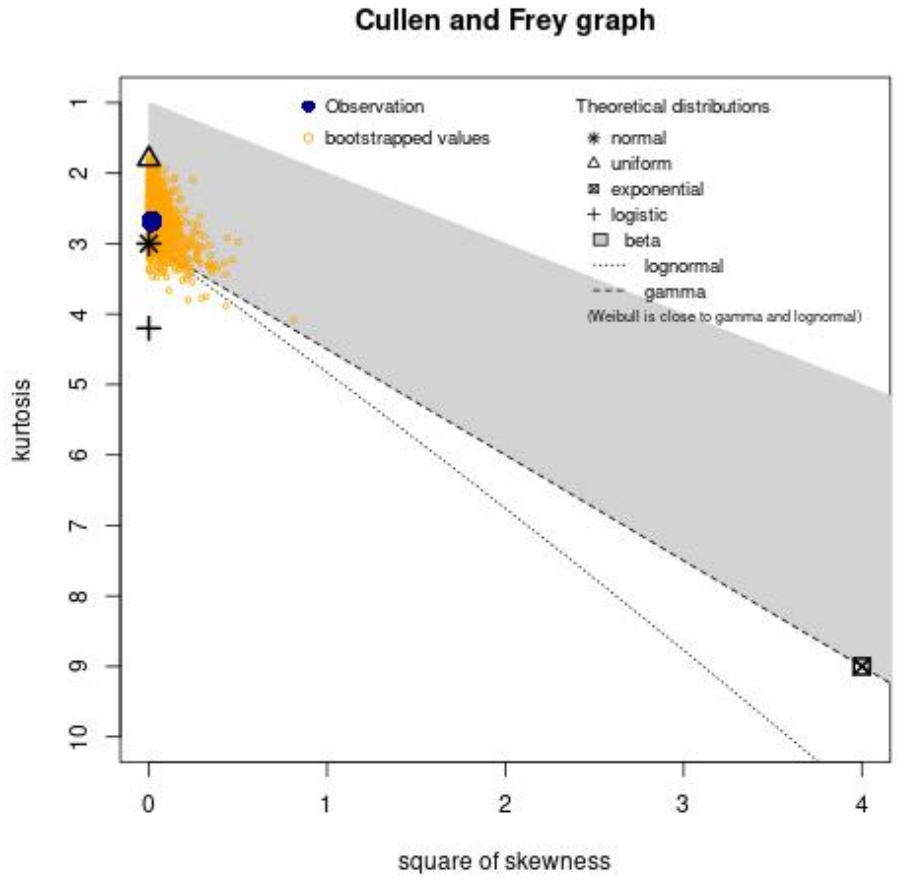

Figure 2.9: kewness-kurtosis plot for the random sample of size 100.

One can see that the estimated skewness is 0.132, and since it is a non-zero, it reveals a lack of symmetry in the empirical distribution. The estimated kurtosis is 2.687, which quantifies the weight of tails in comparison to the normal distribution which has a kurtosis value of 3.

The graph suggests that a beta distribution is an appropriate one. We tried to fit a normal and gamma distribution and compared the values of AIC and BIC of each distribution. We noticed that the beta distribution is the one that yields the minimum AIC and BIC values. For more on AIC and BIC, we direct the reader

to [AB04].
Given this, we get that our sample $X \sim B(723454.2, 1659516)$, with an expected death value

$$E[X] = \frac{\alpha}{\alpha + \beta} = 0.3035935$$

Since we have a considerably large sample size, the central limit theorem applies, which results in the distribution of the sample mean being approximately normal. Therefore, we can consider having a student confidence interval for the death value μ we want to approximate.
For this example, we get the confidence interval $[0.3035148, 0.3036721]$. Note that the first-dimensional death value is known from theory to be 0.30273. The confidence interval indicates that the value we are trying to estimate has 0.3035148 as an upper bound. Estimating the first-dimensional death value is about estimating the infimum/minimum of a compact distribution support in $\mathbb{R}$, i.e., the edge of a parameter space, which is known to be a difficult problem.

2.1.2.2 Fitting regression models to approximate the death values

A second method to approximate the death values of dimensions 1, 3, and 5 of the circle is fitting a regression model for the simulations in Figures 2.5, 2.6, and 2.7. For each simulation, we first fit a linear regression model for the whole samples, we then divide the equidistantly distributed point clouds (blue dots) to different subsets and we fit a linear regression model for each layer. For a deeper insight into linear regression, we direct the reader to see [SL03].

Regression model for the first dimensional death value

Fitting a regression model for the obtained data of Figure 2.5, where n is the size of the point cloud and the response variable is the death value. One starts with the natural expression $Death \simeq n$, and try other linear transformations or polynomial forms, and finally get that a rational model of the form:

$$Death \simeq 0.27720908 + 0.05813695 \, \frac{1}{n}$$

is a good fit with the highest obtained Adjusted R-squared value equals 0.3764.

Grouping the obtained death values coming from equidistantly distributed point clouds into 3 samples and fitting regression models for each sample yields:

$$Death \simeq \begin{cases} 0.27566444771 & n \equiv 0 \ (mod 3) \\ 0.2760303 + 0.3017427\frac{1}{n} & n \equiv 1 \ (mod 3) \\ 0.2757500 + 0.1590706\frac{1}{n} & n \equiv 2 \ (mod 3) \end{cases}$$

Where the second two models fulfill perfect fitting because the value of the Adjusted R-squared equals 1.

Regression model for the third-dimensional death value

Implementing a similar approach to data of Figure 2.6, a general model is obtained:

$$Death \simeq 0.304352935 + 0.002930902 \ \frac{1}{n}$$

with an Adjusted R-squared of value 0.02606.

Grouping the obtained death values coming from equidistantly distributed point clouds into 5 samples and fitting regression models for each sample yields:

$$Death \simeq \begin{cases} 0.30273069145 & n \equiv 0 \ (mod 5) \\ 0.3028778 + 0.1675509\frac{1}{n} & n \equiv 1 \ (mod 5) \\ 0.30274644 + 0.05985787\frac{1}{n} & n \equiv 2 \ (mod 5) \\ 0.3029946 + 0.2153477\frac{1}{n} & n \equiv 3 \ (mod 5) \\ 0.3027943 + 0.1157954\frac{1}{n} & n \equiv 4 \ (mod 5) \end{cases}$$

The last four models are of a perfect fit as well since the Adjusted R-squared value is 1.

For instance, if we have a point-cloud of size 100003, substituting this in the general model gives $Death \simeq 0.304353$, and when we substitute it in the fourth branch where $n \equiv 3(mod 5)$, we get $Death \simeq 0.3029968$, which is closer to the true value 0.30273069145.

Regression model for the fifth-dimensional death value

A general model of the simulation in Figure 2.7 given by:

$$Death \simeq 0.3100055 + 0.1234374\frac{1}{n}$$

is a good fit with an Adjusted R-squared of value 0.061.

Grouping the obtained death values coming from equidistantly distributed point clouds into 7 samples and fitting regression models for each sample yields:

$$Death \simeq \begin{cases} 0.311028 & n \equiv 0 \ (mod 7) \\ 0.311573 - 0.022637\frac{1}{n} & n \equiv 1 \ (mod 7) \\ 0.3103 + 0.03056\frac{1}{n} & n \equiv 2 \ (mod 7) \\ 0.3104 + 0.1428\frac{1}{n} & n \equiv 3 \ (mod 7) \\ 0.3103 + 0.06141\frac{1}{n} & n \equiv 4 \ (mod 7) \\ 0.3104 + 0.1681\frac{1}{n} & n \equiv 5 \ (mod 7) \\ 0.31159 - 0.51765\frac{1}{n} & n \equiv 6 \ (mod 7) \end{cases}$$

Where the models, where $n \equiv 2, 3, 4$ and 5, fulfill a perfect fit since the Adjusted R-squared is 1.

Remark. The winding fraction of a cyclic graph $\overrightarrow{G}$ is

$$wf(\overrightarrow{G}) = sup\ \{\frac{k}{n} : there\ exists\ a\ cyclic\ homomorphism\ \overrightarrow{G_n^k} \to \overrightarrow{G}\},$$

$\overrightarrow{G_n^k}$ is a Vietoris–Rips graph of the vertex set of a regular n-gon, where

$$\overrightarrow{G_n^k} = \overrightarrow{\mathrm{VR}}(\{0, \frac{1}{n}, ..., \frac{n-1}{n}\}; \frac{k}{n})$$

For further explanation about the winding fraction, we direct the reader to the articles [AAM17] and [AA17]. The winding Fraction appears in the regression models in the intercept term. Expressing the coefficient term with the winding fraction might also be possible.

$$Death_k \simeq 2r \sin(wf(k)) + coef.\frac{1}{n}$$

2.2 Vietoris-Rips of the 2-Sphere

In this section, we compute the homology of the Vietoris-Rips complexes of the 2-Sphere. We first explain the generating mechanism of the point clouds, we then present some computational outcomes of different Thomson solids, and later we try to estimate the death value of dimension 3.

2.2.1 Point-clouds approximating the 2-Sphere

We present three ways for generating a point cloud on the sphere S^2. The first two methods produce point clouds that are somehow $''evenly''$ distributed, whereas the third method induces random samples of the uniform distribution on S^2.

- Point-clouds coming from the Thomson Problem, which is concerned in determining the minimum electrostatic potential energy configuration of $n-$electrons constrained to the surface of a unit sphere that repel each other with a force given by Coulomb's law.

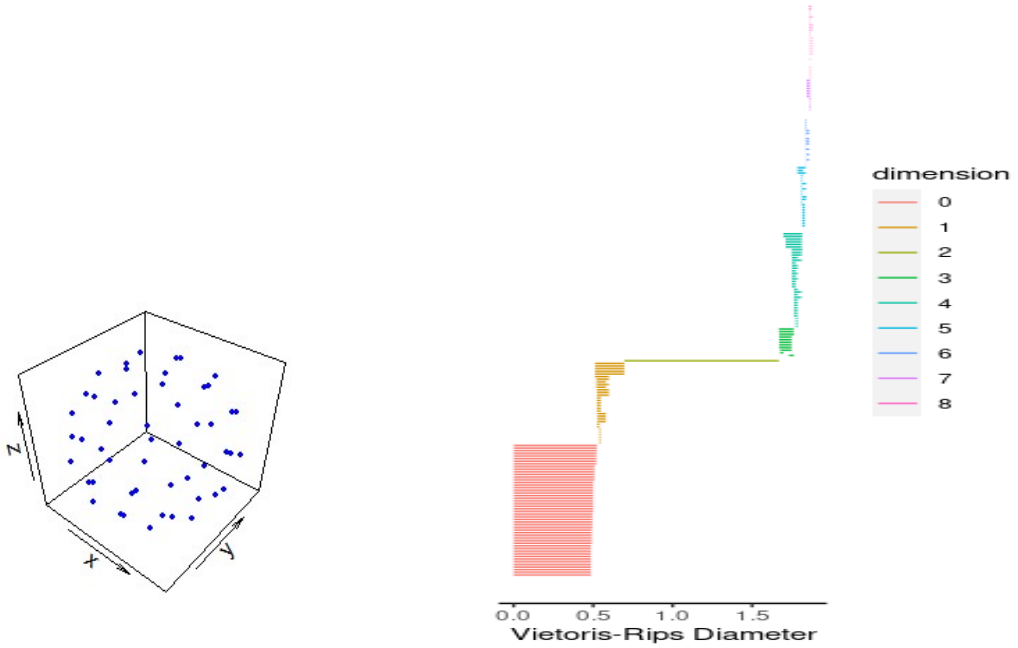

Figure 2.10: Thomson solid of 51 vertices and its corresponding homology up to dim 8

- Point-clouds coming from mapping the Fibonacci lattice (aka Golden Spiral, aka Fibonacci Sphere) onto the surface of a sphere, where the Fibonacci

lattice evenly distributes points inside a unit square $[0,1)^2$, and to produce the Fibonacci spiral, aka the Golden Spiral, one simply maps this point distribution from the unit square to the sphere by the cylindrical equal-area projection:

$$(x, y) \to (\theta, \phi) : (2\pi x, \arccos(1 - 2y))$$

$$(\theta, \phi) \to (x, y, z) : (\cos\theta \sin\phi, \cos\phi \sin\theta, \cos\phi)$$

where $\theta \in [0, 2\pi]$ is longitude, and $\phi \in [0, \pi]$ is the angel from North pole.

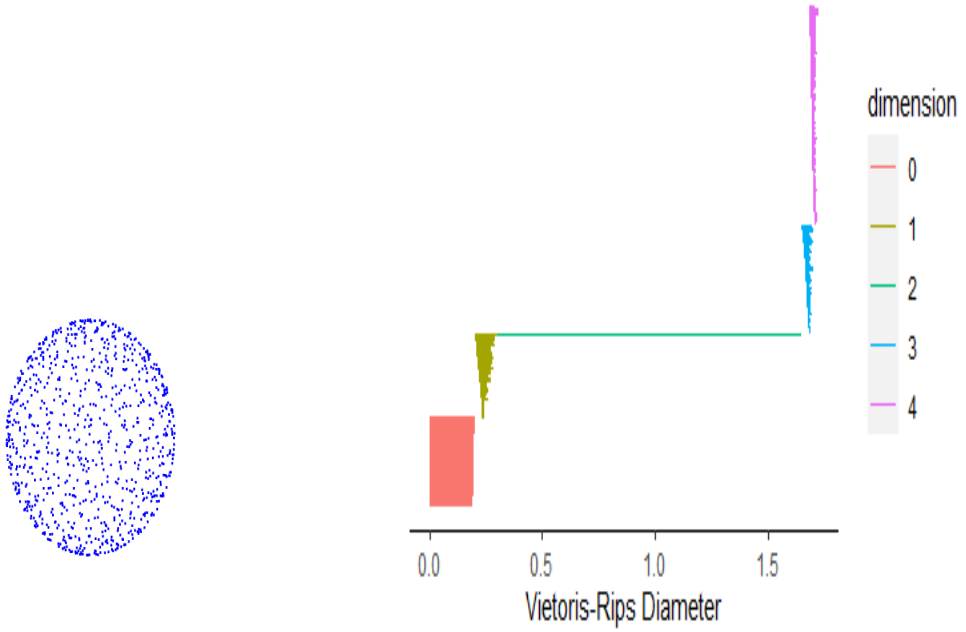

Figure 2.11: Fibonacci Sphere of size 300 and its corresponding homology up to dim 4.

Uniform Distribution

- Point-clouds coming from uniformly distributed points on a unit sphere. One of the ways to obtain such a sample is to generate three standard normally distributed numbers X, Y, and Z to form a vector $V = [X, Y, Z]$. Intuitively, this vector will have a uniformly random orientation in space but will not lie on the sphere. By normalizing the vector $V := \frac{V}{\|V\|}$, one obtains the desired sample.

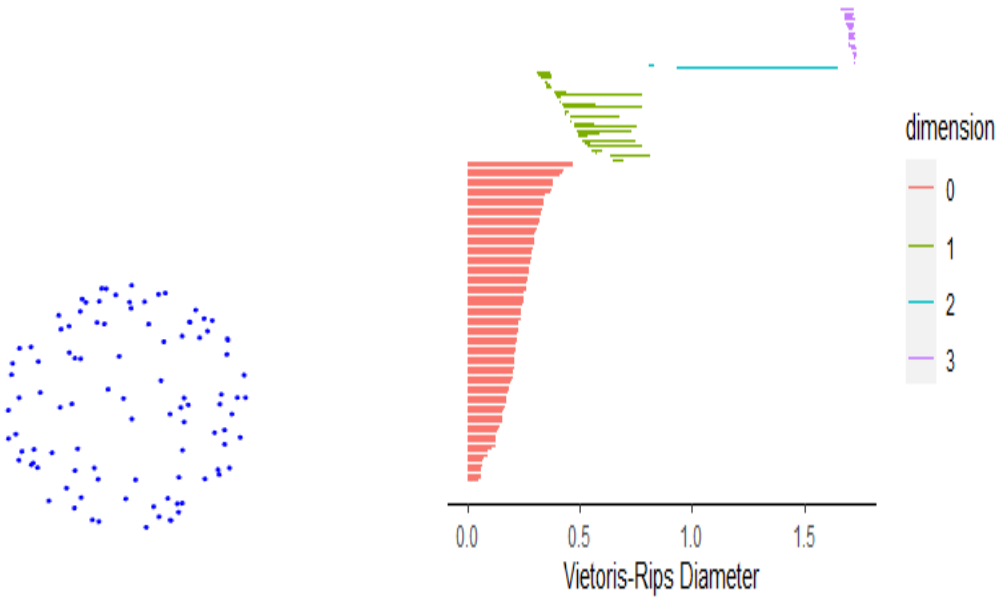

Figure 2.12: A uniform point-cloud of size 100 its corresponding homology up to dim 3

One may also inscribe polyhedra like Catalan or Archimedean solids in the unit sphere and compute their homology. The following figure represents the barcodes of a disdyakis triacontahedron, which has the highest sphericity of approximately 0.9857.

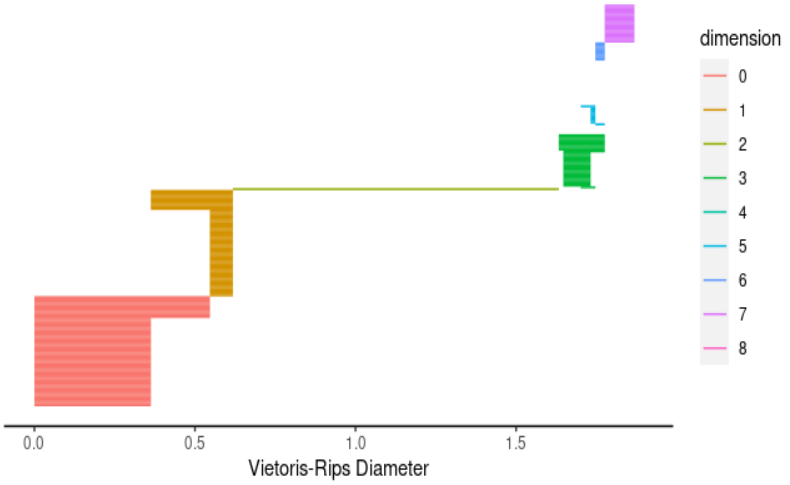

Figure 2.13: The first eight barcodes of the disdyakis triacontahedron inscribed in a unit sphere.

2.2.2 Computational outcomes

All computations were done on JustHPC, a Linux high-performance cluster of University of Giessen, using Ripser C++ code with robin-hood-hashing.

We acknowledge computational resources provided by the HPC Core Facility and the HRZ of the Justus-Liebig-University Giessen. We also thank Dr. Marcel Giar from the administration team of JustHPC for his technical support in running the computations.

JustHPC has 5 partitions:

- serial, single, debug, and regular: each one of them has 248 available nodes with a node configuration of 24 cores, 192 GiB RAM, $\sim$ 750 GiB temporary HDD space.
- bigmem has 4 available nodes with a node configuration of 48 cores, 1.5 TB RAM, $\sim$ 6 TB temporary HDD space.

On all except the 'debug' partition, one may choose among three so-called qualities of service. These modify the maximum allowable runtime of the jobs and their priority. The three length options are:

- short, with a time limit of 12 hours and max. 12 nodes per job.
- normal, with a time limit of 5 days and max. 2 nodes.
- bigmem with an unlimited time.

The following summarized computations were done using a single short partition, except for Thomson 100 and 1500, they were assigned to the bigmem partition.

The following tables represent the minimum and the maximum value of each birth and death of computed persistent homology of Thomson solids of different sizes. The radius r ranges in $[0, 2]$ and the closing radius is the value where the Vietoris-Rips complex becomes contractible to a point.
The plot of the barcodes of each table is given in Appendix A.

Thomson 35

Dimension	min. birth	max. birth	min. death	max. death
0	0	0	0.5697090	0.6353726
1	0.6050468	0.6407641	0.6343331	0.8217621
2	0.8217621	0.8217621	1.7241240	1.7241240
3	1.7241240	1.7586649	1.7611883	1.8181563
4	1.7805049	1.8082616	1.8001861	1.8288708
5	1.8001861	1.8458177	1.8354526	1.8499196
6	1.8387538	1.8534091	1.8510235	1.8602050
7	1.8602050	1.8636544	1.8625656	1.8644397
8	1.8664440	1.8702658	1.8708964	1.8819435
9	1.8819435	1.9252281	1.9173999	1.9303325
10	1.9303325	1.9303325	1.9308187	1.9308187
11	1.9393601	1.9393601	1.9542417	1.9542417
12	1.9542417	1.9542417	1.9551034	1.9551034
15	1.9632013	1.9632013	1.9722432	1.9722432

Table 2.1: Thomson 35 and its corresponding homology up to dim. 15.
The closing radius: 1.9722432.
Memory consumption: 1.49 GB
Time consumption: 00:03:19.

Thomson 40

Thomson 40 is the largest size of a point cloud that we were able to compute all its homology.

Dimension	min. birth	max. birth	min. death	max. death
0	0	0	0.549871	0.585176
1	0.563330	0.585176	0.624521	0.659573
2	0.659573	0.659573	1.632990	1.632990
3	1.731070	1.731320	1.763160	1.789470
4	1.789470	1.789470	1.789470	1.789470
5	1.731070	1.789470	1.763160	1.813910
6	1.798660	1.813910	1.813910	1.887530
7	1.813910	1.887530	1.840520	1.887530
8	1.887530	1.887530	1.900370	1.900370
9	1.900370	1.900370	1.942700	1.942700
12	1.942700	1.942700	1.960580	1.960580
17	1.960580	1.960580	1.966080	1.966080

Table 2.2: Thomson 40 and its corresponding homology up to dim. 17.
The closing radius: 1.96608.
Memory consumption: 23.6 GB.
Time consumption: 00:57:49.

Thomson 50

Dimension	min. birth	max. birth	min. death	max. death
0	0	0	0.495882	0.545191
1	0.504665	0.558085	0.545191	0.615537
2	0.615537	0.615537	1.639110	1.639110
3	1.639110	1.721920	1.724280	1.780980
4	1.724280	1.780980	1.788100	1.796330
5	1.796330	1.796330	1.850080	1.850080
6	1.788100	1.850080	1.847590	1.868500
7	1.857340	1.868500	1.866730	1.868500
8	1.868500	1.868500	1.872970	1.872970
9	1.872970	1.872970	1.876670	1.924260
10	1.924260	1.924260	1.932660	1.932660

Table 2.3: Thomson 50 and its corresponding homology up to dim. 10.
The closing radius: 1.98148.
Memory consumption: 137.29 GB.
Time consumption: 02:29:57.

Thomson 65

Dimension	min. birth	max. birth	min. death	max. death
0	0	0	0.424812	0.458688
1	0.442157	0.478691	0.483655	0.616187
2	0.616187	0.616187	1.691610	1.691610
3	1.691610	1.734110	1.722040	1.737280
4	1.734010	1.767790	1.737790	1.768900
5	1.754350	1.785240	1.761560	1.788680
6	1.787940	1.811480	1.797110	1.829220
7	1.819820	1.852420	1.826000	1.854750

Table 2.4: Thomson 65 and its corresponding homology up to dim. 7.
The closing radius: 1.98142.
Memory consumption: 7.37 GB.
Time consumption: 00:17:56.

Thomson 100

Dimension	min. birth	max. birth	min. death	max. death
0	0	0	0.352396	0.383677
1	0.357705	0.383677	0.390532	0.482218
2	0.482218	0.482218	1.632990	1.632990
3	1.636730	1.705430	1.687960	1.751330
4	1.702780	1.731560	1.710920	1.754280
5	1.705440	1.773650	1.745810	1.777130
6	1.767640	1.802620	1.778700	1.819400

Table 2.5: Thomson 100 and its corresponding homology up to dim. 6.
The closing radius: 1.98786.
Memory consumption: 702.18 GB.
Time consumption: 04:17:21.

Thomson 150

Dimension	min. birth	max. birth	min. death	max. death
0	0	0	0.285337	0.304685
1	0.295609	0.314781	0.316185	0.382101
2	0.382101	0.382101	1.663030	1.663030
3	1.663030	1.699040	1.663030	1.718270
4	1.683620	1.726580	1.721740	1.767070
5	1.683620	1.769160	1.755450	1.781500

Table 2.6: Thomson 150 and its corresponding homology up to dim. 5.
The closing radius: 1.99408
Memory consumption: 12.71 GB.
Time consumption: 01:09:31.

Thomson 400

Dimension	min. birth	max. birth	min. death	max. death
0	0	0	0.175495	0.188676
1	0.184148	0.193075	0.195073	0.214212
2	0.214212	0.214212	1.632990	1.632990
3	1.637600	1.684280	1.668550	1.717450
4	1.679850	1.717450	1.686580	1.717450

Table 2.7: Thomson 400 and its corresponding homology up to dim. 4.
The closing radius: 1.99704
Memory consumption: 143.77 GB.
Time consumption: 00:43:14.

Thomson 1500

Dimension	min. birth	max. birth	min. death	max. death
0	0	0	0.0884814	0.0984626
1	0.0904052	0.100609	0.0988558	0.1221700
2	0.1221710	0.122171	1.6356000	1.6356000
3	1.6356000	1.662170	1.6460900	1.6716600

Table 2.8: Thomson 1500 and its corresponding homology up to dim. 3.
The closing radius: 1.99915
Memory consumption: 252.11 GB.
Time consumption: 15:32:41.

Rhombic triacontahedron

It is a Catalan solid of 32 vertices that includes the arrangement of four Platonic solids. It contains ten tetrahedra, five cubes, an icosahedron, and a dodecahedron. The centers of the faces contain five octahedra.

Dimension	min. birth	max. birth	min. death	max. death
0	0	0	0.640852	0.640852
1	0.640852	0.640852	0.713644	0.713644
2	0.713644	0.713644	1.632990	1.632990
3	1.632990	1.701300	1.868340	1.868340
5	1.701300	1.868340	1.894550	1.894550
8	1.894550	1.894550	1.894550	1.894550
9	1.868340	1.894550	1.894550	1.894550
15	1.894550	1.894550	2	2

Table 2.9: Rhombic triacontahedron and its homology up to dim. 15.
The closing radius: 2
Memory consumption: 17.22 GB.
Time consumption: 00:32:00.

Its barcodes are plotted in A.1 as well.

- Computing homology of Thomson 32 yields the same results obtained from the rhombic triacontahedron.
- Computing homology for point clouds consisting of an inscribed icosahedron with a set of points that are randomly uniformly generated always give the fifth birth value to be 1.701302.

- Computing homology for point clouds consisting of an inscribed dodecahedron with a set of points that are randomly uniformly generated always give the ninth birth value to be 1.8683447.

In Section 2.1.2.1 we have concluded that the first-dimensional death value of $\mathrm{VR}(S^1)$ is capturable once the point-cloud has an inscribed equilateral triangle, and the third-dimensional death value is also capturable if the point-cloud has an inscribed pentagon. Similarly, for the fifth-dimensional death value to be obtained, a heptagon is required to be inscribed. In a generalized scope, it is proven that an inscribed regular n-gon in a point cloud approximating the circle kills the (n-2)th-dimensional homology, where $3 \leqslant n$.
For $\mathrm{VR}(S^2)$, we see in detail in Chapter 3 that the platonic solids play a major role in identifying the homology of the 2-Sphere. From the computations listed above, we observe that the value 1.1701302 is the birth of the fifth-dimensional homology of $\mathrm{VR}_r(S^2)$, and that the value 1.8683447 is the birth of the ninth-dimensional homology of $\mathrm{VR}_r(S^2)$. Similar observations in the 2-Sphere case are also valid: generating random point clouds that have an inscribed icosahedron fixes the birth of the fifth-dimensional homology, and generating random point clouds that have an inscribed dodecahedron fixes the birth of the ninth-dimensional homology. Therefore, we conjecture the following:

Conjecture 2.2.1.
- The birth value of the fifth-dimensional homology of $\mathrm{VR}(S^2)$ is 1.701302, which is the length of the face diagonal of an inscribed icosahedron in a unit sphere. See Table 3.3.

- The birth value of the ninth-dimensional homology of $\mathrm{VR}(S^2)$ is 1.8683447, which is the length of the medium space diagonal of an inscribed dodecahedron in a unit sphere. See Table 3.3.

Note that a point cloud of a small size, like Thomson 40 for instance, is able to catch the exact second-dimensional death value. Thomson 100 with its fifth min. birth shows a value that asserts our conjecture.

2.2.3 Approximating the third dimensional death values

It has been proved that the second-dimensional death value is the diameter of a 3-simplex, which equals 1.632993 in Euclidean metric when inscribed in a unit sphere [LMO20, Theorem 10]. In order to be able to approximate the death value of dimension 3 of Vietoris-Rips complexes of S^2, we consider Thomson solids of sizes varying between 60 to 1500, compute the homology of each solid up to dim 3, and consider that each sample consists of the length of the third-dimensional barcodes. In a similar fashion to circle samples, we get that a beta distribution

is the most appropriate one. We fit a beta distribution and compute its expected mean value. The following table summarizes the results:

Thomson	Sample Size	Expected Mean
60	15	0.027581758
70	15	0.018573078
80	43	0.022211692
90	28	0.031210385
100	36	0.018402231
110	55	0.024939617
120	93	0.036498791
150	93	0.012059799
200	182	0.017035564
250	237	0.013924825
300	298	0.011999938
350	338	0.010995290
400	498	0.017907976
500	606	0.010101854
1500	4122	0.007226794

We get a 95%−Student's Confidence Interval for the length of the 3-dimensional barcode

$$[0.01406937, 0.02335324]$$

Hence, the third-dimensional death value is expected to lie in the interval

$$[1.647063, 1.656346]$$

We anticipated the vanishment of the expected mean, as it is conjectured in [AAF18, Remark 5.6, and Conjecture 5.7]. Although the death value decreases by the increase of the sample size, the chosen point clouds seem to be insufficient to indicate evidence that the third-dimensional bars are all noise. Due to computational limitations, we were restricted to point clouds of such small sizes.

We have seen in this chapter to which extent are computational outcomes of homology in the circle case coincide with the theoretical results. We attempted to transfer the previous findings to the 2-Sphere case by computing the homology of point clouds approximating the 2-Sphere, and we conjectured about the birth values of the fifth and ninth homology of $\mathrm{VR}(S^2)$.

Chapter 3

Homotopy types of Vietoris Rips complexes of Platonic Solids

We have seen that the regular n-gons, where n is odd, played a vital role in identifying the homotopy types of the circle. In this chapter, we will observe that Platonic solids play an important role in identifying the homology of the 2-Sphere. This chapter is joint work with Prof. Stefan Witzel and the Ph.D. student Thomas Titz-Mite and is based on the article [SMW23b].

3.1 Cross-Polytopes and their boundaries

Definition 3.1.1. An n-cross-polytope is a regular, convex polytope that exists in an n-dimensional Euclidean space, [Cox73]. It has $2n$-vertices of permutations of the coordinates $(\pm 1, 0, 0, ..., 0)$ with an edge length $\sqrt{2}$, and bounded by (cells consists of) 2^n simplices of dimension $(n-1)$. The number of k-simplices contained in an n-cross-polytope is $\binom{n}{k+1}2^{k+1}$.

Cross-polytopes are one of the three regular polytope families, the other two being the hypercubes and the simplices.
An n-dimensional polytope has topologically the $(n-1)$-sphere as its boundary.
To avoid ambiguity, it might be worth mentioning that, in many references, an n-cross-polytope would be denoted by β_n, which is the same notion used to refer to the betti numbers.

Cross-Polytope	Name	Vertices	Boundary
β_0	Point	1	ϕ
β_1	Line	2	S^0
β_2	Square	4	S^1
β_3	Octahedron	6	S^2
β_4	16-Cell	8	S^3
β_5	Pentacross	10	S^4

Table 3.1: The first five cross-polytopes, their names, number of vertices, and their boundary spheres.

3.2 Regular Polyhedra in three-dimensional Euclidean space

The five convex, regular polyhedra in a three-dimensional Euclidean space are: Tetrahedron, Cube, Octahedron, Dodecahedron, and Icosahedron.
In this section, we study the homology of Vietoris-Rips complexes $\mathrm{VR}_r := \mathrm{VR}_{\leqslant}(P^{(0)}; r)$ of each polyhedron.
We will consider a platonic solid P, that has the vertex set $P^{(0)}$ and let m, n, v, f, k denote its fundamental invariants, where the numbers m and n are the vertices around a facet and the facets around a vertex, respectively. The numbers v and f are the numbers of vertices and facets respectively. The number k is the diameter of the edge graph.
We provide the three combinatorial, Euclidean, and spherical distances of each polyhedron. However, we consider the combinatorial distance since we will be dealing with the edge graph of the polytope.

Polytope	m	n	v	f	k
Tetrahedron	3	3	4	4	1
Cube	4	3	8	6	3
Octahedron	3	4	6	8	2
Dodecahedron	5	3	20	12	5
Icosahedron	3	5	12	20	3

Table 3.2: Basic combinatorics of the platonic solids.

Polytope	combinatorial	Euclidean	spherical
Tetrahedron	1	$\sqrt{\frac{8}{3}} = 1.632993$	$\arccos(-\frac{1}{3})$
Cube	1	$\sqrt{\frac{4}{3}} = 1.154701$	$\arccos(\frac{1}{3})$
	2	$\sqrt{\frac{8}{3}} = 1.632993$	$\arccos(-\frac{1}{3})$
	3	2	$\pi = \arccos(-1)$
Octahedron	1	$\sqrt{2} = 1.414214$	$\frac{\pi}{2} = \arccos(0)$
	2	2	π
Dodecahedron	1	$\frac{2}{\sqrt{3}\phi} = 0.7136442$	$\arccos(-\frac{1-\phi^4}{3\phi^2})$
	2	$\sqrt{\frac{4}{3}} = 1.154701$	$\arccos(\frac{1}{3})$
	3	$\sqrt{\frac{8}{3}} = 1.6329932$	$\arccos(-\frac{1}{3})$
	4	$\frac{2\phi}{\sqrt{3}} = 1.8683447$	$\arccos(\frac{1-\phi^4}{3\phi^2})$
	5	2	π
Icosahedron	1	$\sqrt{\frac{4}{\phi\sqrt{5}}} = 1.051462$	$\arccos(\frac{1}{\sqrt{5}})$
	2	$\sqrt{\frac{4\phi}{\sqrt{5}}} = 1.701302$	$\arccos(-\frac{1}{\sqrt{5}})$
	3	2	π

Table 3.3: The combinatorial, Euclidean, and spherical distances, respectively. Euclidean and spherical distance refer to the polytope inscribed in the unit sphere, where $\phi = \frac{1+\sqrt{5}}{2}$ is the golden ratio.

The following are the barcodes of the platonic solids inscribed in a unit sphere.

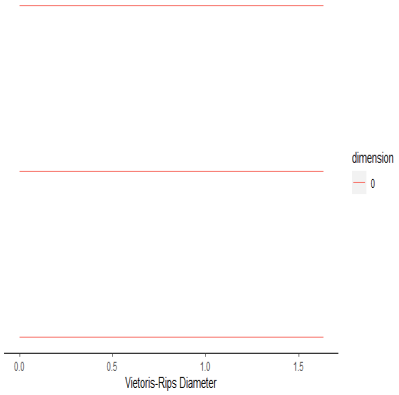

Figure 3.1: Barcodes of a regular tetrahedron inscribed in a unit sphere.

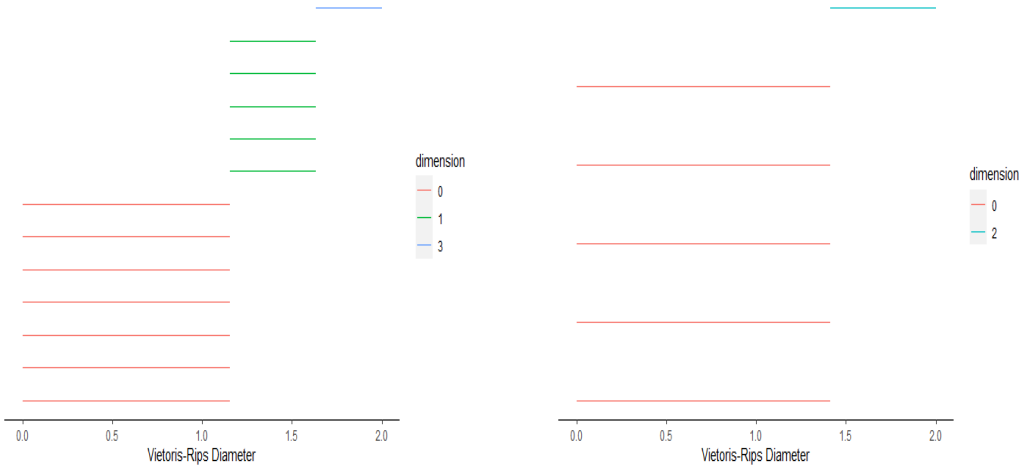

Figure 3.2: Barcodes of a cube, (left), and an octahedron, (right), inscribed in a unit sphere.

The 5 copies of barcodes in the first dimension of the cube represent the number of its faces, it has 6 faces but we see only 5 copies since the sixth face can be written as a linear combination of the other 5 ones.

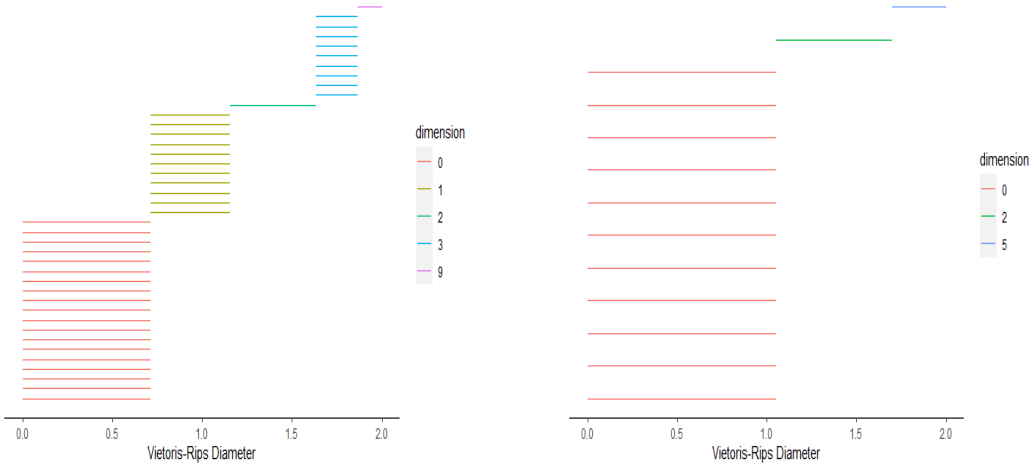

Figure 3.3: Barcodes of a dodecahedron, (left), and an icosahedron, (right), inscribed in a unit sphere.

Similarly, the 11 copies of barcodes in the first dimension of the dodecahedron represent the number of its faces. It has 12 faces, and we notice only 11 copies because the twelfth face can be written as a linear combination of the other 11 faces.

Note that there is supposed to be a long zero-dimensional barcode that persists to infinity $[0, \infty)$. However, the 'TDAstats' package, which is used in plotting persistent barcodes, omits it [WWDS18].
If each Vietoris-Rips is a wedge sum of spheres, then the homology computations tell us how many wedges in each dimension we will get. The following theorem tells us that this is indeed the case.

Theorem 3.2.1. (joint with Witzel, Titz-Mite)
If $P^{(0)}$ is the vertex set of a platonic solid P and $\delta_1, \ldots, \delta_k$ are the occurring distances between elements of $P^{(0)}$ then the homotopy type of $\mathrm{VR}_r(P^{(0)})$ is given as follows. If $r \leqslant 0$ then $\mathrm{VR}_r(P^{(0)}) = \varnothing$, if $r > \delta_k$ then $\mathrm{VR}_r(P^{(0)}) \simeq *$, otherwise:

1. If P is a tetrahedron then

$$\mathrm{VR}_r(P^{(0)}) \simeq \begin{cases} \bigvee^3 S^0 & 0 < r \leqslant \delta_1 \end{cases}$$

2. If P is an octahedron then

$$\mathrm{VR}_r(P^{(0)}) \simeq \begin{cases} \bigvee^5 S^0 & 0 < r \leqslant \delta_1 \\ S^2 & \delta_1 < r \leqslant \delta_2 \end{cases}$$

3. If P is a cube then

$$\mathrm{VR}_r(P^{(0)}) \simeq \begin{cases} \bigvee^7 S^0 & 0 < r \leqslant \delta_1 \\ \bigvee^5 S^1 & \delta_1 < r \leqslant \delta_2 \\ S^3 & \delta_2 < r \leqslant \delta_3 \end{cases}$$

4. If P is an icosahedron then

$$\mathrm{VR}_r(P^{(0)}) \simeq \begin{cases} \bigvee^{11} S^0 & 0 < r \leqslant \delta_1 \\ S^2 & \delta_1 < r \leqslant \delta_2 \\ S^5 & \delta_2 < r \leqslant \delta_3 \end{cases}$$

5. If P is a dodecahedron then

$$\mathrm{VR}_r(P^{(0)}) \simeq \begin{cases} \bigvee^{19} S^0 & 0 < r \leqslant \delta_1 \\ \bigvee^{11} S^1 & \delta_1 < r \leqslant \delta_2 \\ S^2 & \delta_2 < r \leqslant \delta_3 \\ \bigvee^9 S^3 & \delta_3 < r \leqslant \delta_4 \\ S^9 & \delta_4 < r \leqslant \delta_5 \end{cases}$$

To prove this main theorem, we need the following lemmas and propositions. For simplicity, we write VR_r instead of $\mathrm{VR}_r(P^{(0)})$.

The first lemma interprets the zero-dimensional barcodes.

Lemma 3.2.2. *If $0 < r \leqslant 1$ then $\mathrm{VR}_r(P^{(0)})$ is the discrete set of v vertices, so it is $\bigvee^{v-1} S^0$.* □

The next lemma interprets the highest dimensional barcode.

Lemma 3.2.3. *If $P = -P$ (so if P is not the regular simplex) and if $k-1 < r \leqslant k$ then $\mathrm{VR}_r \cong S^{v/2-1}$.*

Proof. For $x \in P^{(0)}$ the only point at distance k from x is $-x$. So, a face of the full simplex on $P^{(0)}$ is in VR_r unless it has two opposite vertices. Hence, VR_r is the boundary of the $v/2$-dimensional cross-polytope, which, as we have stated previously, has $S^{v/2-1}$ as its boundary sphere. Consequently, VR_r is homeomorphic to $S^{v/2-1}$. □

The following lemma interprets the two-dimensional barcode of the octahedron and the icosahedron.

Lemma 3.2.4. *If $m = 3$, $1 < k$ and $1 < r \leqslant 2$ then $\mathrm{VR}_r = P^{(2)}$, so in particular $\mathrm{VR}_r \cong S^2$.* □

In the case of a cube or a dodecahedron, note that the combinatorial diameter of a facet is 2. This following lemma interprets the one-dimensional barcodes of the cube and the dodecahedron.

Lemma 3.2.5. *If $m > 3$ and $1 < r \leqslant 2$ then $\mathrm{VR}_r = P^{(1)}$, so in particular $\mathrm{VR}_r \cong \bigvee^{f-1} S^1$.* □

Lemma 3.2.6. *If $n = 3$, $m = 5$, and $2 < r \leqslant 3$ then $\mathrm{VR}_r \cong S^2$. In particular, every triangulation of $P^{(2)}$ without added vertices arises a strong deformation retract of VR_r.*

Proof. There are 3- and 4-simplices that are maximal in VR_r. The 3-simplex σ_x consists of a vertex x and its 3 adjacent vertices. Applying an elementary simplicial collapse on σ_x onto $\sigma_x \backslash \{x\}$ represents a deformation retraction of VR_r, where $\sigma_x \backslash \{x\}$ is a subcomplex of simplices, that belong to facets of P.

A 4-simplix in VR_r is σ_F, where F is a facet of the dodecahedron. If S_F is any triangulation of F, then each vertex $v \in F$ is adjacent to any other vertices of F. We impose a matching on the facets of σ_F that are not in the triangulation S_F by pairing a facet τ, where $v \in \tau$, with the facet $\tau \backslash \{v\}$. This matching is acyclic since

if τ is matched with γ then $v \in \gamma$ but $v \notin \tau$. However, if τ and γ are unmatched, then $v \in \tau$, and $v \in \gamma$. Hence, a cycle cannot evolve. Applying Proposition 1.5.2 and Proposition 1.5.1 completes the proof.

□

The last and the most interesting case is when P is the dodecahedron and $3 < r \leqslant 4$. For this case, we need the following:

Lemma 3.2.7. *The complex* VR_r *has* 10 *tetrahedra* $\tau_1, \ldots, \tau_{10}$ *such that any two of its vertices have distance* 3. □

These are well-known: under the action of the rotation group of the dodecahedron they fall into two orbits and the action on each orbit witnesses that the rotation group is A_5.

Notation: to specify the types of the simplices, i.e., the orbits, we draw the edge graph of the dodecahedron with a colored set of vertices, it represents all the simplices we acquire by having an embedding of the set of colored vertices into a full subgraph.

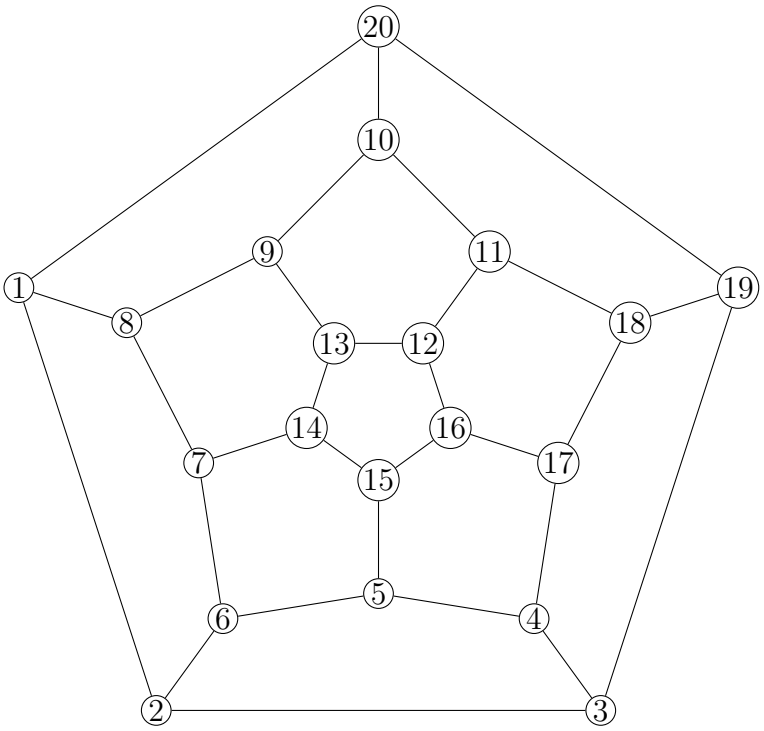

Figure 3.4: The edge graph of the Dodecahedron.

The type of the considered tetrahedra in Lemma 3.2.7 is obtained by coloring the simplex $[5, 8, 12, 19]$ for instance, or the simplex $[6, 13, 17, 20]$, etc.

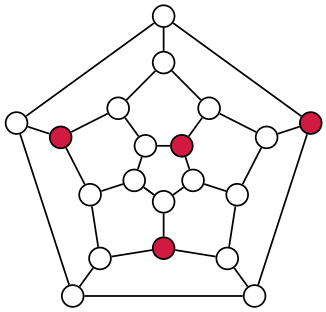

Figure 3.5: One of the 10 tetrahedra, [5, 8, 12, 19].

Tailoring Proposition 1.5.2 on the dodecahedron, we state the following:

Proposition 3.2.8. *There is a strong deformation retraction of* $\mathrm{VR}_{\leqslant 3} \setminus \{\tau_1, \ldots, \tau_{10}\}$ *to* $\mathrm{VR}_{\leqslant 2}$*. More precisely there is a partial acyclic matching on the simplices of* $\mathrm{VR}_{\leqslant 3}$ *of diameter* 3 *whose only critical simplices are* $\tau_1, \ldots, \tau_{10}$*.*

Proof. To prove the proposition we need to induce a partial matching on all the simplices of diameter 3 except for the tetrahedra, $\tau_1, \ldots, \tau_{10}$, and prove that this matching is acyclic. In general, there are 34 unoriented simplices of diameter 3, (excluding $\tau_1, \ldots, \tau_{10}$), and they are 2-, 3-, 4-, 5- and 6-simplices, see [SMW23a] and Appendix B. We impose an orientation on the edges of the dodecahedron. Whenever we plot a graph, it represents the class of a simplex. When we draw an edge orientation, then the simplex drawn in this graph is identified with the dodecahedron graph in a way that the edge orientation of the simplex matches the edge orientation of the dodecahedron graph. This process of picking an orientation on the edge of a simplex and matching it in a one-to-one correspondence always happens when some simplex that has symmetry is matched with a simplex that does not have symmetry. For more explanation, consider the following example:

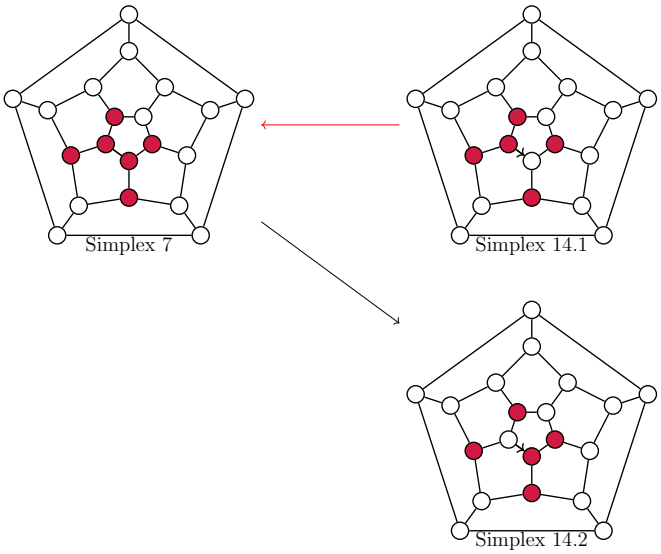

Figure 3.6: An example of a matching.

The two simplices on the right-hand side have a different edge orientation. We choose to match Simplex 14.1 with Simplex 7, and Simplex 14.2 is considered as one of the facets of Simplex 7. Since the matched simplices can be written as pairs, we express this matching by writing (Simplex 14.1, Simplex 7), or by specifying the simplices with their numbered vertices ([5,7,13,14,16], [5,7,13,14,15,16]). The latter notation is used in defining the following matching:
Note that each plot represents two paired simplices, where the first element is the simplex without the green vertex, and the second element is the simplex of all colored vertices (red and green).

- Matching simplices with C_3 and C_2 symmetry:

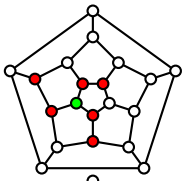

$([5, 7, 8, 12, 13, 15], [5, 7, 8, 12, 13, 14, 15])$

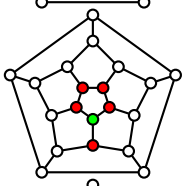

$([5, 12, 13, 14, 16], [5, 12, 13, 14, 15, 16])$

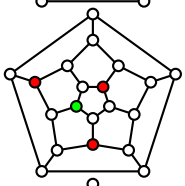

$([5, 8, 12], [5, 8, 12, 14])$

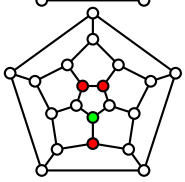

$([5, 12, 13], [5, 12, 13, 15])$

- Matching simplices with broken C_2 symmetry:

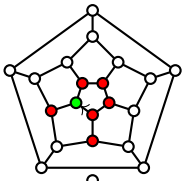

$([5, 7, 12, 13, 15, 16], [5, 7, 12, 13, 14, 15, 16])$

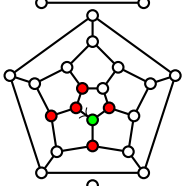

$([5, 7, 13, 14, 16], [5, 7, 13, 14, 15, 16])$

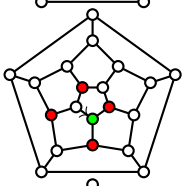

$([5, 7, 13, 16], [5, 7, 13, 15, 16])$

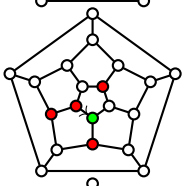

$([5, 7, 12, 14], [5, 7, 12, 14, 15])$

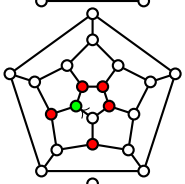

$([5, 7, 12, 13, 16], [5, 7, 12, 13, 14, 16])$

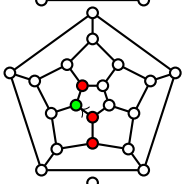

$([5, 13, 15], [5, 13, 14, 15])$

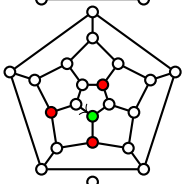

$([5, 7, 12], [5, 7, 12, 15])$

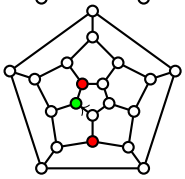

$([5, 13], [5, 13, 14])$

- Matching simplices with trivial stabilizer:

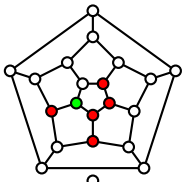

$([5, 7, 12, 15, 16], [5, 7, 12, 14, 15, 16])$

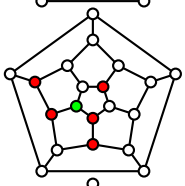

$([5, 7, 8, 12, 15], [5, 7, 8, 12, 14, 15])$

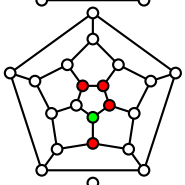

$([5, 12, 13, 16], [5, 12, 13, 15, 16])$

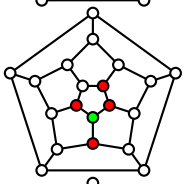

$([5, 12, 14, 16], [5, 12, 14, 15, 16])$

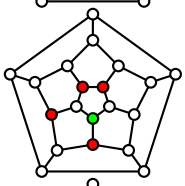

$([5, 7, 12, 13], [5, 7, 12, 13, 15])$

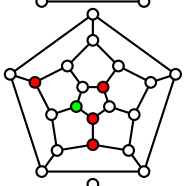

$([5, 8, 12, 15], [5, 8, 12, 14, 15])$

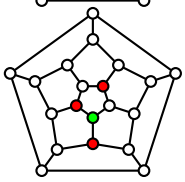

$([5, 12, 14], [5, 12, 14, 15])$

Finally, we are left to prove that the presented matching is indeed acyclic. Therefore, it is sufficient to show that the simplices in adjacent dimensions of the Hasse diagram of our underlying graph can be particularly ordered in such a way that arrows are all pointing in one direction. We will work on adjacent dimensions, starting from the highest, and keeping in mind that the red arrows ($\rightarrow$) will always present the matching, then the black arrows are obviously indicating that there is no matching, they are actually resulting from applying the boundary operator. We will be able to divide each adjacent dimension into different layers.

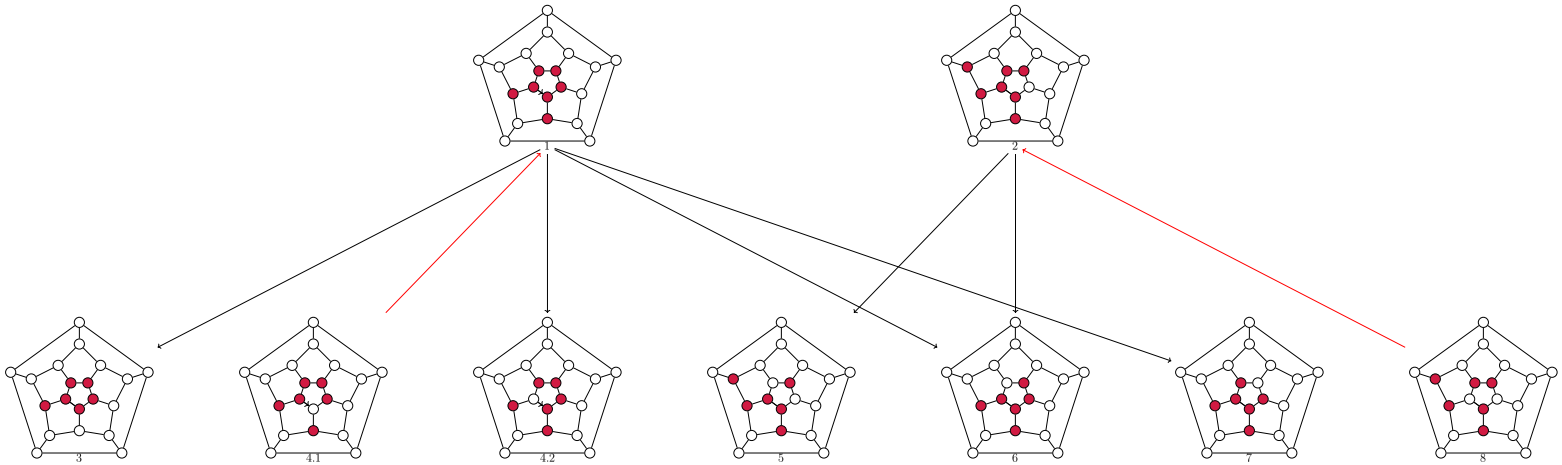

Figure 3.7: The acyclic matching on the first level of the simplicial complex of the dodecahedron, the 5- and 6-simplices.

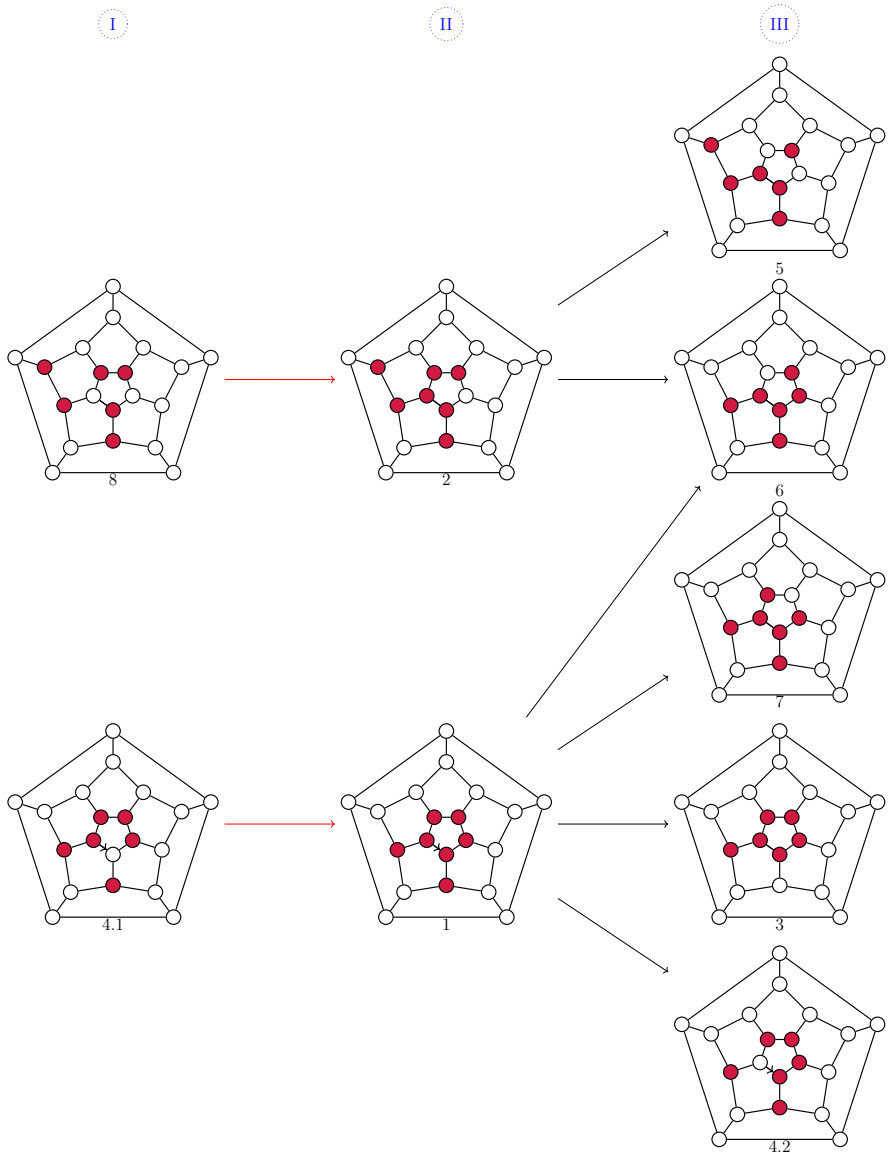

Figure 3.8: The directed graph G_1, for the acyclic matching from Figure 3.7 and its decomposition into three layers I, II, and III.

Figure 3.9: The acyclic matching on the second level of the simplicial complex of the dodecahedron, the 4- and 5-simplices. We avoid drawing the downward edges in this diagram for clarity.

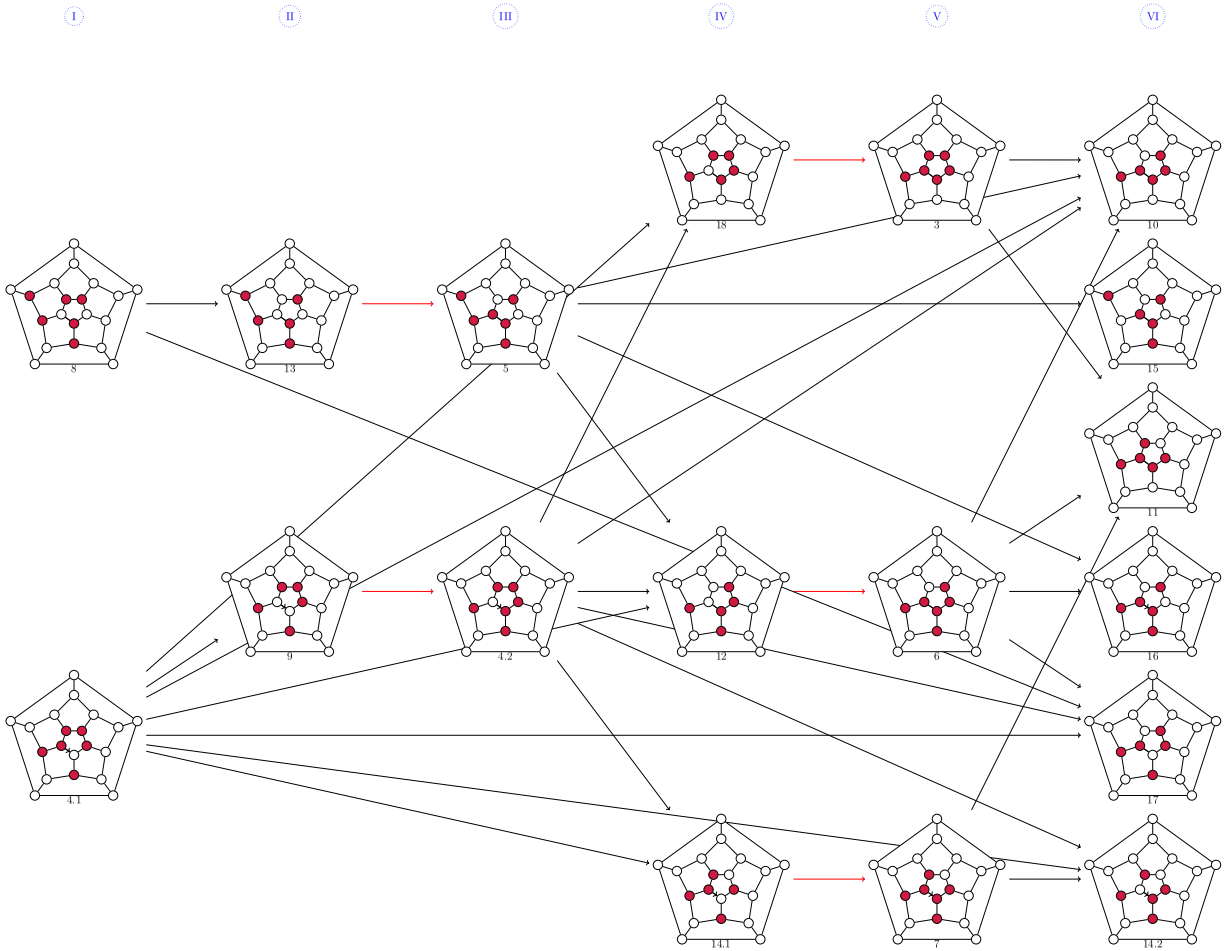

Figure 3.10: The directed graph G_2, for the acyclic matching from Figure 3.9 and its decomposition into six layers I, II, III, IV, V, and VI.

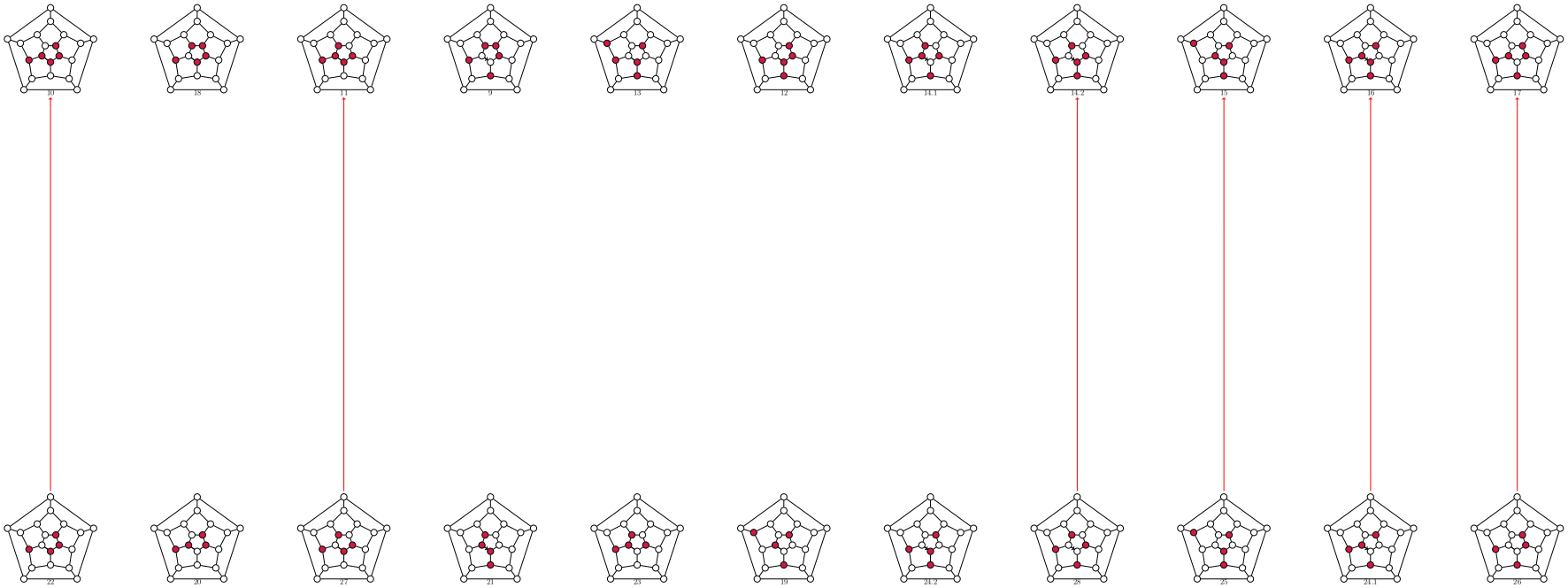

Figure 3.11: The acyclic matching on the third level of the simplicial complex of the dodecahedron, the 3- and 4-simplices. We avoid drawing the downward edges in this diagram for clarity.

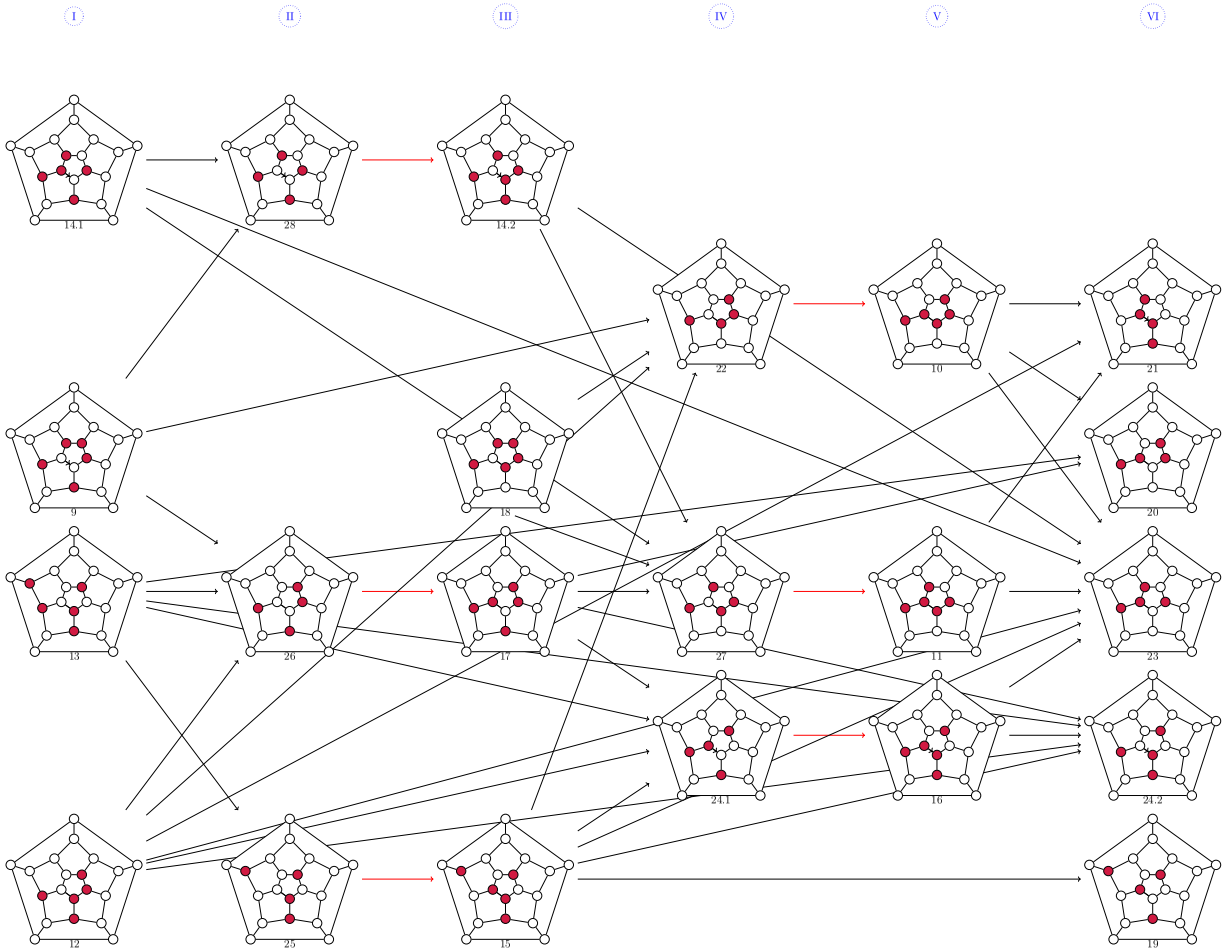

Figure 3.12: The directed graph G_3, for the acyclic matching from Figure 3.11 and its decomposition into six layers I, II, III, IV, V, and VI.

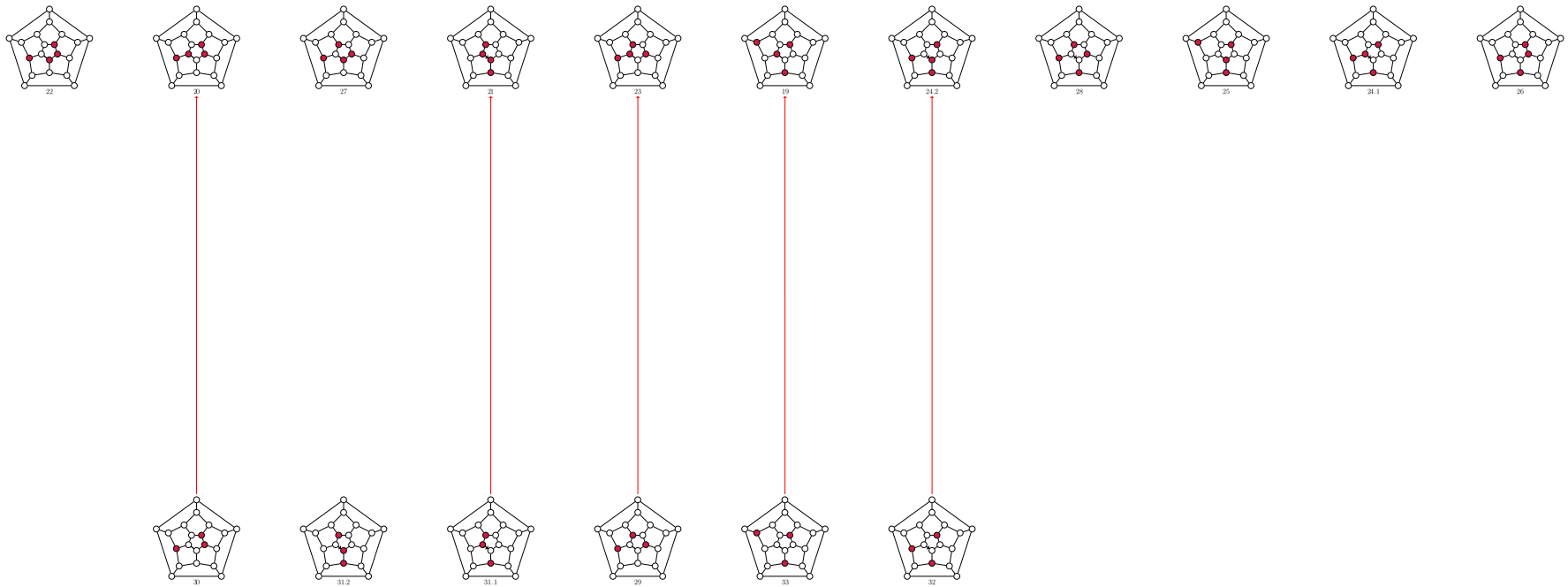

Figure 3.13: The acyclic matching on the fourth level of the simplicial complex of the dodecahedron, the 2- and 3-simplices. We avoid drawing the downward edges in this diagram for clarity.

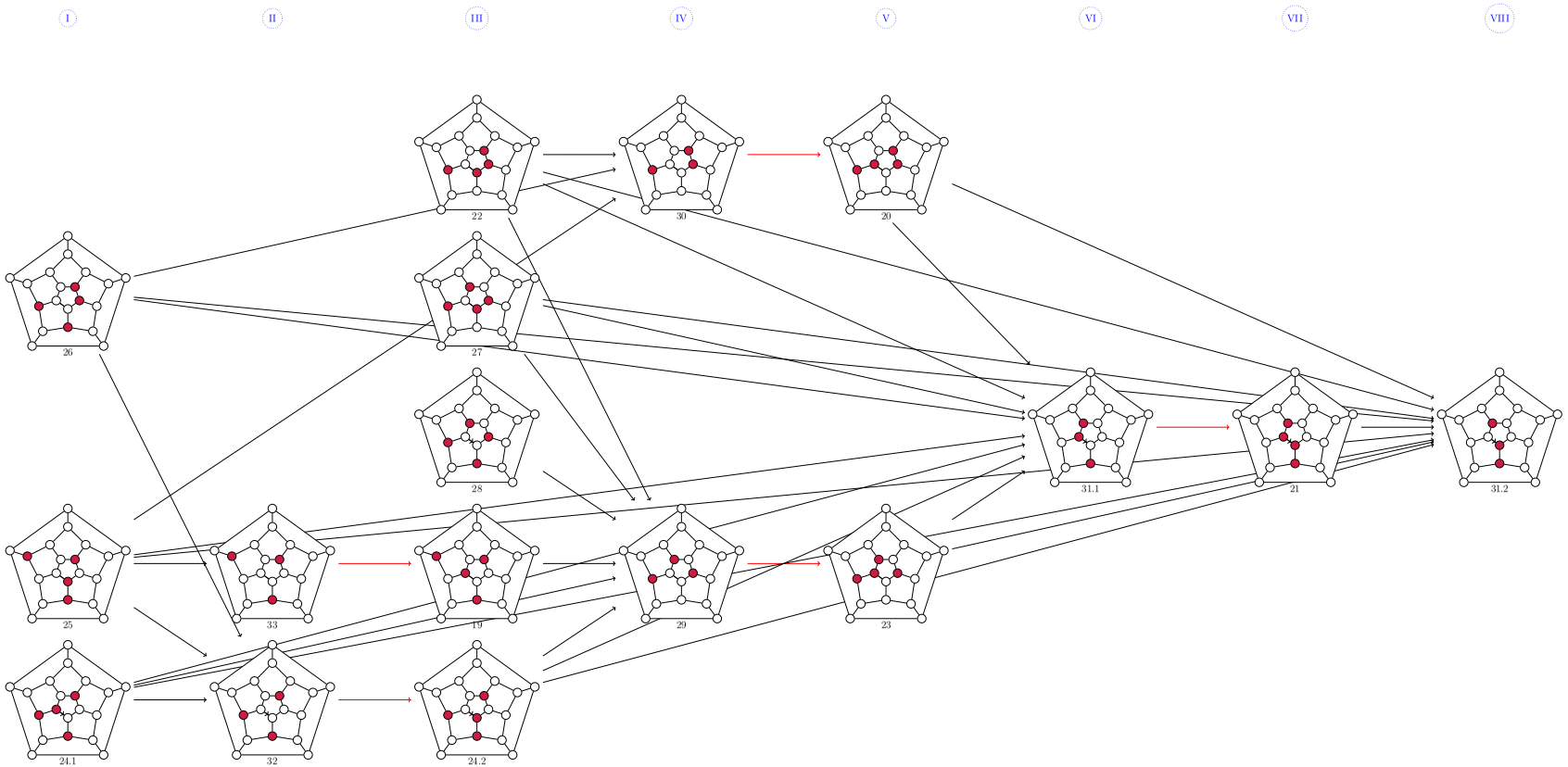

Figure 3.14: The directed graph G_4, for the acyclic matching from Figure 3.13 and its decomposition into six layers I, II, III, IV, V, and VI.

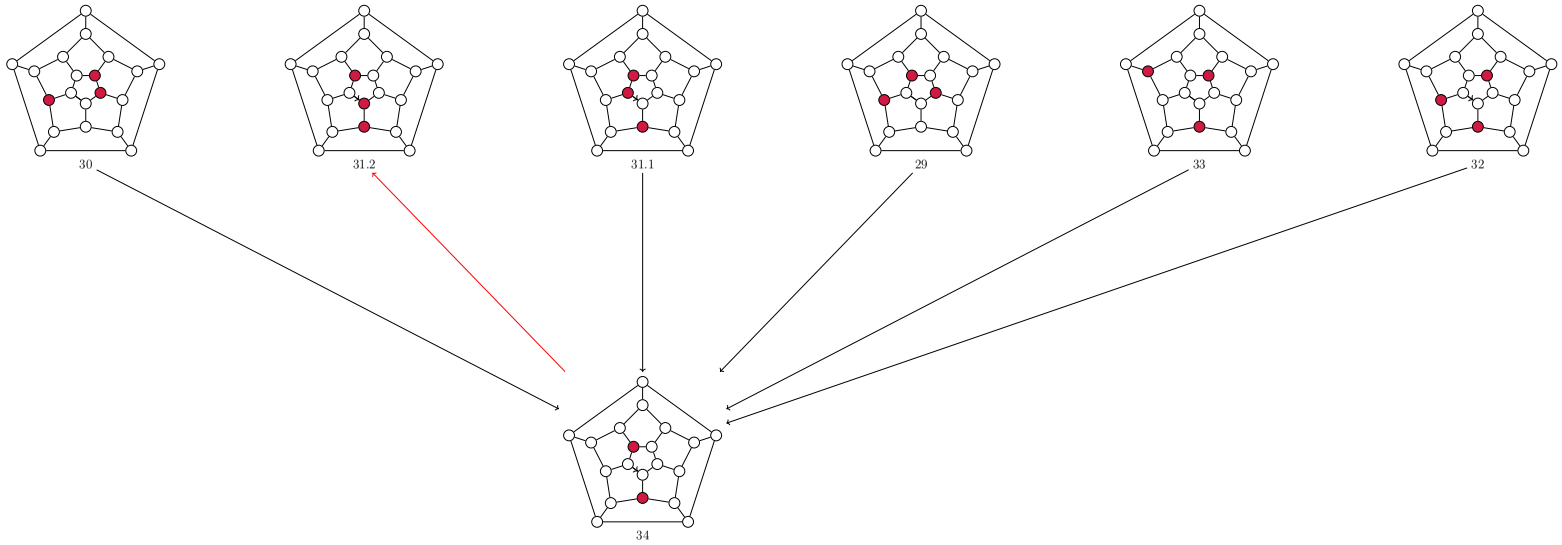

Figure 3.15: The acyclic matching on the fifth level of the simplicial complex of the dodecahedron, the 1- and 2-simplices.

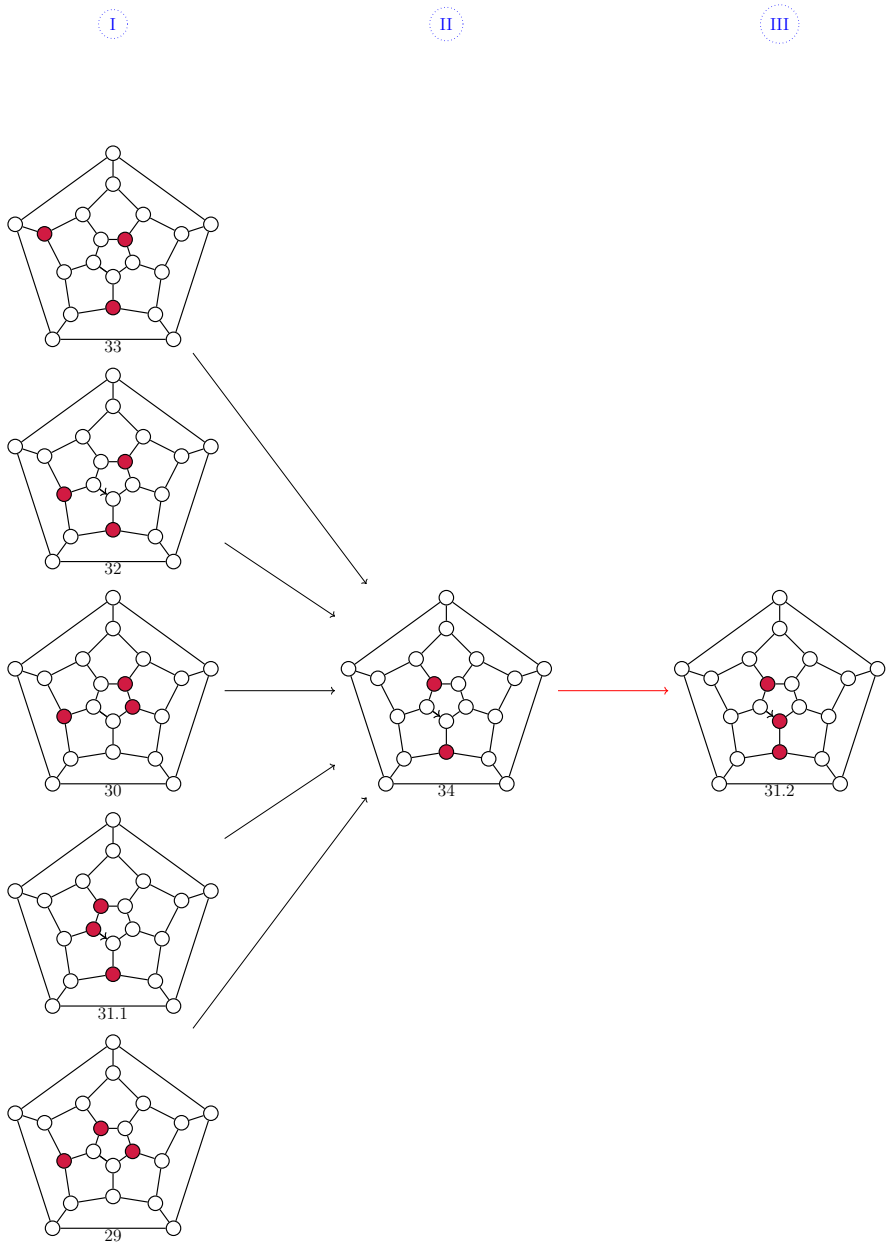

Figure 3.16: The directed graph G_5, for the acyclic matching from Figure 3.15 and its decomposition into three layers I, II, and III.

We excluded the 10 tetrahedra and defined a partial matching on all the left simplices of diameter 3. We proved that this matching is acyclic. Since these 10 tetrahedra were not matched, they are the critical simplices of diameter 3. Hence,

we get a strong deformation retraction of $\mathrm{VR} \leqslant 3 \backslash \{\tau_1, \ldots, \tau_{10}\}$ to $\mathrm{VR}_{\leqslant 2}$, and that completes the proof.

□

To prove Theorem 3.2.1 it remains to show that the map

$$\partial\tau_i \cong S^2 \to S^2 \simeq \mathrm{VR}_{\leqslant 3} \backslash \{\tau_1, \ldots, \tau_{10}\}$$

along which τ_i is glued in is a homotopy equivalence. To study this map, we have to homotope it along the deformation retraction that is described in Proposition 3.2.8. Theorem 1.3.2 states that there is an isomorphism between $\pi_2(X)$ and $H_2(X)$, if the space X is 1-connected. Therefore, it is sufficient to show:

Proposition 3.2.9. *For each i the homology class $[\partial\tau_i]$ generates*

$$H_2(\mathrm{VR}_{\leqslant 3} \backslash \{\tau_1, \ldots, \tau_{10}\}) \cong H_2(\mathrm{VR}_{\leqslant 2}) \cong \mathbb{Z}.$$

Proof. To compute the homology with coefficients of an integral domain, the oriented simplices should be considered. It is worth mentioning that if we permute the numbers of a simplex by an even permutation, we get the same simplex, and if we apply an odd permutation, we get a simplex with an opposite orientation.

Without loss of generality, one of the critical simplices of Proposition 3.2.8, $\{\tau_1, \ldots, \tau_{10}\}$, namely $[6, 13, 17, 20]$, has $[13, 6, 17]$ as one of its facets. We want to figure out how these facets are mapped under the deformation retraction. From the previously defined matching, we know that a 2-simplex, namely $[13, 6, 17]$ is matched with $[6, 13, 17, 15]$. Consequently, to identify the image of $[13, 6, 17]$ under the deformation retraction we compute the boundary of the 3-simplex, $[6, 13, 17, 15]$,

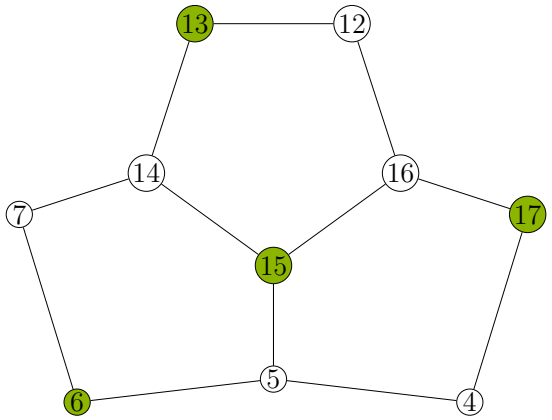

Thus,

$$\partial[13,6,17,15] = [13,6,17] - [13,6,15] + [13,17,15] - [6,17,15]$$

$$[13,6,17] \simeq [13,6,15] + [13,15,17] + [6,17,15] \qquad (*)$$

Each simplex on the right-hand side has the edge lengths 2,2,3. We will try to write each of them as a linear combination of simplices of a maximum edge length 2.

For the simplex [13,6,15]:

$$\partial[13,6,15,14] = [13,6,15] - [6,14,13] + [13,15,14] - [6,15,14]$$

$$[13,6,15] \simeq [6,14,13] + [14,15,13] + [6,15,14]$$

For the simplex [13,15,17]:

$$\partial[13,15,17,16] = [13,15,17] - [13,15,16] + [13,17,16] - [15,17,16]$$

$$[13,15,17] \simeq [16,13,15] + [16,17,13] + [15,17,16]$$

For the simplex [6,17,15]:

$$\partial[6,17,15,5] = [6,17,15] - [6,17,5] + [6,15,5] - [17,15,5]$$

$$[6,17,15] \simeq [6,17,5] + [6,5,15] + [17,15,5]$$

Substituting in (*) we get,

$$\begin{aligned}[13,6,17] \simeq\ & [6,14,13] + [14,15,13] + [6,15,14] \\ & + [16,13,15] + [16,17,13] + [15,17,16] \\ & + [6,17,5] + [6,15,5] + [17,15,5]\end{aligned}$$

Ordering the terms:

$$\begin{aligned}[13,6,17] \simeq\ & [6,15,14] + [15,17,16] + [6,5,15] \\ & + [14,15,13] + [16,13,15] + [17,15,5] \\ & + [6,14,13] + [16,17,13] + [6,17,5]\end{aligned}$$

The summands of the first two rows are in $\mathrm{VR}_{\leqslant 2}$.

Which can be illustrated as:

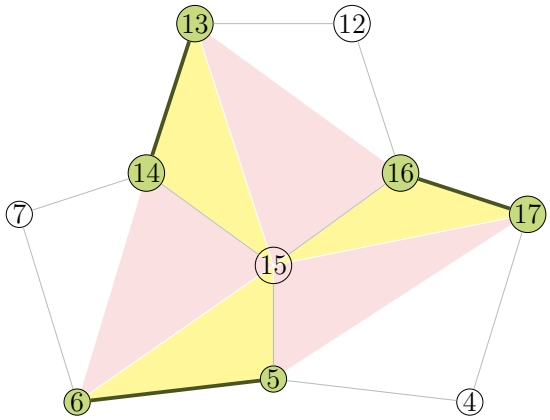

We get similar outcomes for the simplex [17,20,13],

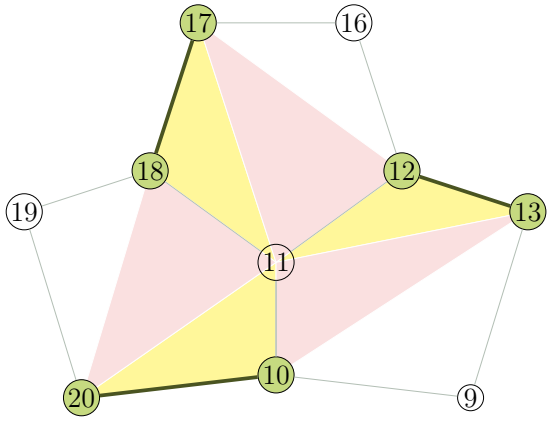

As well as the simplex [13,20,6],

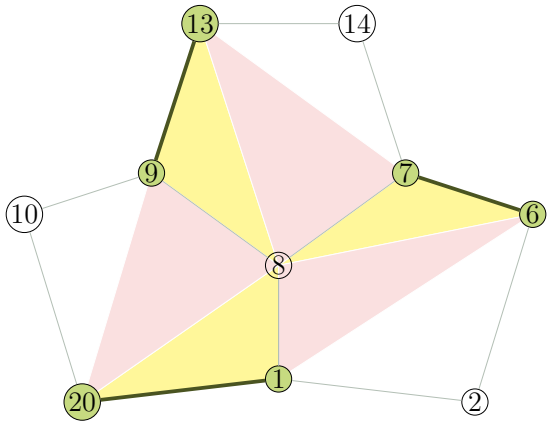

Finally the simplex [17,6,20],

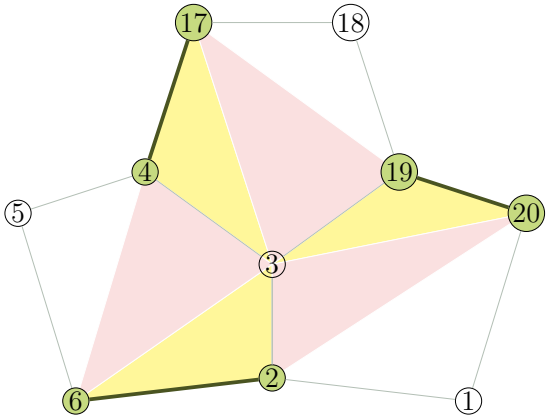

The full boundary of each of the four simplices spans the fundamental class of triangulation of the dodecahedron.

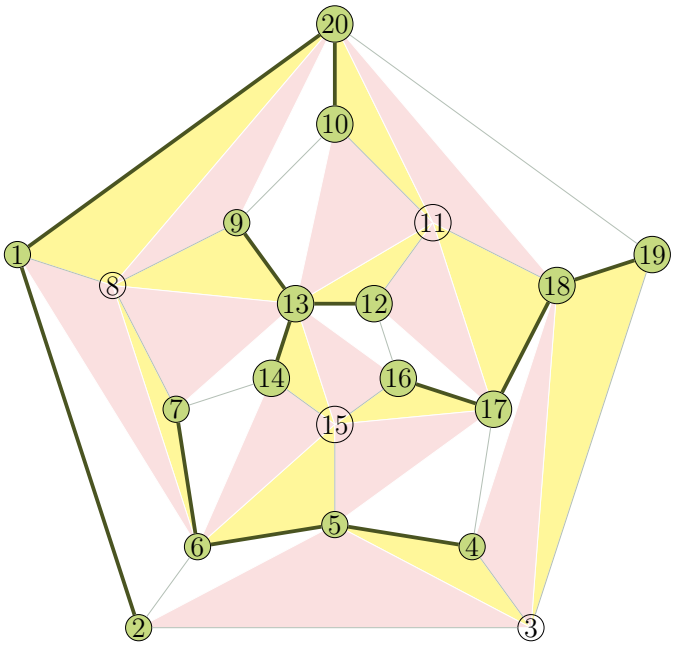

Figure 3.17: Triangulation of the dodecahedron, a tessellation of the 2-Sphere.

When the simplex $[13, 14, 7, 6]$ has the orientation $14 \to 7$, we get:

$$\partial[13, 14, 7, 6] = [13, 14, 7] - [14, 7, 6] + [13, 7, 6] - [13, 14, 6] \qquad (**)$$

The simplex [13,7,6] is matched with a facet, so it does not contribute to the second homology.

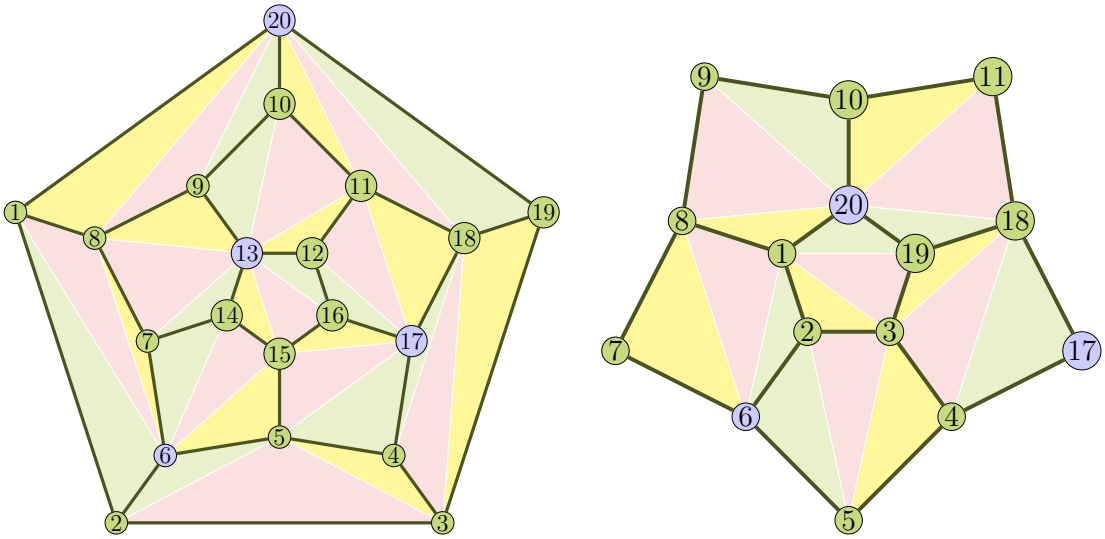

Figure 3.18: Triangulation of the dodecahedron, a tessellation of the 2-Sphere.

From (**) we get,

$$[13, 14, 6] + [14, 7, 6] = [13, 14, 7] + [14, 7, 6]$$

Note that each critical simplex has four facets of type $[6, 13, 7]$. Although we do not know if a simplex of type $[6, 13, 7]$ retracts to simplices of type [13,14,7] or [14,7,6] and has [13,14,7] in its retraction image or not, the sum of the four facets will have [13,14,7] + [14,7,6] in its retraction image, consequently, [13,14,6] + [14,7,6]. Hence, the boundary of a critical simplex τ_i retracts to the sum of the four facets, which gives a complete tessellation for the 2-sphere.

□

In this chapter, we have introduced the concept of cross-polytopes and stated that an n-dimensional cross-polytope has the sphere S^{n-1} as its boundary sphere. We computed the homology of Platonic solids and interpreted them, with a focus on the dodecahedron case. In the dodecahedron, we proved the existence of a strong deformation retraction from $\mathrm{VR}_{\leqslant 3} \setminus \{\tau_1, \ldots, \tau_{10}\}$ onto $\mathrm{VR}_{\leqslant 2}$, to do so, we identified a partial matching on $\mathrm{VR}_{\leqslant 3} \setminus \{\tau_1, \ldots, \tau_{10}\}$ and proved its acyclicity. We later proved that for each i, the homology class $[\partial\tau_i]$, generates

$$H_2(\mathrm{VR}_{\leqslant 3} \setminus \{\tau_1, \ldots, \tau_{10}\}) \cong H_2(\mathrm{VR}_{\leqslant 2}) \cong \mathbb{Z}.$$

Chapter 4

Homology of some n-polytopes

In this chapter, we provide computational outcomes for some hypercubes and 4-Polytopes. The following tables summarize the non-zero homology and the blank lines in the third column indicate that we were able to compute the homology up to a certain dimension but not higher due to the extensive memory consumption.

4.1 The Hypercubes

We compute the homology of some hypercubes. For the identified homotopy types, see [AA22].

n-Cube	Vertices	Homology
2-Cube	4	$H_0(VR_0(Q_2);\mathbb{Z}) = (\mathbb{Z})^3$ $H_1(VR_1(Q_2);\mathbb{Z}) = \mathbb{Z}$
3-Cube	8	$H_0(VR_0(Q_3);\mathbb{Z}) = (\mathbb{Z})^7$ $H_1(VR_1(Q_3);\mathbb{Z}) = (\mathbb{Z})^5$ $H_3(VR_2(Q_3);\mathbb{Z}) = \mathbb{Z}$
4-Cube	16	$H_0(VR_0(Q_4);\mathbb{Z}) = (\mathbb{Z})^{15}$ $H_1(VR_1(Q_4);\mathbb{Z}) = (\mathbb{Z})^{17}$ $H_3(VR_2(Q_4);\mathbb{Z}) = (\mathbb{Z})^9$ $H_7(VR_4(Q_4);\mathbb{Z}) = \mathbb{Z}$
5-Cube	32	$H_0(VR_0(Q_5);\mathbb{Z}) = (\mathbb{Z})^{31}$ $H_1(VR_1(Q_5);\mathbb{Z}) = (\mathbb{Z})^{49}$ $H_3(VR_2(Q_5);\mathbb{Z}) = (\mathbb{Z})^{49}$ $H_4(VR_3(Q_5);\mathbb{Z}) = \mathbb{Z}$ $H_7(VR_3(Q_5);\mathbb{Z}) = (\mathbb{Z})^{10}$ $H_{15}(VR_4(Q_5);\mathbb{Z}) = \mathbb{Z}$

6-Cube	64	$H_0(VR_0(Q_6);\mathbb{Z}) = (\mathbb{Z})^{63}$ $H_1(VR_2(Q_6);\mathbb{Z}) = (\mathbb{Z})^{129}$ $H_3(VR_3(Q_6);\mathbb{Z}) = (\mathbb{Z})^{209}$ $H_4(VR_4(Q_6);\mathbb{Z}) = (\mathbb{Z})^{11}$ $H_7(VR_3(Q_6);\mathbb{Z}) = (\mathbb{Z})^{60}$ $H_7(VR_4(Q_6);\mathbb{Z}) = (\mathbb{Z})^{239}$ $H_{31}(VR_5(Q_6);\mathbb{Z}) = \mathbb{Z}$
7-Cube	128	$H_0(VR_0(Q_7);\mathbb{Z}) = (\mathbb{Z})^{127}$ $H_1(VR_1(Q_7);\mathbb{Z}) = (\mathbb{Z})^{321}$ $H_2(VR_3(Q_7);\mathbb{Z}) = (\mathbb{Z})^{769}$ $H_4(VR_3(Q_7);\mathbb{Z}) = (\mathbb{Z})^{71}$ $H_{63}(VR_6(Q_7);\mathbb{Z}) = \mathbb{Z}$

Computations of the 6-Cube were doable on HPC only up to dimension 7, and the cross-polytope property tells us that S^{31} should appear in the last range. Hence $H_i(VR_k(Q_6);\mathbb{Z})$ is unknown for $8 \leqslant i \leqslant 30$. Similarly, only the first 4 dimensions of the homology computations of the 7-Cube were doable on HPC. Hence, $H_i(VR_k(Q_7);\mathbb{Z})$ is also unknown for $5 \leqslant i \leqslant 62$.

4.1.1 The Tesseract

The 4-Cube, known as the tesseract, has 24 faces and 8 cubes (cells). Its barcodes are illustrated in the following figure:

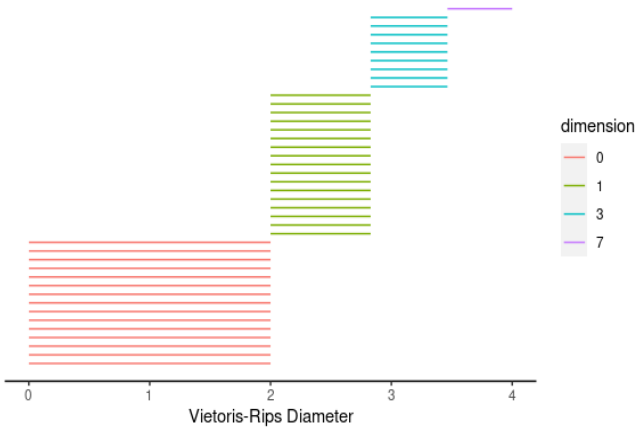

Figure 4.1: Barcodes of the tesseract.

To interpret the 9 wedges of S^3; we start first from the 3-Cube case:
There are three kinds of tetrahedra of diameter 2 in the 3-Cube:

- a vertex and its neighbors (there are 8 ones in the 3-Cube),
- the faces (there are 6 ones in the 3-Cube), and
- vertices of a pairwise-distance 2 (they are 2 ones in the 3-Cube)

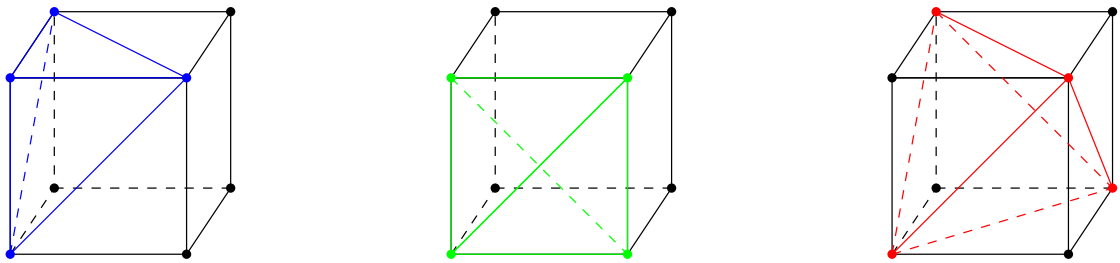

Figure 4.2: The first, second, and third kind of a tetrahedron in a cube.

Analogously to the dodecahedron case in Chapter 3, if we remove the two tetrahedra of the third kind, the remaining complex deformation retracts onto the boundary of the cube which is a 2-sphere. The tetrahedra of the first kind can be matched away from their center, and the tetrahedra of the second kind can be matched to either triangulation of the face. Hence, the complex is a 2-sphere with two 3-simplices glued in. The first 3-simplex fills the 2-sphere, the second tetrahedron creates a 3-sphere.

Regarding the 4-Cube; the 2-Skeleton consists of the boundary of its eight 3-Cubes. Therefore, it is a wedge of seven 2-Spheres. Into these seven 2-Spheres if we glue the 3-Simplices of the third kind, there are $16 = 8 \times 2$, of them in the 4-Cube. The first of these fill in 2-Spheres while the remaining create 3-Spheres. Hence, we get $16 - 7 = 9$ wedges of 3-Spheres.

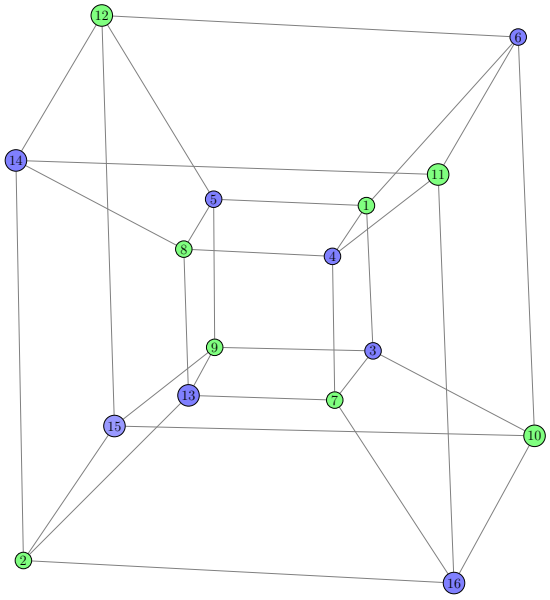

Figure 4.3: The tesseract.

4.2 4-Polytopes

Another interesting family to investigate its homology is the 4-Polytopes, the four-dimensional analogs of the Platonic solids. In the following table, we provide the computational outcome.

4-Polytope	Vertices	Diameter	Homology
24-Cell	24	4	$H_2(VR_1(C_{24});\mathbb{Z}) = (\mathbb{Z})^{23}$ $H_3(VR_2(C_{24});\mathbb{Z}) = \mathbb{Z}$ $H_{11}(VR_3(C_{24});\mathbb{Z}) = \mathbb{Z}$
600-Cell	120	8	$H_3(VR_1(C_{600});\mathbb{Z}) = \mathbb{Z}$ $H_{59}(VR_7(C_{600});\mathbb{Z}) = \mathbb{Z}$
120-Cell	600	15	$H_1(VR_1(C_{120});\mathbb{Z}) = (\mathbb{Z})^{601}$ $H_2(VR_2(C_{120});\mathbb{Z}) = (\mathbb{Z})^{119}$ $H_3(VR_3(C_{120});\mathbb{Z}) = (\mathbb{Z})^{1080}$ $H_3(VR_3(C_{120});\mathbb{Z}) = \mathbb{Z}$ $H_{299}(VR_{15}(C_{120});\mathbb{Z}) = \mathbb{Z}$

For the 600-cell, only homology up to dimension 4 was computable. Hence, $H_i(VR_k(C_{600});\mathbb{Z})$ is unknown, where $5 \leqslant i \leqslant 58$ and $42 \leqslant k \leqslant 6$. As well for the 120-cell, only homology up to dimension 3 was obtainable. $H_i(VR_k(C_{120});\mathbb{Z})$ is unknown, where $4 \leqslant i \leqslant 298$ and $4 \leqslant k \leqslant 14$.

The 23 copies of the second-dimensional barcodes of the e24-cell represent the 24 octahedra that the 24-cell consists of. The existence of the third-dimensional barcode is because it is a 4-polytope, similar to the existence of the first-dimensional barcode in the circle and the second-dimensional barcode in the 2-sphere. The eleventh-dimensional barcode is coming from the cross-polytope property.

Similarly for the 120-cell, the 119 copies of barcodes in dimension 2 are a result of the fact that the 120-cell consists of 120 dodecahedrons and each one of them produces one barcode, the last missed copy can be written as a linear combination of the 119 copies.

Further computations and interpretations are indeed needed for the two interesting types: hypercubes and 4-polytopes.

Open questions and further research

Chapter 2

- For the 2-Sphere, prove computationally that $H_3(VR_r(X)) \simeq 0$, when r exceeds the diameter of a 3-simplex (see Section 2.2.3).
- Prove Conjecture 2.2.1 (see Table 3.3).

Chapter 3

- Prove conjecture 5.7 of [AlAC$^+$] (see Theorem 5.4 and Remark 5.5, 5.6 in the same reference).
- Determine the homology and then characterize the homotopy types of $\mathrm{VR}_r(S^2)$ and $\check{C}_r(S^2)$ for larger values of r (check the interleaving property of the two complexes and Theorem 1.3.2).
- Try to do the same for Vietoris-Rips complexes of higher dimensional spheres of a larger scale r.
- Investigate the homotopy types of $\mathrm{VR}_r(T^n)$ and $\check{C}_r(T^n)$ when r gets larger, and where $T^n = (S^1)^n$ is an $n-$dimensional Torus.

Chapter 4

- Complete the homology computations of the hypercubes and 4-Polytopes tables (see Section 4.1 and 4.2).
- Determine the homotopy types of the hypercubes and the 4-Polytopes.
- Specify the homotopy types of Catalan solids.
- Specify the homotopy types of Archemidean solids.

Bibliography

[AA17] Michał Adamaszek and Henry Adams. The vietoris–rips complexes of a circle. *Pacific Journal of Mathematics*, 290(1):1–40, 2017.

[AA22] Michał Adamaszek and Henry Adams. On vietoris–rips complexes of hypercube graphs. *Journal of Applied and Computational Topology*, 6(2):177–192, 2022.

[AAF18] Michał Adamaszek, Henry Adams, and Florian Frick. Metric reconstruction via optimal transport. *SIAM Journal on Applied Algebra and Geometry*, 2(4):597–619, 2018.

[AAM17] Michał Adamaszek, Henry Adams, and Francis Motta. Random cyclic dynamical systems. *Advances in Applied Mathematics*, 83:1–23, 2017.

[AAR19] Michał Adamaszek, Henry Adams, and Samadwara Reddy. On vietoris–rips complexes of ellipses. *Journal of Topology and Analysis*, 11(03):661–690, 2019.

[AB04] D Anderson and K Burnham. Model selection and multi-model inference. *Second. NY: Springer-Verlag*, 63(2020):10, 2004.

[ACJS18] Henry Adams, Samir Chowdhury, Adam Quinn Jaffe, and Bonginkosi Sibanda. Vietoris-rips complexes of regular polygons. *arXiv preprint arXiv:1807.10971*, 2018.

[AlAC+] Henry Adams, Micha l Adamaszek, Mark Heim Carr, Lara Kassab, Joshua Mirth, and Alex Williams. Metric reconstruction via optimal transport.

[AT+11] Henry Adams, Andrew Tausz, et al. Javaplex tutorial. *Google Scholar*, 27, 2011.

[ATVJ14] Henry Adams, Andrew Tausz, and Mikael Vejdemo-Johansson. Javaplex: A research software package for persistent (co) homology. In *Mathematical Software–ICMS 2014: 4th International Congress, Seoul, South Korea, August 5-9, 2014. Proceedings 4*, pages 129–136. Springer, 2014.

[Bau21] Ulrich Bauer. Ripser: efficient computation of Vietoris-Rips persistence barcodes. *J. Appl. Comput. Topol.*, 5(3):391–423, 2021.

[Cho17] Aruni Choudhary. Approximation algorithms for vietoris-rips and čech filtrations. 2017.

[CJS15] Nicholas J Cavanna, Mahmoodreza Jahanseir, and Donald R Sheehy. A geometric perspective on sparse filtrations. *arXiv preprint arXiv:1506.03797*, 2015.

[CMC+16] Lorin Crawford, Anthea Monod, Andrew X Chen, Sayan Mukherjee, and Raúl Rabadán. Topological summaries of tumor images improve prediction of disease free survival in glioblastoma multiforme. *arXiv preprint arXiv:1611.06818*, 2, 2016.

[Cox73] Harold Scott Macdonald Coxeter. *Regular polytopes*. Courier Corporation, 1973.

[DMD15] Marie Laure Delignette-Muller and Christophe Dutang. fitdistrplus: An r package for fitting distributions. *Journal of statistical software*, 64:1–34, 2015.

[DMDP+15] Marie Laure Delignette-Muller, Christophe Dutang, Regis Pouillot, Jean-Baptiste Denis, and Maintainer Marie Laure Delignette-Muller. Package 'fitdistrplus'. *Journal of Statistical Software*, 64(4):1–34, 2015.

[DW22] Tamal Krishna Dey and Yusu Wang. *Computational topology for data analysis*. Cambridge University Press, 2022.

[EH22] Herbert Edelsbrunner and John L Harer. *Computational topology: an introduction*. American Mathematical Society, 2022.

[For02] Robin Forman. A user's guide to discrete morse theory. *Séminaire Lotharingien de Combinatoire [electronic only]*, 48:B48c–35, 2002.

[GFW17] William Gasarch, Brittany Terese Fasy, and Bei Wang. Open problems in computational topology. *ACM SIGACT News*, 48(3):32–36, 2017.

[H+95] Jean-Claude Hausmann et al. On the vietoris-rips complexes and a cohomology theory for metric spaces. *Annals of Mathematics Studies*, 138:175–188, 1995.

[Hat02] Allen Hatcher. *Algebraic topology*. Cambridge University Press, Cambridge, 2002.

[HDP22] Greg Hamilton, Travis Dore, and Christopher Plumberg. Applications of persistent homology in nuclear collisions. *arXiv preprint arXiv:2209.15480*, 2022.

[KMM04] Tomasz Kaczynski, Konstantin Michael Mischaikow, and Marian Mrozek. *Computational homology*, volume 3. Springer, 2004.

[KNBNH16] Violeta Kovacev-Nikolic, Peter Bubenik, Dragan Nikolić, and Giseon Heo. Using persistent homology and dynamical distances to analyze protein binding. *Statistical applications in genetics and molecular biology*, 15(1):19–38, 2016.

[Koz08] Dimitry Kozlov. *Combinatorial algebraic topology*, volume 21. Springer Science & Business Media, 2008.

[Koz21] Dmitry N Kozlov. *Organized collapse: An introduction to discrete Morse theory*, volume 207. American mathematical society, 2021.

[Lat01] Janko Latschev. Vietoris-rips complexes of metric spaces near a closed riemannian manifold. *Archiv der Mathematik*, 77(6):522–528, 2001.

[LMO20] Sunhyuk Lim, Facundo Memoli, and Osman Berat Okutan. Vietoris-rips persistent homology, injective metric spaces, and the filling radius. *arXiv preprint arXiv:2001.07588*, 2020.

[SL03] George AF Seber and Alan J Lee. *Linear regression analysis*, volume 330. John Wiley & Sons, 2003.

[SMW23a] Nada Saleh, Thomas Titz Mite, and Stefan Witzel. switzel/regular_polytope_vr. September 2023. `https://doi.org/10.5281/zenodo.7670647`.

[SMW23b] Nada Saleh, Thomas Titz Mite, and Stefan Witzel. Vietoris-rips complexes of platonic solids. *arXiv preprint arXiv:2302.14388*, 2023.

[TSBO18] Christopher Tralie, Nathaniel Saul, and Rann Bar-On. Ripser.py: A lean persistent homology library for python. *The Journal of Open Source Software*, 3(29):925, Sep 2018.

[VAB13] Ramanarayan Vasudevan, Aaron Ames, and Ruzena Bajcsy. Persistent homology for automatic determination of human-data based cost of bipedal walking. *Nonlinear Analysis: Hybrid Systems*, 7(1):101–115, 2013.

[WWDS18] Raoul R Wadhwa, Drew FK Williamson, Andrew Dhawan, and Jacob G Scott. Tdastats: R pipeline for computing persistent homology in topological data analysis. *Journal of open source software*, 3(28):860, 2018.

[Zom05] Afra J Zomorodian. *Topology for computing*, volume 16. Cambridge university press, 2005.

[Zom09] Afra Zomorodian. Computational topology. *Algorithms and theory of computation handbook*, 2(3), 2009.

Appendix A

Barcodes

The following plots represent barcodes of the rhombic triacontahedron and different Thomson solids. These outcomes were summarised in Section 2.2.2.

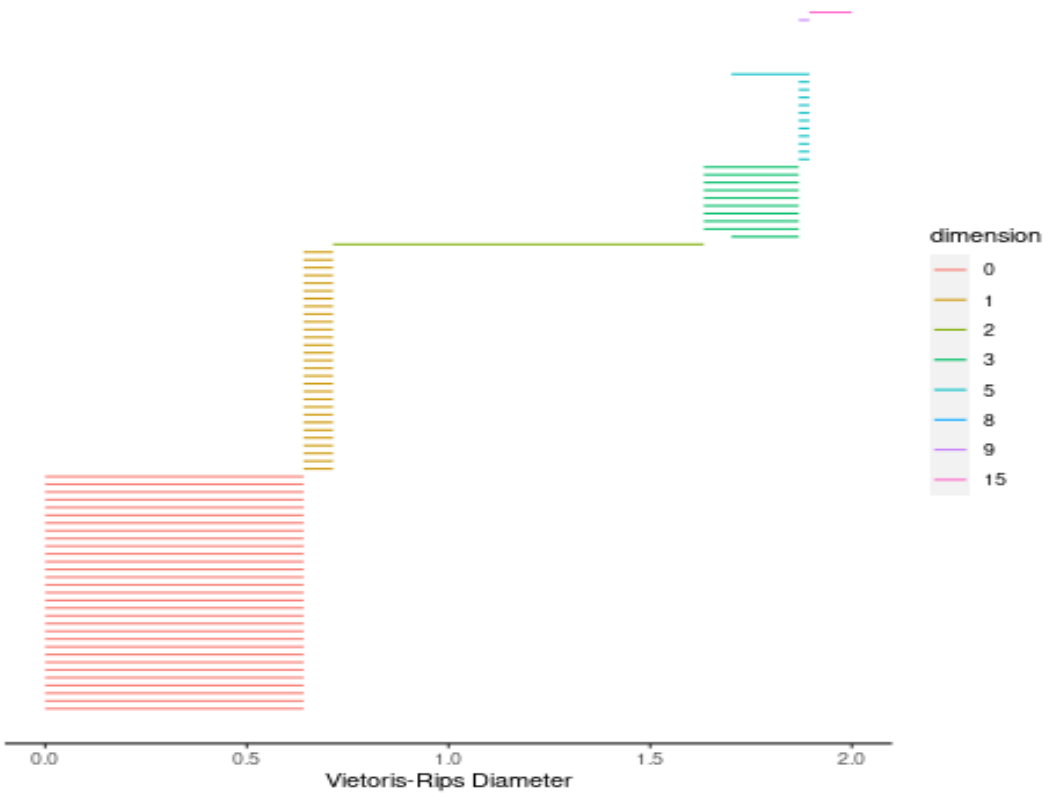

Figure A.1: Barcodes of Rhombic triacontahedron.

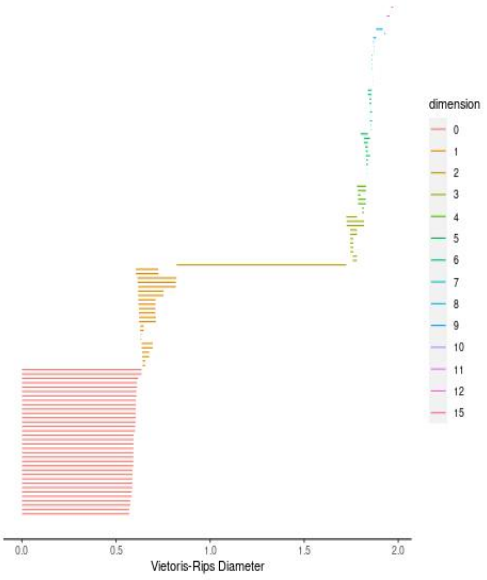

(a) Thomson 35

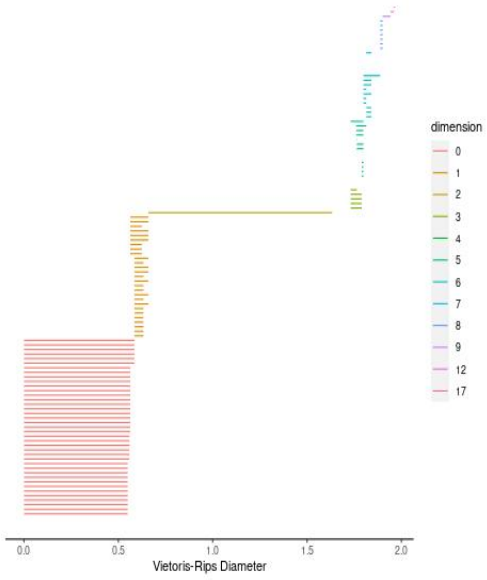

(b) Thomson 40

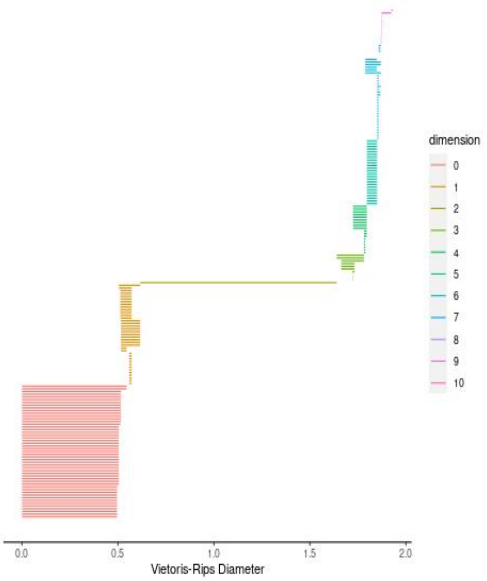

(c) Thomson 50

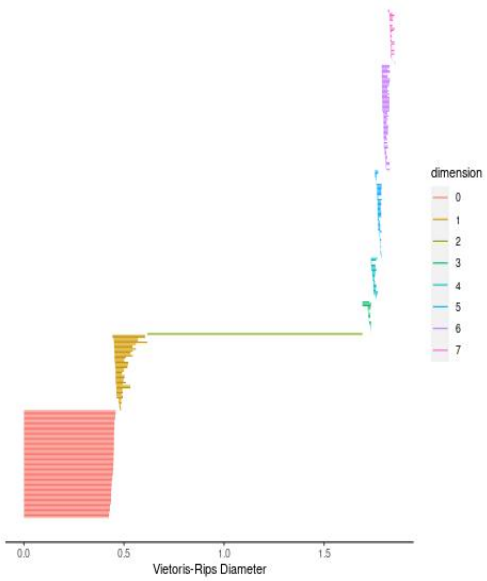

(d) Thomson 65

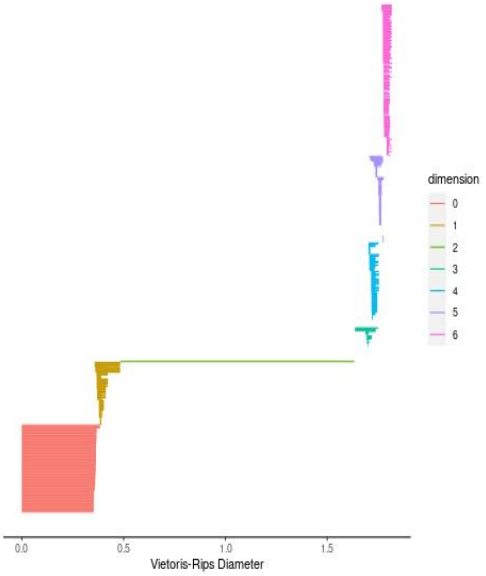

(a) Thomson 100

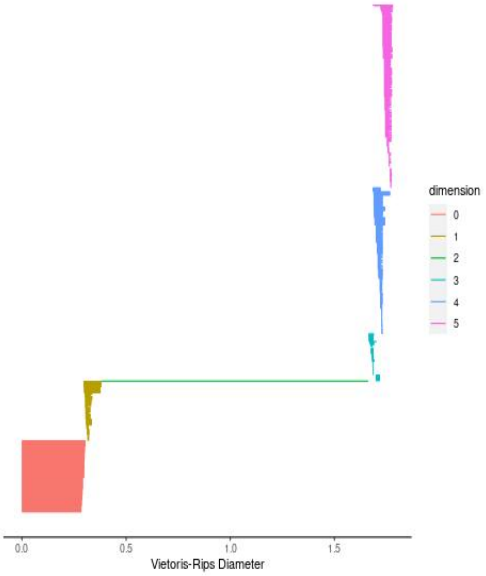

(b) Thomson 150

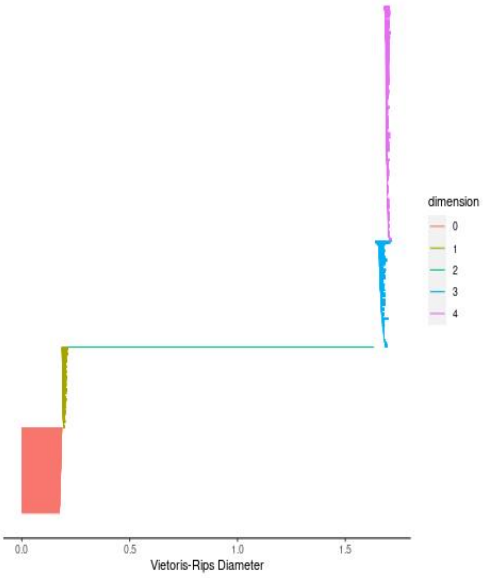

(c) Thomson 400

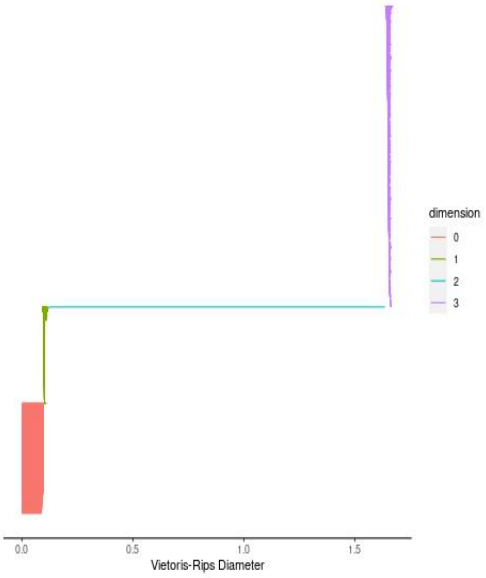

(d) Thomson 1500

Appendix B

Simplices and their facets

These facets were determined thanks to the gap code written by Thomas Titz-Mite. See [SMW23a].

6-Simplices and their facets

Simplex 1

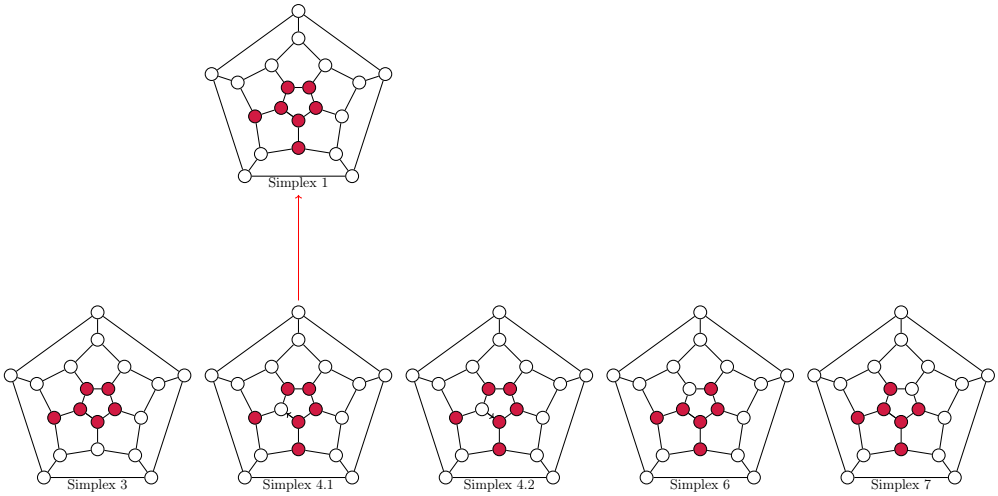

Figure B.1: Simplex 1 and its facets. Simplex 1 is matched with Simplex 4.1.

Simplex 2

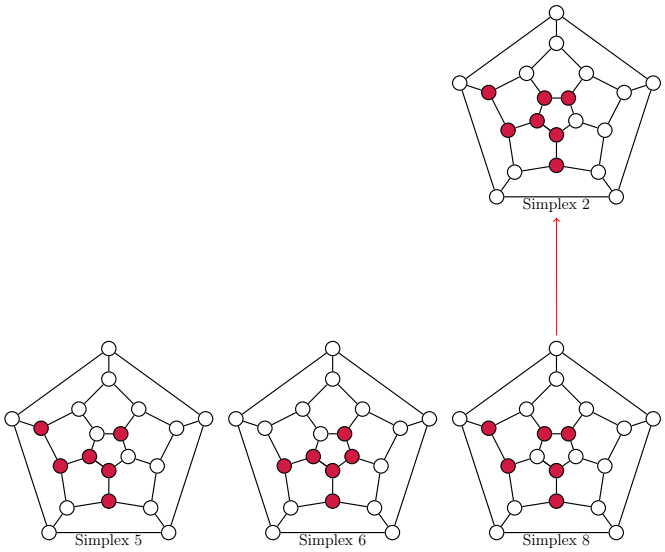

Figure B.2: Simplex 2 and its facets. Simplex 2 is matched with Simplex 8.

5-Simplices and their facets

Simplex 3

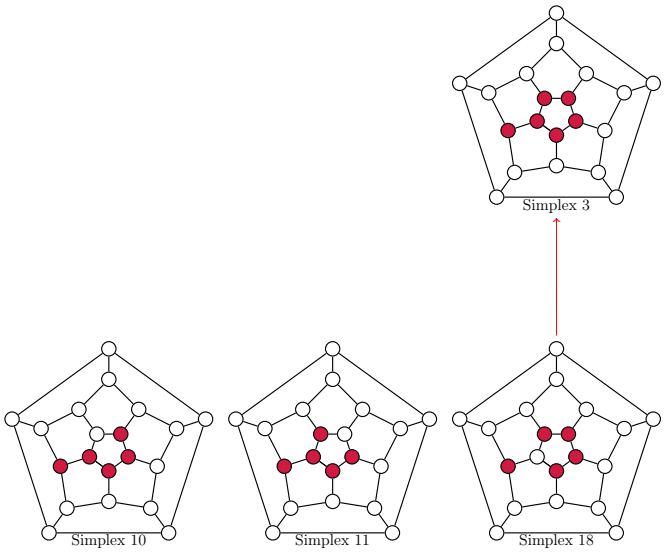

Figure B.3: Simplex 3 and its facets. Simplex 3 is matched with Simplex 18.

Simplex 4.1

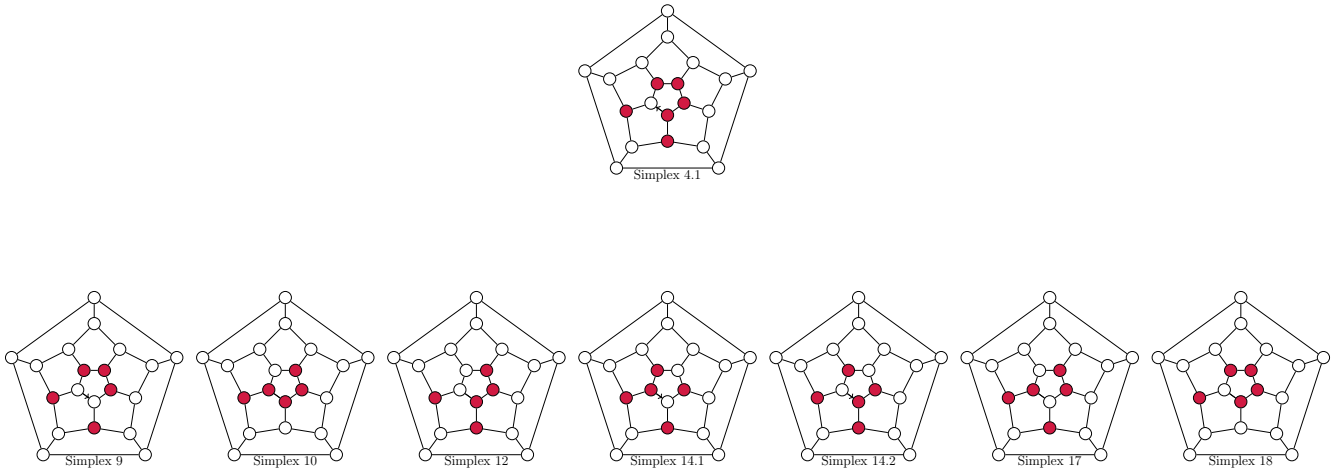

Figure B.4: Simplex 4.1 and its facets.

Simplex 4.2

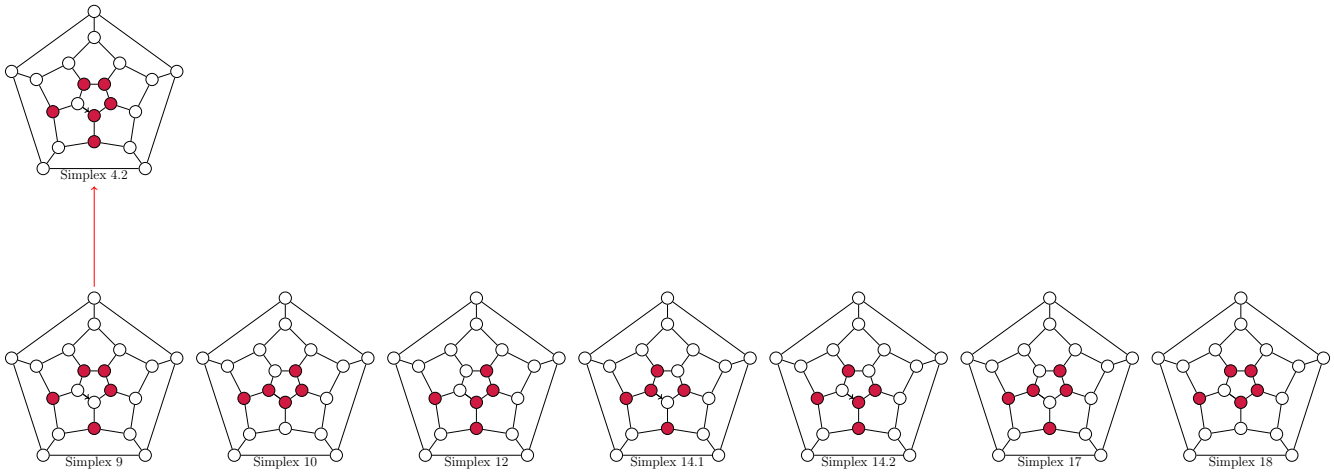

Figure B.5: Simplex 4.2 and its facets. Simplex 4.2 is matched with Simplex 9.

Simplex 5

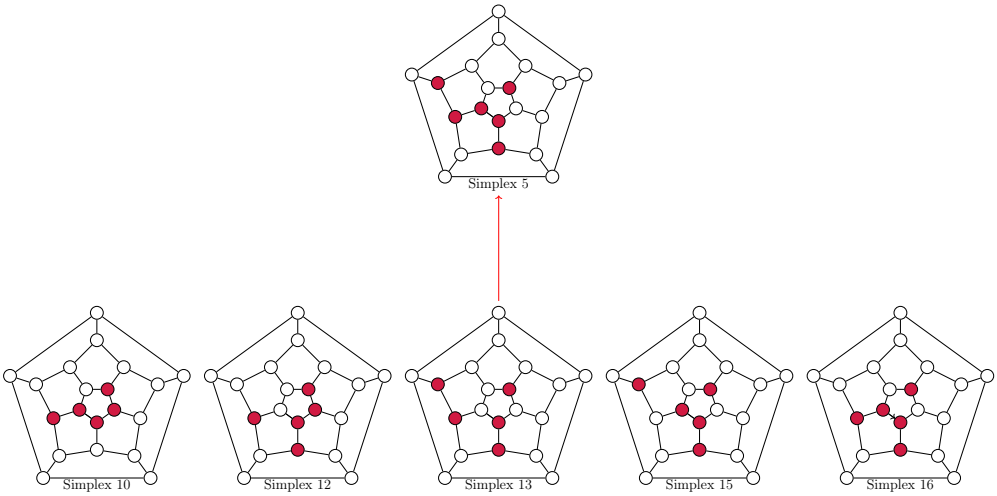

Figure B.6: Simplex 5 and its facets. Simplex 5 is matched with Simplex 13.

Simplex 6

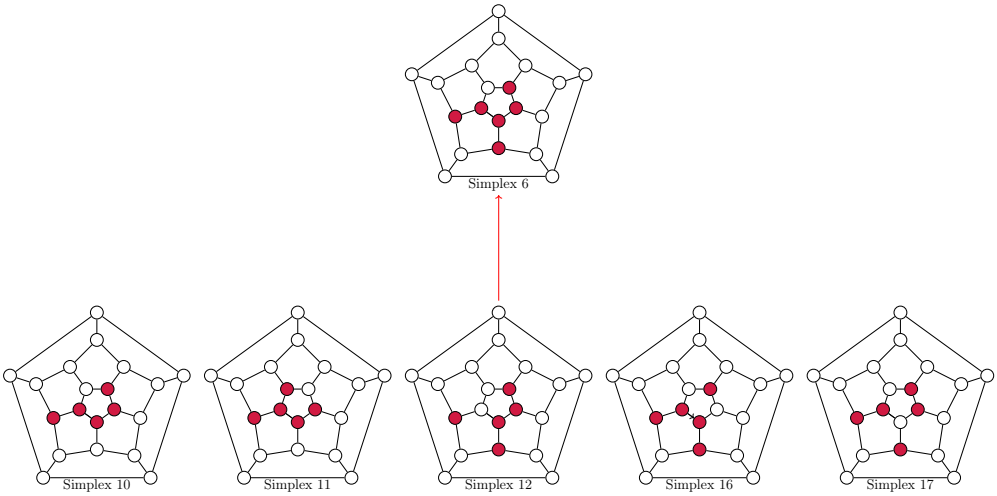

Figure B.7: Simplex 6 and its facets. Simplex 6 is matched with Simplex 12.

Simplex 7

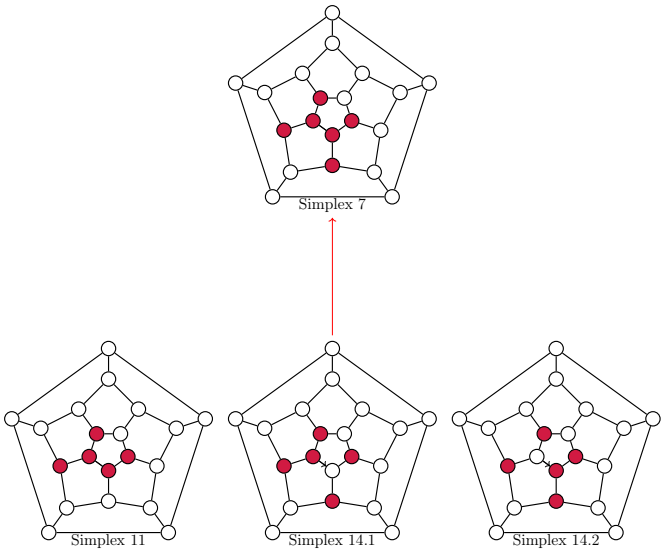

Figure B.8: Simplex 7 and its facets. Simplex 7 is matched with Simplex 14.1.

Simplex 8

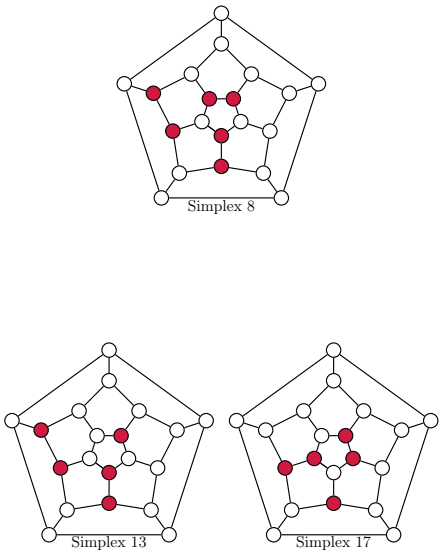

Figure B.9: Simplex 8 and its facets.

4-Simplices and their facets

Simplex 9

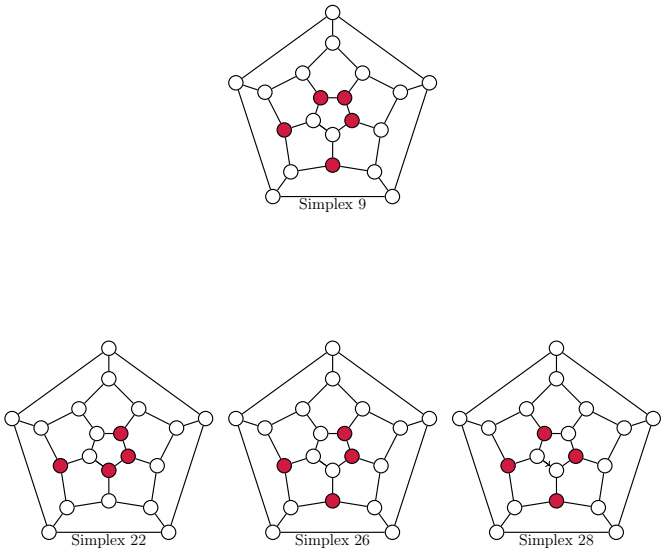

Figure B.10: Simplex 9 and its facets.

Simplex 10

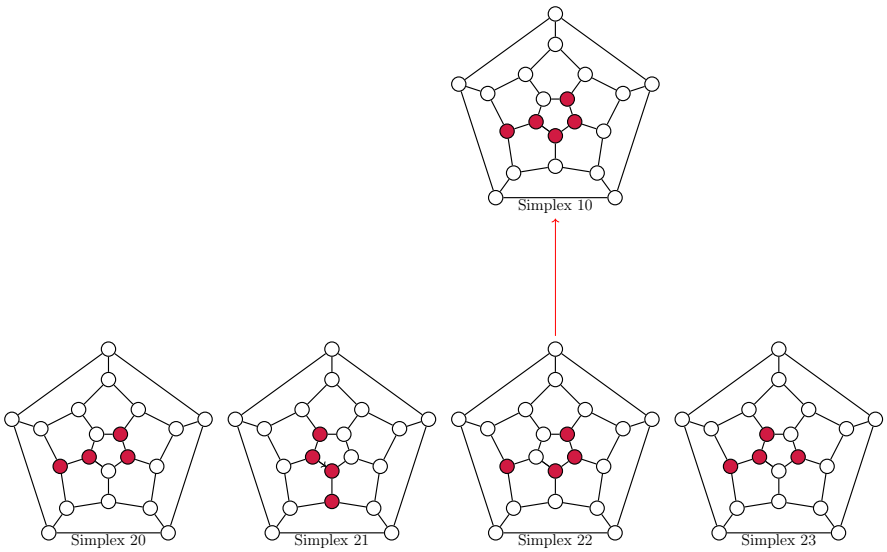

Figure B.11: Simplex 10 and its facets. Simplix 10 is matched with Simplex 22.

Simplex 11

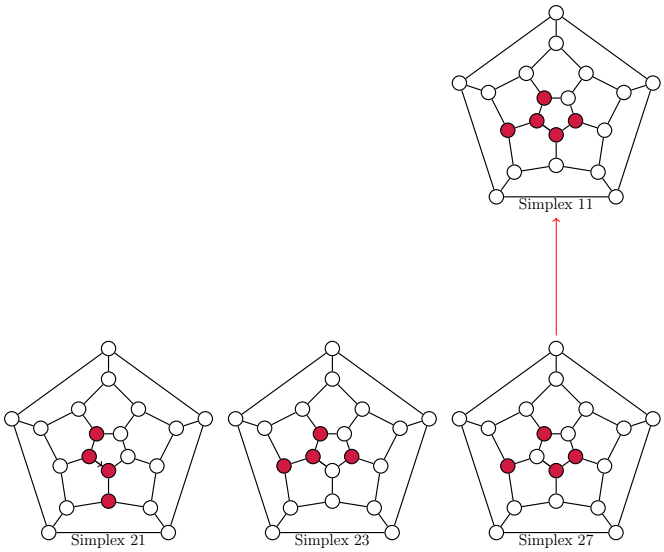

Figure B.12: Simplex 11 and its facets. Simplix 11 is matched with Simplex 27.

Simplex 12

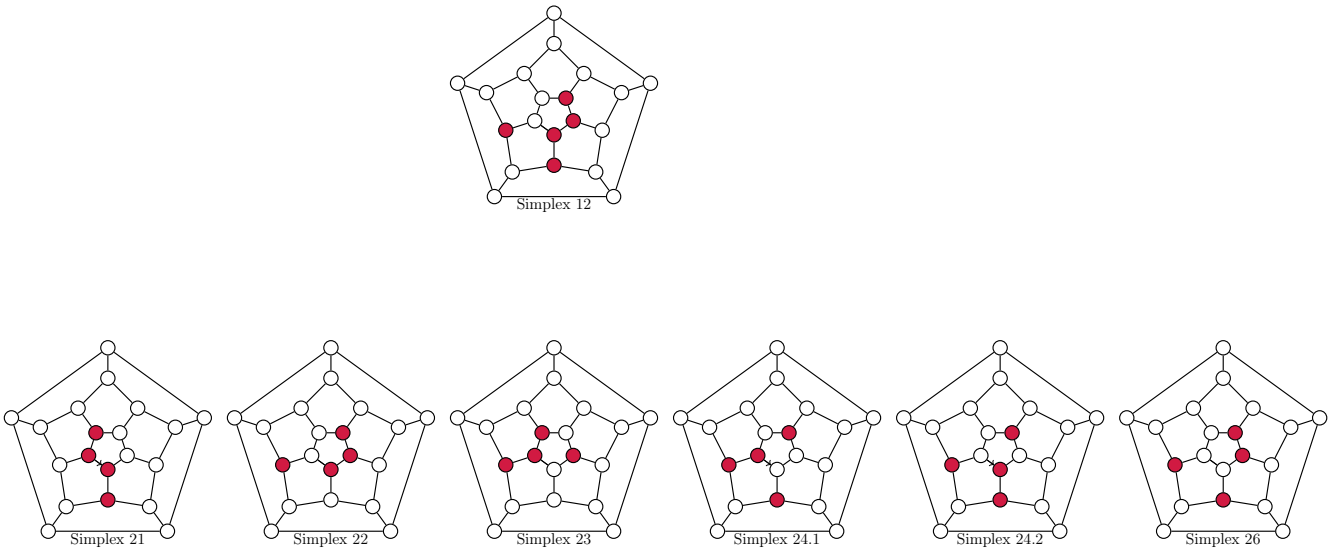

Figure B.13: Simplex 12 and its facets.

Simplex 13

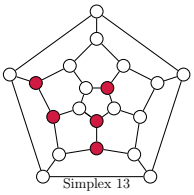

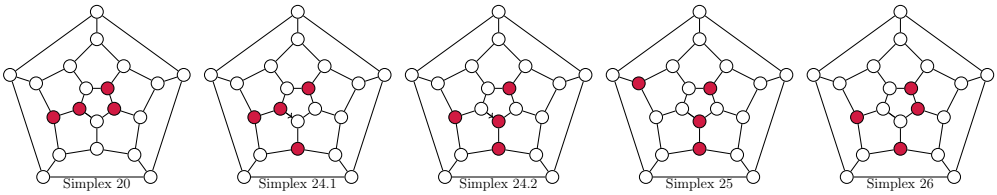

Figure B.14: Simplex 13 and its facets.

Simplex 14.1

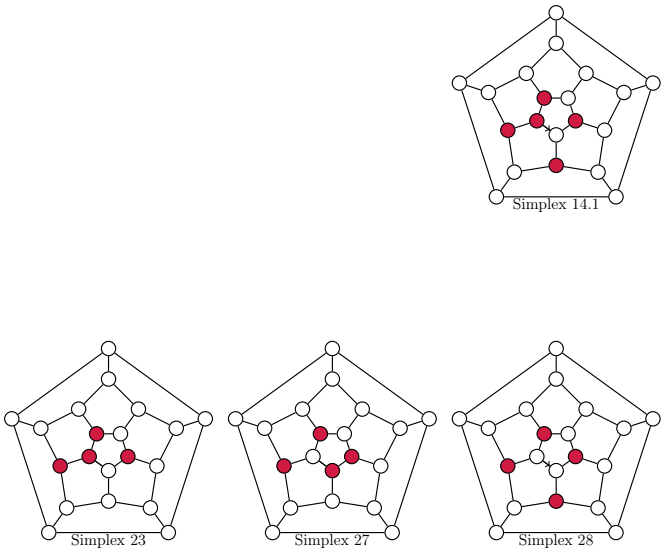

Figure B.15: Simplex 14.1 and its facets.

Simplex 14.2

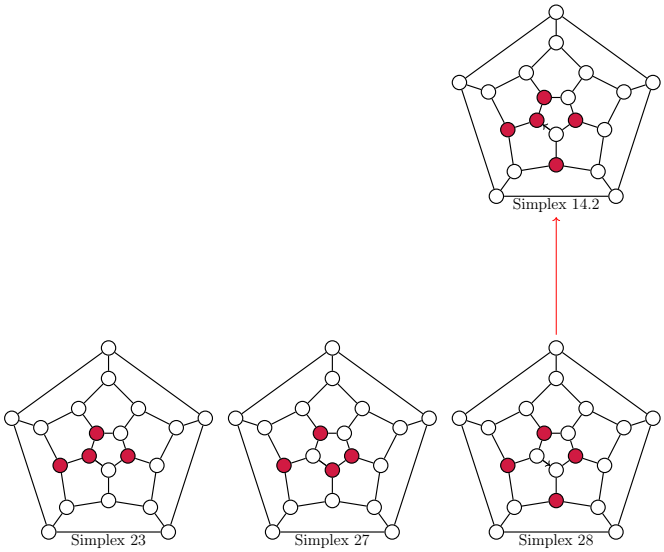

Figure B.16: Simplex 14.2 and its facets. Simplix 14.1 is matched with Simplex 28.

Simplex 15

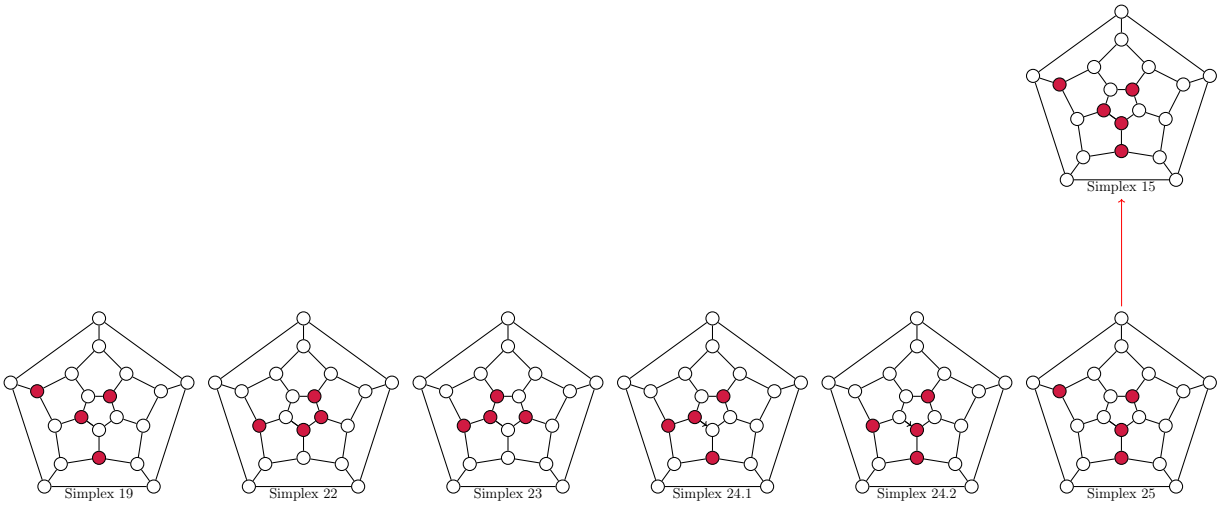

Figure B.17: Simplex 15 and its facets. Simplix 15 is matched with Simplex 25.

Simplex 16

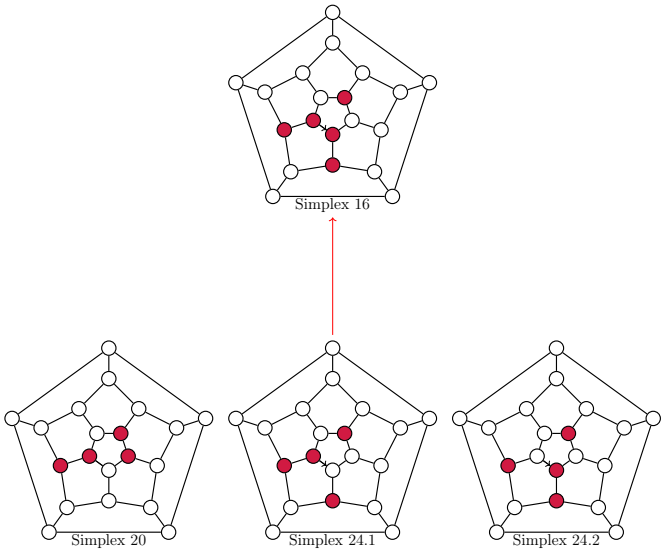

Figure B.18: Simplex 16 and its facets. Simplix 16 is matched with Simplex 24.1.

Simplex 17

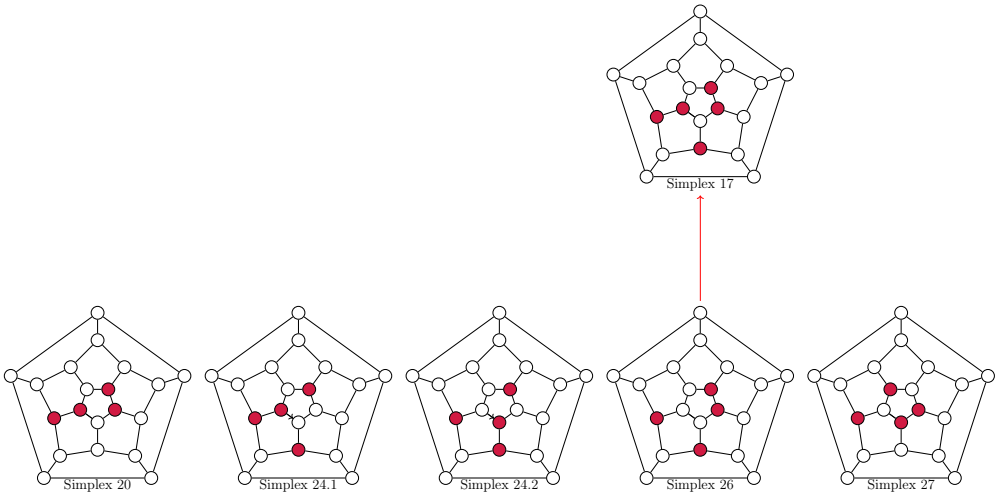

Figure B.19: Simplex 17 and its facets. Simplix 17 is matched with Simplex 26.

Simplex 18

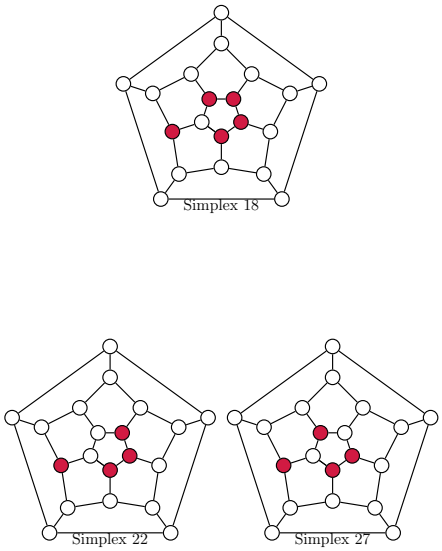

Figure B.20: Simplex 18 and its facets.

3-Simplices and their facets

Simplex 19

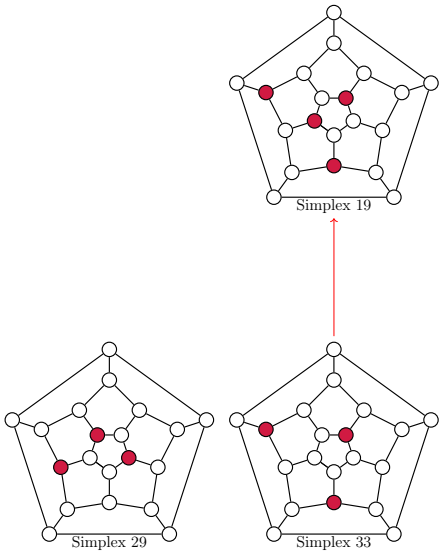

Figure B.21: Simplex 19 and its facets. Simplix 19 is matched with Simplex 33.

Simplex 20

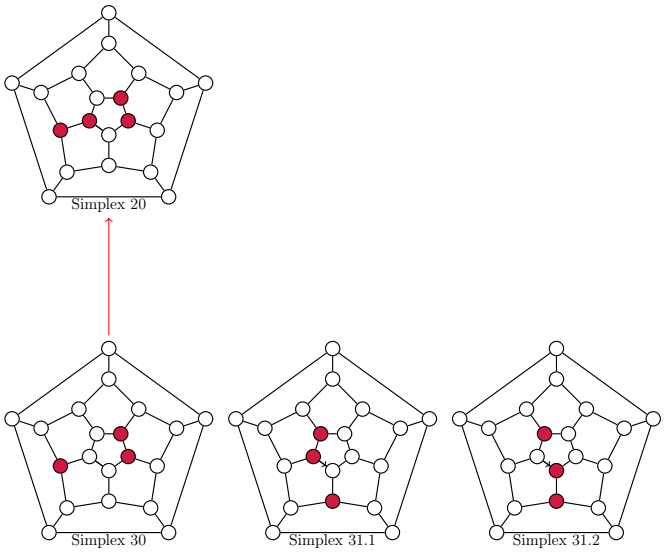

Figure B.22: Simplex 20 and its facets. Simplix 20 is matched with Simplex 30.

Simplex 21

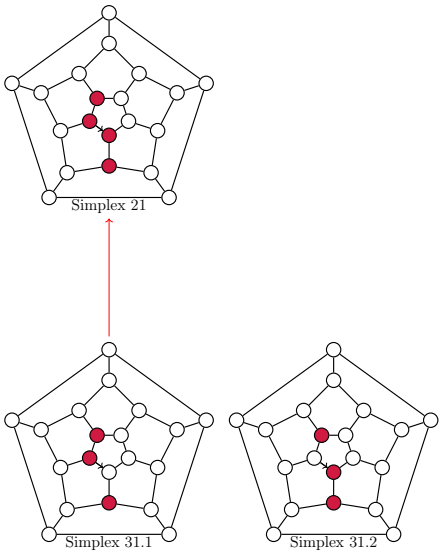

Figure B.23: Simplex 21 and its facets. Simplix 21 is matched with Simplex 31.1

Simplex 22

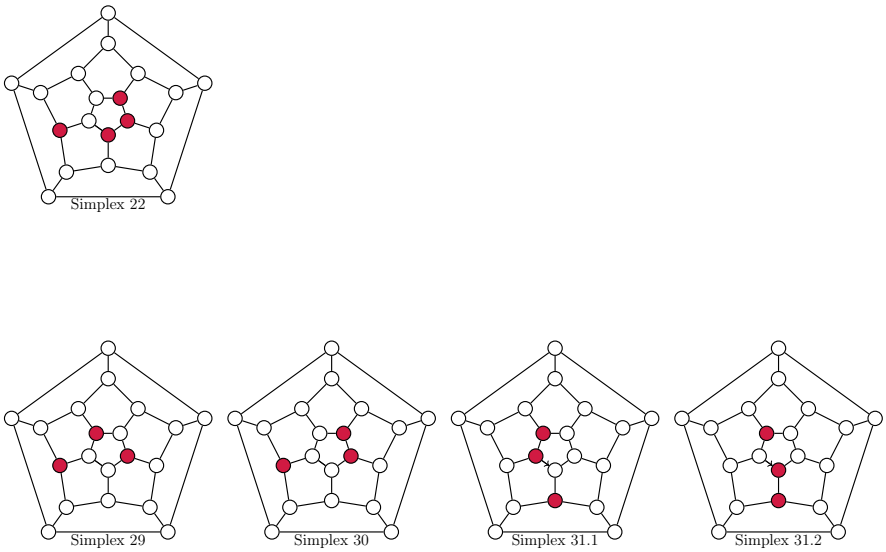

Figure B.24: Simplex 22 and its facets.

Simplex 23

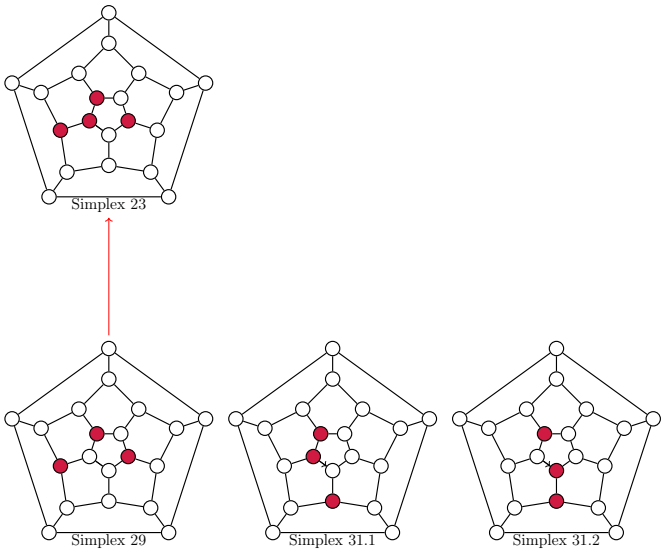

Figure B.25: Simplex 23 and its facets. Simplix 23 is matched with Simplex 29.

Simplex 24.1

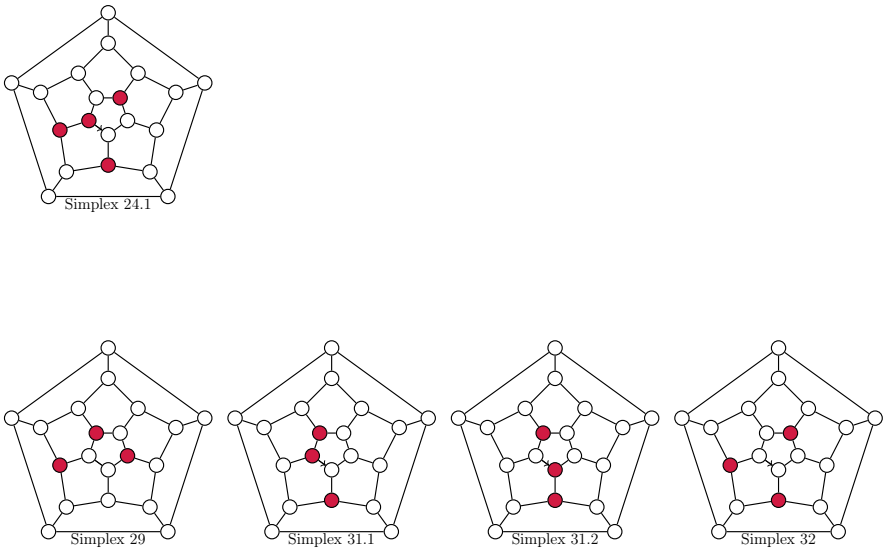

Figure B.26: Simplex 24.1 and its facets.

Simplex 24.2

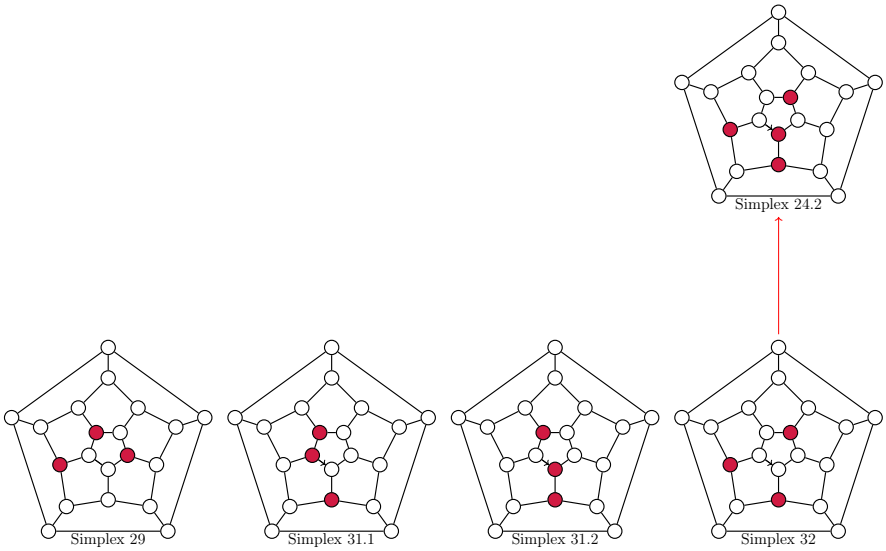

Figure B.27: Simplex 24.1 and its facets. Simplix 24.2 is matched with Simplex 32.

Simplex 25

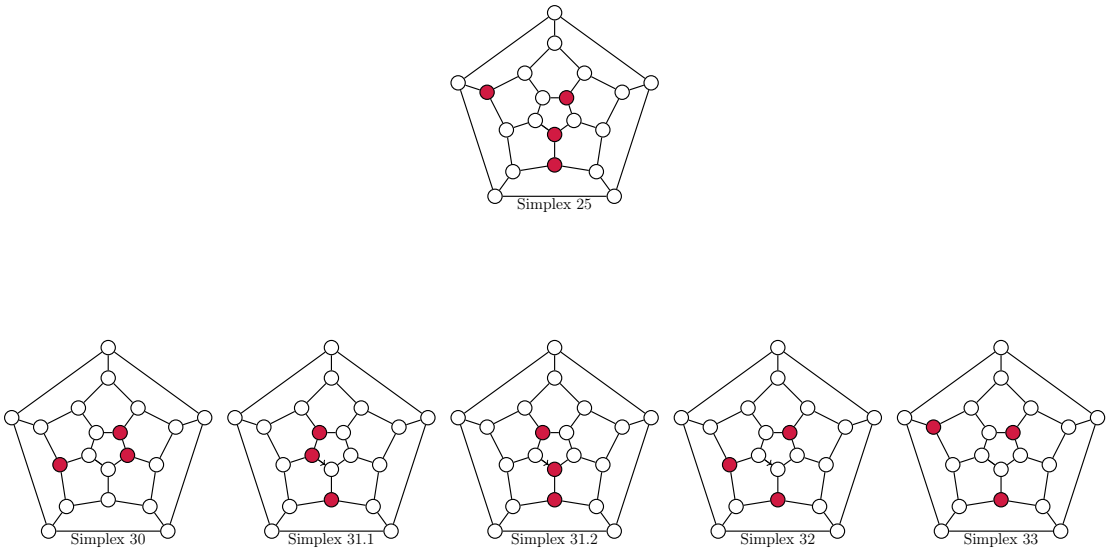

Figure B.28: Simplex 25 and its facets.

Simplex 26

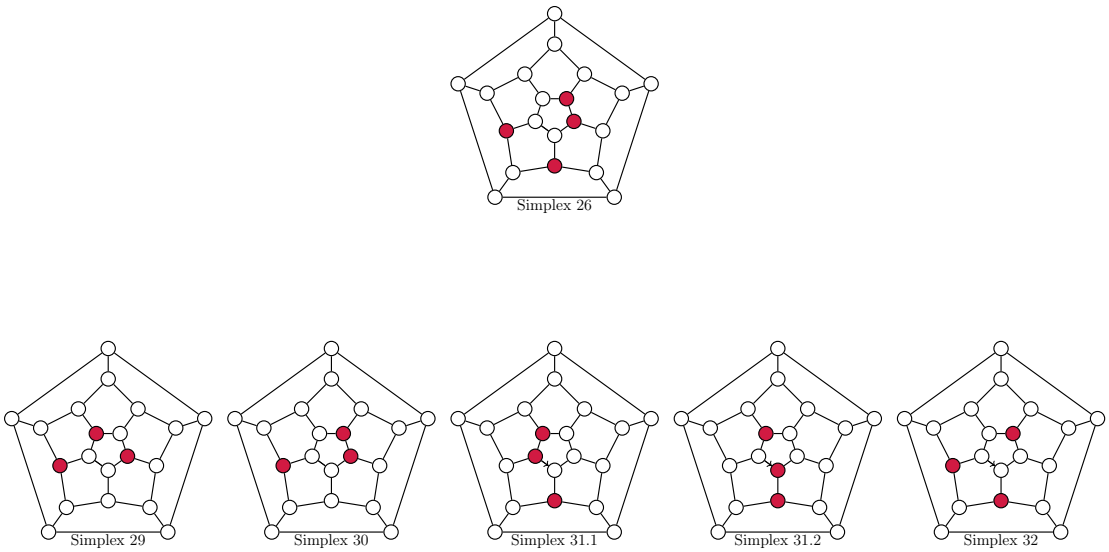

Figure B.29: Simplex 26 and its facets.

Simplex 27

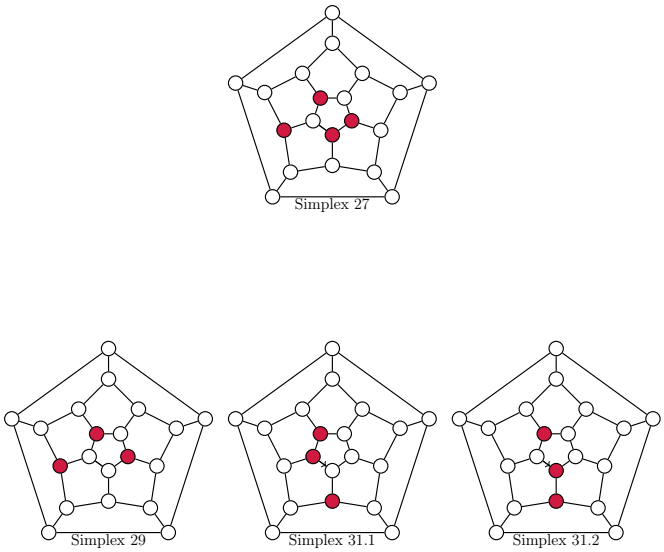

Figure B.30: Simplex 27 and its facets.

Simplex 28

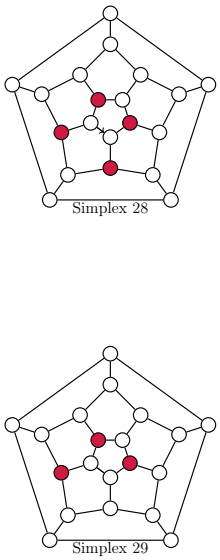

Figure B.31: Simplex 28 and its facet.

2-Simplices and their facets

Simplex 29

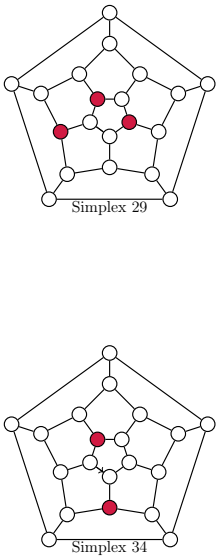

Figure B.32: Simplex 29 and its facet.

Simplex 30

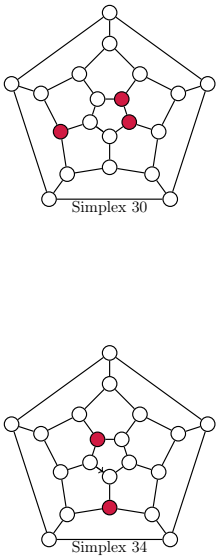

Figure B.33: Simplex 30 and its facet.

Simplex 31.1

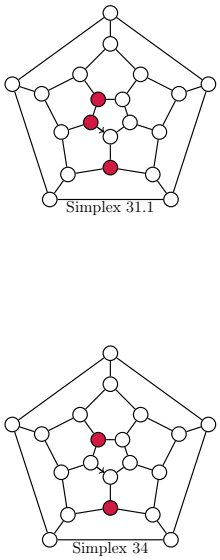

Figure B.34: Simplex 31.1 and its facet.

Simplex 31.2

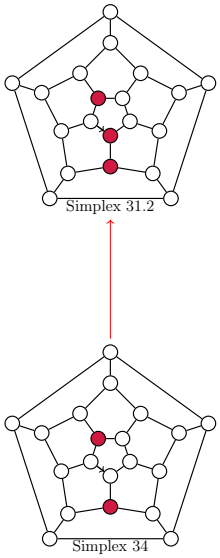

Figure B.35: Simplex 31.2 and its facet. Simplex 31.1 is matched with Simplex 34

Simplex 32

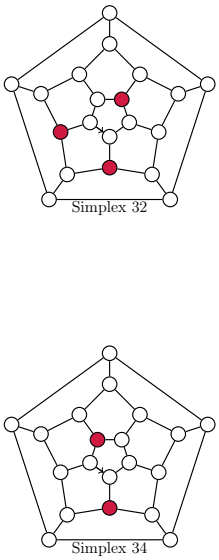

Figure B.36: Simplex 32 and its facet.

Simplex 33

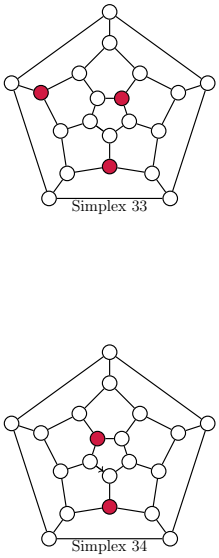

Figure B.37: Simplex 33 and its facet.

An illustration of the complete Hasse diagram of the simplices, where each number in a node refers to the simplex that has the same number.

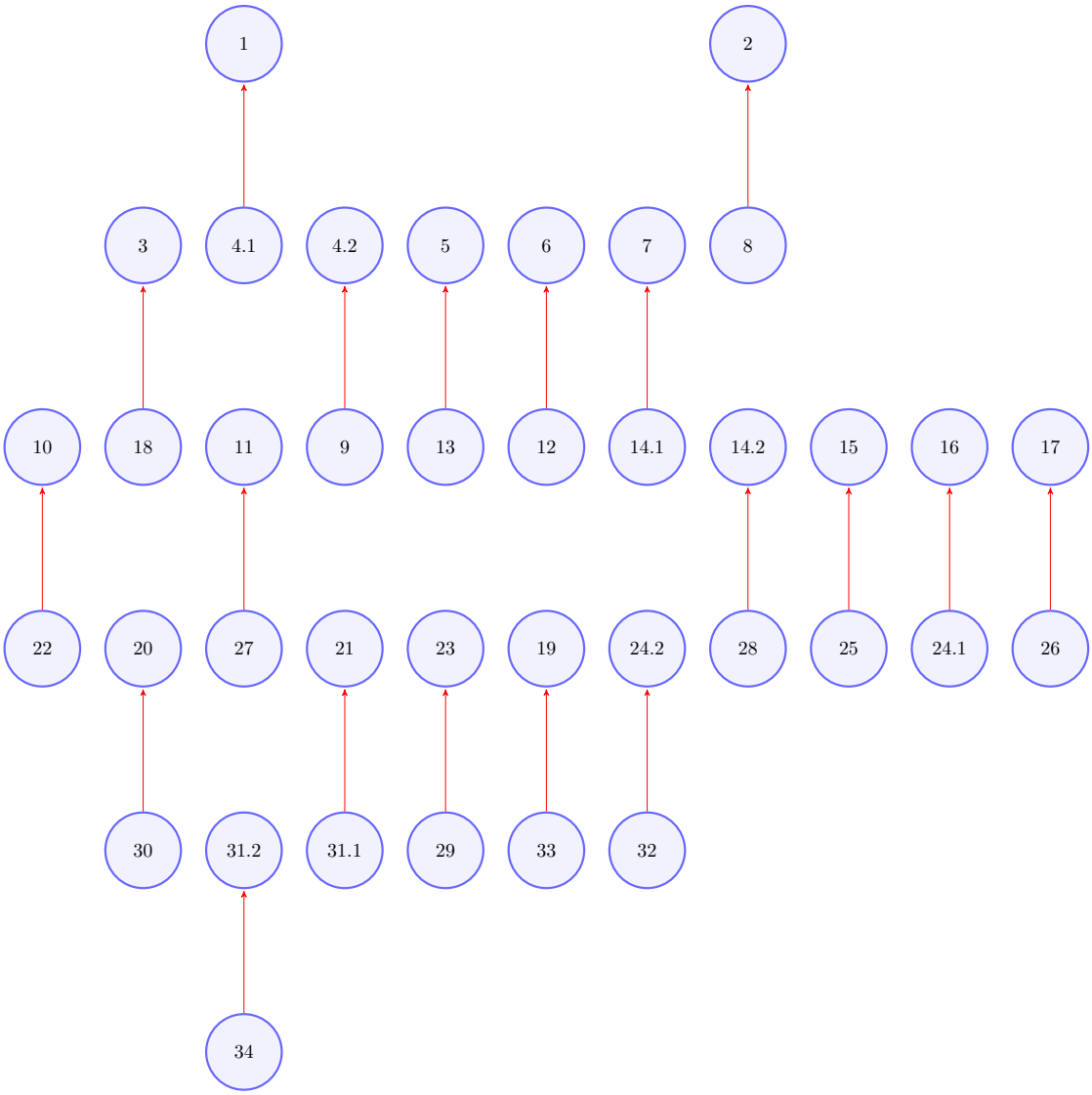

Figure B.38: The Hasse Diagram of the numbered simplices of the dodecahedron with the matching.

Selbstständigkeitserklärung

Ich erkläre: Ich habe die vorgelegte Dissertation selbstständig und ohne unerlaubte fremde Hilfe und nur mit den Hilfen angefertigt, die ich in der Dissertation angegeben habe. Alle Textstellen, die wörtlich oder sinngemäß aus veröffentlichten Schriften entnommen sind, und alle Angaben, die auf mündlichen Auskünften beruhen, sind als solche kenntlich gemacht. Ich stimme einer evtl. Überprüfung meiner Dissertation durch eine Antiplagiat-Software zu. Bei den von mir durchgeführten und in der Dissertation erwähnten Untersuchungen habe ich die Grundsätze guter wissenschaftlicher Praxis, wie sie in der "Satzung der Justus-Liebig-Universität Gießen zur Sicherung guter wissenschaftlicher Praxis" niedergelegt sind, eingehalten.

Gießen, Juni.2023

Nada Saleh